Electrochemical Chlorine Evolution at Sol-Gel Derived Mixed Oxide Electrocatalyst Coatings

Dissertation

Zur Erlangung des Grades des Doktors der Naturwissenschaften

der Naturwissenschaftlich-Technischen Fakultät III

der Universität des Saarlandes

von

Ruiyong Chen

Saarbrücken

2010

Tag des Kolloquiums:	04. February 2011
Dekan:	Prof. Dr.-Ing. Stefan Diebels
Berichterstatter:	Prof. Dr. Rolf Hempelmann
	Prof. Dr. Wilhelm F. Maier
	Prof. Dr. Herbert Over
Prüfungsvorsitzender:	Prof. Dr. Kaspar Hegetschweiler
Akademischer Beirat:	Dr. Harald Natter

Abstract

Performance improvement in electrode coatings plays a critical role in reducing energy consumption (i.e., overpotential) in the electrolytic chlorine production. The performance dependence on the chemical composition, surface morphology and phase structure of the oxide coatings has been investigated systematically. The multi-component $RuTiMO_x$ system prepared by the sol-gel route improved effectively the catalytic performance with M = Ir, Sn, V. The impermeable crack-free coatings obtained by controlling the coating/drying process are expected to protect the Ti-substrate against passivation. Nano-pores created by lanthanum leaching from the La-containing oxide matrix provided highly accessible surface. A novel in-situ supported rutile $RuTiO_2$/anatase TiO_2 structure with enhanced catalytic activity was achieved by the solvothermal crystallization of the Ru-O-Ti xerogel. Cl_2 bubble evolution behaviour at the $RuTiMO_x$/Ti electrodes has been studied in a first approach by analyzing the bubble-induced potential noise using wavelet transform.

Zusammenfassung

Die Effizienzverbesserung der Elektrodenbeschichtungen spielt eine kritische Rolle bei der Reduzierung des Energieverbrauchs (z.B. der Überspannung) für die elektrolytische Chlorentwicklung. Die Effizienzabhängigkeit der Oxidbeschichtung wurde systematisch in Abhängigkeit von der chemischen Zusammensetzung, der Oberflächenbeschaffenheit und der Phasenstruktur untersucht. Die Multikomponent-Beschichtung $RuTiMO_x$ wurde im Sol-Gel Verfahren hergestellt, wobei der Anteil von M=Ir, Sn, V die katalytische Effizienz erheblich verbesserte. Die undurchlässigen und rissfreien Beschichtungen, die durch ein kontrolliertes Beschichten/Trocknen-Verfahren erhalten wurden, sollen die Passivierung des Ti-Substrats verhindern. Es wurden Nano-Poren infolge eines Leaching-Verfahrens aus einer Lantan-haltigen Oxidmatrix erhalten, die eine höchst zugängliche Oberfläche bieten. Mittels einer solvothermalen Kristallisierung des Ru-O-Ti-Xerogels wurde eine neue, in-situ-verstärkte Rutil-$Ru_xTi_{1-x}O_2$/Anatas-TiO_2 Struktur erhalten, die eine erhöhte katalytische Aktivität aufweist. Die Entwicklung der Cl_2-Gasblasen auf $RuTiMO_x$/Ti-Elektroden wurde in einem ersten Ansatz durch die Analyse des blaseninduzierten Potentialrauschens mit Hilfe der Wavelet-Transformation untersucht.

Table of Contents

1 Introduction

The industrial sector accounts for about a third of the both global primary energy consumption and energy-related CO_2 emissions. Industrial energy efficiency has a significant impact on the mitigation of the climate change, security of energy supply, and sustainability. Energy-efficient technological innovations, particularly in the energy-intensive industrial manufacturing processes, become the core factors considered as sustainable industrial strategy in the future.

Chlorine and its co-product caustic soda (sodium hydroxide) are important building blocks for the whole chemical and pharmaceutical industry, which are produced industrially by the electrolysis of brine. Electricity is essential to produce chlorine in the chlor-alkali industry, which accounts for about half of the total production cost. Energy savings arise primarily through using more efficient technologies, such as the replacement of the less energy-efficient mercury and diaphragm processes by the most energy-efficient membrane technology, and the substitution of the hydrogen evolving cathode by the oxygen depolarized cathode.

In terms of electrocatalysis, the chemical reaction proceeds electrochemically, i.e. it is driven by the electrode potential. Overpotential related to the electron transfer reactions at the electrode could be reduced by proper selection of electrode materials. Thus it is a task for chemists to develop and evaluate new catalytic materials and accordingly new preparation routes to meet the continuous expansion of industrial requirements. This is one of the motivations of the present research project to optimize the electrocatalysts and to innovate in the preparation strategy of electrocatalysts.

Furthermore, the design in electrode coating morphology (surface and cross-section) was studied regarding the issue of electrode deactivation caused by the substrate passivation. A protective and impermeable crack-free oxide layer deposited onto the titanium substrate has been fabricated by controlling the dipping/drying/sintering processes. Nanoporous

electrode coatings were obtained by the lanthanum leaching route in order to increase the electrocatalytically accessible active surface area, which could improve the electrocatalytic performance as a geometrical factor.

The crystallization process of the mixed oxide coatings was modified by using solvothermal curing of the xerogel coatings followed by post-sintering treatment. The resulting phase structure and the electrochemical properties of the electrode coatings as a function of the solvothermal processing parameters have been investigated. Detailed structural characterization of the solvothermally prepared electrode coatings has been carried out in order to elucidate the achieved significant improvement in the electrocatalytic activity for chlorine evolution.

Chlorine gas bubbles generated at the electrode surface result in additional ohmic drop due to the shielding and blocking effects. The preliminary identification of the bubble evolution behaviour at the electrode surface was performed by analyzing the bubble-induced electrochemical noise. Various mathematical analysis methods such as the statistical standard deviation, autocorrelation function and Fourier power spectral density were performed to analyze the time series of potential noise. Wavelet transform, which is used widely in the field of signal processing as an alternative to the conventional Fourier transform, was used to extract the characteristic bubble evolution information, such as detachment frequency, and also the possible in-situ wettability analysis of electrode coatings. The proposed analytical strategy is able to be extended to the further evaluation of the electrode material, morphology and structure dependent gas evolution behaviour.

2 Theory and background

2.1 The history of industrial chlorine production

Chlorine is essential to the global chemical industry and to our daily life. Approximately 50% of the products marketed by the chemical industry and 85% of the pharmaceuticals are derivatives of chlorine chemistry [1]. The production of chlorine is being esteemed as ‘‘Engine’’ of the chemical industry in a country. The industrial chlorine production dates back to the last half of the 19th century [2]. At that time chlorine was produced from hydrochloric acid by the so-called Weldon and Deacon processes (chemical oxidation route). The Weldon process uses the manganese dioxide (MnO_2) as reactant:

$$MnO_2 + 4HCl \xrightarrow{100-110^{\circ}C} MnCl_2 + Cl_2 + 2H_2O \tag{2.1}$$

The manganese is recycled by treating the $MnCl_2$ with lime (CaO, which is mixed with H_2O to obtain calcium hydroxide) and oxygen to improve the process economics:

$$2MnCl_2 + 3Ca(OH)_2 + O_2 \longrightarrow 2MnO_2 + CaO + 2CaCl_2 + 3H_2O \tag{2.2}$$

The Deacon process generates chlorine by direct catalytic oxidation of the hydrochloric acid gas with air according to:

$$4HCl + O_2(air) \xrightarrow[Catalyst]{ca.300^{\circ}C} 2Cl_2 + 2H_2O \tag{2.3}$$

The reaction (2.1) and (2.3) are the secondary process of the manufacture of sodium carbonate (Na_2CO_3) by the Leblanc process:

$$\begin{array}{ccccc} NaCl & \xrightarrow{H_2SO_4} & Na_2SO_4 & \xrightarrow{C} & Na_2S & \xrightarrow{CaCO_3} & Na_2CO_3 \\ & & + HCl & & + CO_2 & & + CaS \end{array}. \tag{2.4}$$

In the late 19th century, the Solvay process for carbonates began to replace the Leblanc process and the shortage of HCl made it necessary to find new route to produce chlorine. Most chlorine today is produced by using the electrolytic processes (electrolytic oxidation

route), where solutions of sodium chloride are electrolyzed to convert chloride ions (Cl^-) into molecular chlorine (Cl_2) at the anode. Simultaneously, sodium hydroxide (NaOH) solution and hydrogen (H_2) are produced at the cathode side, according to the following equations.

$$\text{Anode: } 2Cl^- \rightarrow Cl_2 + 2e^- \tag{2.5}$$

$$\text{Cathode: } 2H_2O + 2e^- \rightarrow H_2 + 2OH^- \tag{2.6}$$

$$\text{Overall: } 2NaCl + 2H_2O \rightarrow 2NaOH + Cl_2 + H_2 \tag{2.7}$$

Only a tiny part of chlorine is produced worldwide by other processes, such as the chlorine recovery by the electrolysis of hydrochloric acid (HCl) solutions. Hydrogen chloride gas is a by-product in the processes used to manufacture polyurethanes, fluorocarbons, hydro-fluorocarbons and white pigments, in which chlorine used is reduced to hydrogen chloride. The Deacon catalytical oxidation process [3], which is a thermochemical process opposite to the electrochemical process, is beyond the scope of the present work.

Among the amalgam process, diaphragm process and membrane process, in which different anode products separations are involved, the mercury process is the most energy intensive process, whereas the membrane process is the most energy-efficient process (ca. 2500 kWh of electrical energy consumption is required to produce one ton of chlorine). All new plants in the world are based on the membrane cell process nowadays. Worldwide, the annual production of chlorine amounts to approximately 55 million metric tons in the year 2005 [4]. Accordingly, the overall energy consumption amounts to more than 1.5×10^{11} kWh/a [5]. Therefore, a significant reduction of the energy consumption in the chlor-alkali industry is highly desirable.

The total consumption of electric power is proportional to the voltage applied to the cell for a given current density (the rate of electrode reaction) (See: *Appendix* A4). The cell voltage consists of several components [6]:

$$\triangle V = \triangle E + \triangle \eta + IR_e + \triangle V_{ad} \tag{2.8}$$

where $\triangle E$ is the thermodynamic potential difference for a given anode/cathode reaction, $\triangle \eta$ is the sum of the overpotentials for the anodic and cathodic reactions (which are dependent on the electrocatalysts), IR_e is the ohmic drop of the electrolyte, and $\triangle V_{ad}$ is the additional ohmic drop from the membrane, gas bubble effect etc. Industrial demands for the energy-efficient chlorine production in order to reduce the electrical power consumption in the chlor-alkali electrolysis processes drive increasingly the scientific and technical innovations, since the electrical power consumption occupies almost 50% of the cost of chlorine manufacturing.

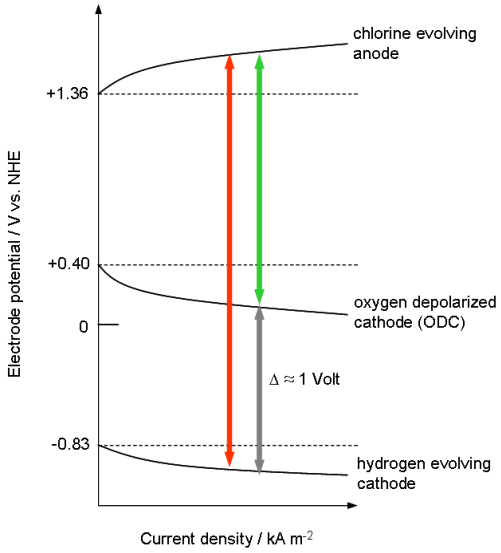

Figure 2.1. Electrode potential in chlor-alkali electrolysis from NaCl aqueous solution as a function of current density. The curves deviate away from the dotted lines (The equilibrium potentials, which vary with the operation parameters, such as temperature and concentration. For simplicity, standard equilibrium potentials were given in this figure.) with the increase of current density indicating the overpotential required to drive the electrochemical reactions. The unit of the current density mA cm^{-2} was used throughout the present work to present the obtained experimental data, whereas the kA m^{-2} is more often used in the industrial technical data. 100 mA cm^{-2} = 1 kA m^{-2}.

The electric energy needed for driving the electrode reaction depends on the reaction type of the electrolytic cell. The hydrogen evolving cathode (HEC) (see Eq. (2.6)) can be replaced by the oxygen depolarized cathode (ODC):

$$O_2 + 2H_2O + 4e^- \rightarrow 4OH^- \quad (2.9)$$

Accordingly, the overall reaction turns to:

$$4NaCl + 2H_2O + O_2 \rightarrow 4NaOH + 2Cl_2 . \quad (2.10)$$

A comparison of the HEC and ODC process is illustrated in Figure 2.1. The thermodynamic potential difference for the classical electrolysis with HEC is about 2.2 V (in practice, the overall cell voltage is approximately 3.1 V including the anode and cathode overpotential, ohmic resistance in membrane, electrolyte and electrode materials, electrode gap). The ODC cell reduces the overall cell voltage by around 1 V compared to the conventional process [7].

A technological breakthrough in the history of electrolytic chlorine production is the presence of Dimensional Stable Anodes (DSA®), which were invented by H.B. Beer in 1965 [8 , 9], and were then developed and industrialized by De Nora [10]. The commercially available DSA consists of RuO_2 as active component, inert oxide such as TiO_2 as stabilizer and coated onto titanium substrate [11]. The DSA using a conductive titanium substrate as a substitution for conventional graphite anodes benefits from the fact that fixed inter-electrode gap can be remained during the long-term operation of electrolytic cell. RuO_2 exhibits excellent corrosion resistance and low potential for anodic chlorine evolution reaction, which can be diluted and stabilized by TiO_2 by obtaining a rutile structure of mixed oxide solid solution. A thermal decomposition method is generally used to prepare this kind of electrode coatings.

2.2 The anodic process

2.2.1 Anodic chlorine evolving reaction and classical equations

The electrolysis process consists of the electron transfer at the electrode surface; ions pass through the electrolyte between the anode and cathode; and electrons transfer through the wires externally interconnecting the two electrodes. The current through the external circuit is a convenient measure of the rate of the cell reaction. The charge (Q) required to convert the starting materials to products in an electrode reaction is calculated using Faraday's law: $Q = nFm/M$, where m is the mass of the substance produced from the electrochemical reaction, M is the molar mass of the substance, F is the Faraday constant and n is the number of equivalents per molar of reactant.

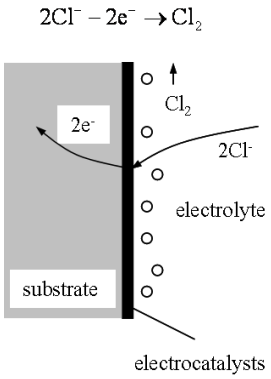

Figure 2.2. Pictorial drawing of chlorine evolution reactions at the anode side, which involves a series of steps: The reactant Cl^- moves to the interface (mass transport); electron transfer occurs close to the interface (electron transfer reaction); the product Cl_2 moves away from the anode to allow the fresh reactants to the anode surface.

In the anode reaction, the oxidation of Cl^- species occurs by the loss of electrons to the anode, as shown in Figure 2.2. The electrode reaction is a sequence of several basic steps. To maintain a current it is essential to supply reactants to the electrode surface and also remove the products (i.e. the mass-transfer processes, such as diffusion and convection of

the reacting species between the electrode surface and bulk of the solution), as well as for the electron transfer reactions at the electrode surface.

For a simple reversible electrode reaction (electrochemical oxidation process):

$$R \underset{k_b}{\overset{k_f}{\rightleftharpoons}} O + ne^- \tag{2.11}$$

If the current i_f and i_b are assigned to the forward and backward reactions, respectively, the electrochemical reaction rate can be expressed usually by the net Faradaic current:

$$i = i_f + i_b \tag{2.12}$$

where $i_f > 0$ and $i_b < 0$. At equilibrium conditions, which means that the forward and reverse reactions proceed at the same rates, the positive current contributed by the forward reaction is balanced by the negative current contributed by the backward current, $i_f = -i_b = i_0$, (where $j_0 = i_0/A$ is the exchange current density, A is the electrode surface area) and the net Faradaic current is equal to zero, $i = 0$.

The process of reduction of O and oxidation of R is a dynamic equilibrium at the surface of the working electrode. The equilibrium potential (E_e) of the working electrode is given by the Nernst equation:

$$E_e = E_e^{\,0} + \frac{RT}{nF} \ln \frac{C_O^s}{C_R^s} \tag{2.13}$$

where $E_e^{\,0}$ is the standard equilibrium potential of the couple R/O, $C_R^{\,s}$ and $C_O^{\,s}$ are the surface concentration of R and O species at the working electrode, respectively. R, T and F are universal gas constant 8.314 J mol^{-1} K^{-1}, absolute temperature in degrees Kelvin and Faraday's constant (the number of coulombs per mole of electrons, F = 96485 C mol^{-1}), respectively, and n is the number of electrons transferred in the anode reaction. For the chlorine evolution (Eq. (2.5)), the equilibrium potential is represented by:

$$E_e = E^0_{cl^-/Cl_2} + \frac{RT}{2F}\ln\frac{p_{Cl_2}}{\left(\alpha_{Cl^-}\right)^2}, \tag{2.14}$$

where $E^0_{cl^-/Cl_2}$ is the standard potential (1.36 V vs. NHE), p_{Cl_2} is the partial pressure of chlorine in the gas phase, and α_{Cl^-} is the activity of the chloride ion.

If the potential of the working electrode is imposed more positive than the equilibrium potential ($E > E_e$), this will require current to flow through the electrode/solution interface. In fact, the decrease in the ratio C_R^s / C_O^s is necessary, and this can be brought about by the conversion of *R* to *O* by the passage of an anodic current to the counter electrode. The overpotential is defined as the deviation of the potential from the equilibrium value, i.e.

$$\eta = E - E_e. \tag{2.15}$$

Overpotential is the driving force for the electrode reaction to proceed in a given direction. Overpotential arises from the kinetic limitations of the electrode reaction for a given electrode material.

For a given electron transfer reaction (Eq. (2.11)) without the mass-transfer limitation, the empirical relation between the current density and overpotential is given commonly by the Butler-Volmer equation:

$$j = j_0\left\{\exp\left(\frac{(1-\alpha)nF}{RT}\eta\right) - \exp\left(-\frac{\alpha nF}{RT}\eta\right)\right\} \tag{2.16}$$

where *j* is current density, j_0 is the exchange current density, η is the overpotential, and α is the dimensionless electronic transfer coefficient with a value between 0 and 1. *R*, *T* and *F* have its usual meanings and *n* is the number of electrons involved in the electrode reaction. It is worth noting that the Bulter-Volmer equation is valid when the electrode reaction is controlled by electrical charge transfer at the electrode and not by the mass transfer.

The Butler-Volmer equation is valid over the full potential range. At high positive overpotential $|i_f| >> |i_b|$, the second term in Eq. (2.16) may be ignored, i.e., the reverse

rate is negligible compared to the forward reaction rate. Hence, a simple exponential relationship between the anodic current density and overpotential is then given by:

$$\log j = \log j_0 + \frac{(1-\alpha)nF}{2.303RT}\eta, \tag{2.17}$$

which is known as the Tafel equation, $\eta = a + b\log j$. It describes the relation between the rate (i.e., current) of an electrode reaction and the overpotential. The slope of a Tafel plot ($b = \frac{2.303RT}{1-\alpha\ nF}$) reveals the value of the electronic transfer coefficient (α) for the anode reaction, which can be measured experimentally.

At low overpotential region of the Butler-Volmer equation, the exponential terms in Eq. (2.16) may be linearized in a Taylor series expansion, and thus a linear dependence of *j*-η is usually obtained, i.e. $j = j_0 \frac{nF}{RT}\eta$. From the slope of the linear dependence of *j*-η, the exchange current density, j_0, can be determined, i.e.,

$$\lim_{\eta\to 0}\frac{dj}{d\eta} = \frac{nF}{RT}\, j_0 . \tag{2.18}$$

The charge transfer resistance, R_{ct} (ohm cm^2), is defined as the slope of the overpotential versus current density at the equilibrium potential (i.e. at zero net current, when the overpotential is very small and the electrochemical system is at equilibrium):

$$R_{ct} = \frac{d\eta}{dj} = \frac{1}{dj/d\eta} = \frac{RT}{nFj_0}\cdot\frac{1}{(1-\alpha)\cdot\exp\left((1-\alpha)\frac{nF}{RT}\eta\right)+\alpha\cdot\exp\left(-\alpha\frac{nF}{RT}\eta\right)} \tag{2.19}$$

which describes the dynamic behaviour of the redox reaction. Note that the value of R_{ct} changes with the overpotential and $R_{ct} = \frac{RT}{nFj_0}$ for η = 0.

2.2.2 The reaction mechanisms and kinetics of anodic chlorine evolution

The reaction paths for the chlorine evolution reactions (Eq. (2.5)) at the anode materials have been described by the following mechanism (i) or mechanism (ii) [12]:

(i): Volmer-Tafel mechanism [13]

$Cl^- \rightarrow Cl_{ads} + e^-$ (Volmer reaction, the primary electron transfer step, with the formation of adsorbed species (Cl_{ads}), by the discharge of its counter species at the anode surface)

$2Cl_{ads} \rightarrow Cl_2$ (Tafel reaction, with the formation of molecular product (Cl_2) by recombination of two neighbouring surface chlorine atoms)

(ii): Volmer-Heyrovsky mechanism [14]

$Cl^- \rightarrow Cl_{ads} + e^-$ (Volmer reaction)

$Cl^- + Cl_{ads} \rightarrow Cl_2 + e^-$ (Heyrovsky reaction, with the formation of molecular product (Cl_2) by the electrochemical desorption of adsorbed species (Cl_{ads}) and a simultaneous oxidation of Cl^-)

The initial Volmer step is the electron transfer, resulting in the formation of the adsorbed intermediate Cl_{ads}. The molecular Cl_2 is formed by either chemical desorption (Tafel step) or electrochemical desorption (Heyrovsky step) of the adsorbed species.

The value of the Tafel slope depends on the rate-determining step of the Faradaic reaction. The Tafel slope and exchange current density for a given electrode reaction at a given electrocatalyst are essential for understanding the reaction mechanism. It is desirable to have high exchange current density and low Tafel slope for the electrode reactions, which permits the operation at high current densities without significant voltage supply.

Different reaction mechanisms for the chlorine evolution at oxide electrodes have been proposed [15]. The obtained Tafel slope depends on the concentration of NaCl, the operation temperature, pH value. Various electrode materials have been investigated for the chlorine evolution reaction (Table 2.1), and the kinetic parameters dependence on the electrode material are summarized.

Table 2.1. Kinetic parameters for the chlorine evolution reactions from 5 M NaCl, at 25°C [16].

Electrode material	j_0 / mA cm^{-2}	Tafel slope / mV	Mechanism
Pt	8.5	72	ii
Ir	6.4	76	ii
Rh	5.9	90	ii
$Pt_{0.7}Ir_{0.3}$ (smooth)	0.85	86	ii
$Pt_{0.7}Ir_{0.3}$ (thermally formed)	3.75	36	ii
Ru	0.2	38-40	ii
RuO_2-TiO_2/Ti	1.25	40	ii
Vitreous carbon	0.3	120	i
Graphite	1.2	40-120	ii
Fe_3O_4	5.5×10^{-5}	85	-
TiO_2	4.0×10^{-2}	30-120	i
IrO_2	1.17	40	ii
$(RuO_2)_{0.3}(Co_3O_4)_{0.1}(TiO_2)_{0.6}$	0.1	40	-
$Ru_{0.3}Pt_{0.3}Ce_{0.4}O_2$	3.0	32	other
$Ru_{0.3}Pt_{0.7}O_2$	10	31	other
Co_3O_4 (thermally formed)	8.5×10^{-3}	40	other

The activation energy of the reaction steps (catalytic effect) is related to the adsorption strength of the intermediates bonded to the electrocatalyst surface (active sites). RuO_2 is the most widely studied anode materials for chlorine evolution. The investigation of the atomic scale surface catalytic reactivity of RuO_2 reveals that the presence of the coordinatively unsaturated surface sites (*cus*) of *cus*-Ru atoms and bridge-bonded O_{br} atoms are the active sites [17]. Density functional theory calculations indicate that at the RuO_2 (110) surface the adsorption energies of intermediates determine the reaction paths and the selectivity of electrode reaction [12].

Electrode reactions can be charge-transfer controlled and/or mass-transfer controlled. For the charge-transfer controlled process, the rate equation is expressed by the Butler-Volmer equation (Eq. (2.16)). Mass-transfer controlled process can be observed from the polarization curve either at highly applied current density under galvanostatic mode, or at high polarization potential under potentiostatic mode.

2.2.3 Anode electrocatalyst coatings

The electrocatalyst could accelerate the electron transfer at the electrode/electrolyte interface (Figure 2.2). Industrially, electrocatalyst is desired to bring about high current density at lower applied potential, i.e. to obtain high product yield per unit of energy consumption. Electrocatalysts are utilized in the coating form generally in order to maximize the utilization of catalyst materials. A three-phase interface of gas product, solid electrode and aqueous electrolyte exists in the chlorine evolution process. Cl^- ions are oxidized to Cl_2 by the loss the electrons to the anode. The crucial factors for the practical application of the electrocatalysts are the activity (to reduce the overpotential), (chemical, electrochemical and mechanical) stability, selectivity and the cost of catalyst material and manufacturing.

2.2.3.1 Electrode Materials

The expansion in the range of electrode materials is striking during the past 50 years of electrocatalysis [18]. However, the practical applications of electrocatalysts are a compromise between the technical, economic and environmental targets. Besides, the historical fluctuations in the materials cost dominate significantly the selection in electrocatalytic materials. In this regard, noble metals and/or their oxides play a critical role in the past several decades [19,20] and could even remain so for the foreseeable future.

Platinum and graphite were employed as anode materials in the electrolytic chlorine production. The former is expensive and the latter is instable mechanically and electrochemically. The development of the dimensionally stable anodes (DSA) is a revolution in the chlor-alkali industry compared to the prior graphite anode [8,21,22]. It consists of commonly electrocatalytic coating containing platinum group metals or oxides of platinum group metal and valve metal oxides coated onto an electrically conductive valve metal base or alloy containing valve metal, such as titanium, tantalum, nickel and zirconium. Ruthenium dioxide has been recognized as one of the best electrode materials for chlorine evolution reaction. The loss of the electrocatalytic activity of the ruthenium

dioxide caused by the electrochemical dissolution of active ruthenium species depresses the long-term stability of the electrode [23]. In chlor-alkali industry, mixed RuO_2-TiO_2 with TiO_2 as stability promoter is commonly used to inhibit the loss of active component and reduce the material cost of the anode coatings. Due to the same crystal symmetry between RuO_2 and TiO_2, the formation of solid solution is possibly responsible for their durability [24]. The decrease of the ruthenium content below 10 mol% is restricted due to the poor electrical conductivity of the coatings, which contributes to the voltage drop significantly [25].

The electrocatalytic activity of the anode coatings depends on two major factors, the electronic and geometric factors. The former is related to the chemical composition and structure, while the latter to the surface and layer morphology. They are also more often mentioned in another way in the literatures as the true electrocatalytic activity and apparent electrocytalytic activity. Metal or their oxide of platinum group elements such as platinum, iridium, palladium and rhodium has been used as active additives into RuO_2-TiO_2 system to improve the electrocatalytic activity of anode coatings for chlorine evolution. Due to the conflict of technical and economic problems, industrial electrocatalysts prefer the activer and cheaper materials. In contrast to the improvement of the electrocatalytic activity originated from the electronic effect due to the addition of precious metal promoters, less expensive transition metal as additives will contribute to the electrocatalytic activity by geometric factors. The most widely investigated RuO_2-based oxide electrode materials are listed in Table 2.2. S. Trasatti summarized and classified the electrode oxides for chlorine and oxygen evolution reactions into the rutile (RuO_2-based), spinel (Co_3O_4-based), perovskite (NiM_2O_4-based) etc. types [26]. Transition metals have also the potential to show proper individual catalytic activity. The doped multicomponent electrocatalysts are expected to exhibit synergetic effect to improve the activity, stability and selectivity.

Numerous electrode materials exhibit high catalytic activity both for the chlorine evolution and for the oxygen evolution. Note that the oxygen evolution reaction (the anode side reaction for the chlorine evolution, $2H_2O \rightarrow O_2 + 4H^+ + 4e^-$) exhibits a lower standard reversible potential (1.23 V vs. NHE) than the one for chlorine evolution reaction (1.36 V vs. NHE). The former is thermodynamically favoured. However, the exchange current densities of the chlorine evolution reactions are usually substantially greater than those of

oxygen evolution reactions, i.e., the overpotential for chlorine evolution reactions at the anode is lower than that for oxygen evolution reactions. Therefore, chlorine evolution is the dominant reaction during the electrolysis of saturated aqueous NaCl solution in the low pH range of 2~3. The selectivity of anode coatings is evaluated by the electrode potential difference ($E_{O_2} - E_{Cl_2}$) for the O_2/Cl_2 evolution reactions. Further purification of the desired products is necessary in the industrial process.

Table 2.2. Overview of the most investigated RuO_2-based electrode materials for chlorine evolution reaction.

Material	mol % [#]	Preparation route*	Ref.
RuO_2+IrO_2	100	TD	[27]
RuO_2+TiO_2	5~30	TD	[28]
	5~50	TD	[25]
	20	SG	[29]
	40	SG	[30]
	30 [§]	TD	[11]
RuO_2+TiO_2+CeO_2	30	TD	[31]
RuO_2+TiO_2+SnO_2	19~33	TD	[32]
	25	TD	[33]
RuO_2+TiO_2+ CeO_2+Nb_2O_5	30	TD	[34,35]
RuO_2+CeO_2	25~100	SG	[36]
RuO_2+TiO_2+PtO_x	30~100	TD	[37]
RuO_2+TiO_2+$CrNbO_4$	10~20	TD	[28]
RuO_2+TiO_2+Cr_2WO_6	5~7.6	TD	[27]
RuO_2+TiO_2+Cr_2WO_6+$CoWO_4$	1~10	TD	[27]
RuO_2+MnO_2	85	Solid state reaction	[38]
RuO_2/boron-doped diamond	-	SG	[39,40]
RuO_2/areogel-SiO_2	-	Cryogenic decomposition of RuO_4	[41]

[#] Molar percent of noble metal elements;

* TD = thermal decomposition method, SG = sol-gel method;

[§] Commercial DSA electrode.

2.2.3.2 Preparation route of RuO_2-based materials

RuO_2 can be prepared at relatively low temperature (350~550 ^oC) by the thermal decomposition of $RuCl_3$ dissolved in water or alcohols onto an inert metallic substrate such as titanium, tantalum. Mixed oxide can be obtained by adding the additional precursor salts into the coating solutions. This technique is adopted routinely in the chlor-alkali industry. It is known that the oxide layers are not homogeneous in the structure and composition. It contains the non-stoichiometric Ru^{3+} and chloride impurities with the mixed amorphous and crystalline structure. The thermal decomposition process of $RuCl_3$ to form RuO_2 has been analyzed by the EXAFS (extended X-ray absorption fine structure) combined with X-ray diffraction [42]. The simultaneous formation of the Ru-O bonds and the break of Ru-Cl bonds occur at the sintering temperature from 300~400^oC. The change in the coordination number with the calcination temperature was accompanied by the change in the lattice constants. The formation of solid solution has been confirmed for the binary RuO_2-IrO_2 system starting from the thermal decomposition of $RuCl_3$ and $IrCl_3$ inorganic salts.

Sol-gel technique has the potential to replace the traditional thermal decomposition route due to some intrinsic advantages. More intimate mixing of multi-component at molecular scale can be achieved by the hydrolysis and condensation reactions. Different sol-gel preparation routes have been demonstrated, as summarized in Table 2.3.

Single crystal RuO_2 has been prepared by the vapour deposition technique operated at high temperature to investigate the crystal plane dependent electrochemical properties [43,44]. For the rutile structure RuO_2, the metal cations locate at the corners and center of the tetragonal unit cell and each cation is surrounded by six oxygen ions to form an octahedral array. RuO_2 with the (100) or (101) orientation has only Ru atoms at the top plane, whereas, at the (110) orientation plane, both Ru and O atoms present. Besides, the atomic densities of Ru and O and the number of active sites are different for different crystal planes. The kinetics investigation of the chlorine evolution on the RuO_2 (110) and (230) showed that the (230) plane is more active than the (110) plane [45].

Table 2.3. Summary of the sol-gel preparation route to obtain the coating solutions.

Electrode	Precursor(s)	Preparation details	Ref.
$Ru_{0.4}Ti_{0.6}O_2$/Ti	$RuCl_3$, $TiCl_3$	forced hydrolysis of $RuCl_3$ and $TiCl_3$ in HCl solutions separately for different time, then mixing	[30]
$RuIrTiO_2$/Ti	$RuCl_3$, $TiCl_3$, H_3IrCl_6	forced hydrolysis of precursors separately, then mixing	[46]
RuO_2/Ti	$RuCl_3 \cdot xH_2O$	refluxing the mixture of $RuCl_3$ + ethanol + sodium ethoxide, washing the RuO_xH_y precipitate, redispersing the oxide into ethanol	[47]
RuO_2/Ti	$RuCl_3 \cdot xH_2O$	$RuCl_3$+citric acid + ethylene glycol, Pechini route	[48]
$Ce_xRu_{1-x}O_2$/Ti	$RuCl_3 \cdot 3H_2O$ $Ce(NO_3) \cdot 6H_2O$	precursors + alcohol + glycol + citric acid, Pechini route	[36]
$Ru_{0.2}Ti_{0.8}O_2$/Ti	$RuCl_3 \cdot 3H_2O$ $Ti(OC_4H_9)_4$	$RuCl_3$ + n-C_4H_9OH, acetylacetone, $Ti(OC_4H_9)_4$ with controlled adding sequence; then HNO_3 or NH_4OH was added to catalyze the hydrolysis and condensation reactions	[29]

2.2.3.3 Deactivation mechanism of electrode

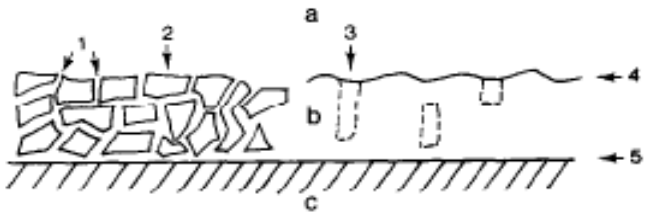

Figure 2.3. Sketch of the morphology of oxide coated electrodes [49]. (a) electrolyte, (b) oxide layer, (c) substrate; (1) grain boundaries, (2) island containing oxide crystallite, (3) pore, (4) electrolyte/coating interface, (5) coating/substrate interface.

The sketch of the cross-section morphology of the oxide layers supported onto the underlying substrate is shown in Figure 2.3. Deactivation mechanism analysis of oxide film coated titanium anodes implies that the dissolution of active component(s) (ruthenium

species) and the growth of insulating TiO_x interlayer between Ti-substrate and oxide layer (shown in Figure 2.4) are responsible for the loss of electrochemical activities [50,51].

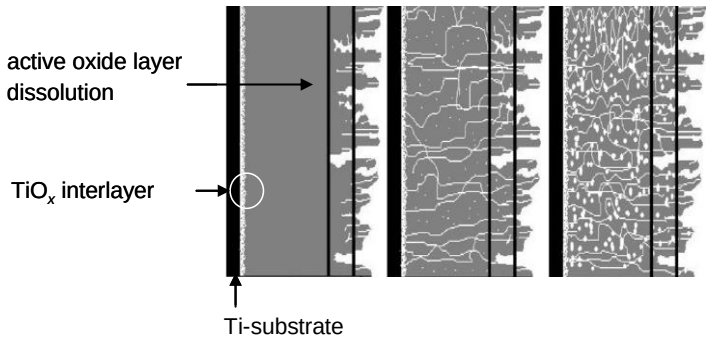

Figure 2.4. Sketch of the DSA® structure with compact catalytic layer or cracky catalytic layer onto the Ti-substrate [51].

Although highly cracky/porous films are favourable in terms of electrocatalytic properties, with respect to the electrode durability a compact and impermeable layer could provide good protection of Ti-substrate from passivation. Various strategies have been developed to prevent the passivation of the substrates caused by the contact with electrolyte in the electrolysis of aqueous solution of sodium chloride or hydrochloric acid. As described in *EP 0046449 A1*, multiple coating/sintering cycles are commonly applied in order to increase the coating thickness and to prolong the service life. The cracks and pores within the first layer are filled by the next applied coating solutions. The amount of inner defects is gradually reduced after each stage of the cycle.

To avoid the formation of the TiO_x interlayers using titanium as substrate, alternative substrates or modified substrates are used. In *WO 2008/046784 A1*, an electrically conductive titanium alloy substrate is used without the deterioration of the electrocatalytic activity. V. Panić et al. describe a Ti_3SiC_2 as anode coating substrate possessing higher corrosion stability than titanium [52]. *EP 0 538 955 A1* describes an anode with semi-conducting oxide interlayer such as titanium suboxide or higher valent metal ions doped titanium oxide. F. Gestermann et al. describe an electrode coating with titanium carbide and/or titanium boride interlayer [53].

2.2.4 Gas evolution and electrochemical noise

Cl^- is oxidized to molecular chlorine by the anodic reactions. As the reactions proceed, bubbles appear in the vicinity of electrode surface with the continuous local release of the supersaturation of dissolved Cl_2 gas in the electrolyte when the convection and diffusion fail to do it [54]. The supersaturated electrolyte recovers the stable thermodynamic state by transferring the excess of dissolved gas molecules into vapour phase [55].

Gas bubble evolution includes a series of events such as bubble nucleation, growth, coalescence, detachment and lingering in the vicinity of electrode surface, which causes the chaos and turbulence of the electrochemical system. Bubble nucleation may occur within the liquid bulk in a manner of homogeneous nucleation or on a rough surface in a way of heterogeneous nucleation. The latter is the case of gas evolving on the electrode surface. Once a tiny bubble is formed at the nucleation sites at the surface of electrode, a gas/liquid meniscus interface is created. The concentration gradient of dissolved Cl_2 between the liquid bulk and the bubble surface is the driving force responsible for the gas molecules diffuse through the meniscus interface, which results in the growth of bubble. The bubble is anchored to its nucleation sites and keeps growing. When the buoyancy force overcomes the capillary force anchoring the bubble to the nucleation sites, the bubble detaches and ascends upward [56].

Under the supersaturated conditions, Ostwald ripening occurs when the disperse phase of gas bubbles is slightly soluble in the continuous phase of electrolyte, wherein the driving force is Laplace pressure (for a spherical bubble, $P_L = 2\gamma / r$, where γ is the interfacial tension, and r is the bubble radius) [57]. Consequently, smaller bubbles decrease in size, while larger bubbles get larger as the gas diffuses from smaller to larger bubbles. This phenomenon is known as the Kelvin effect for gas in liquid. The large bubbles grow at the expense of the small ones. The bubble size distribution becomes broader. On the other hand, the bubble coalescence occurs when the film between the bubbles ruptures. Subsequently, the Laplace pressure drives the bubbles to form a larger single bubble. Thus the coalescence results in the disappearance of the dispersion. The coalescence by film rupture can be caused by thermal fluctuations ($\sim k_B T$) or mechanical agitation.

The bubble evolution is a remarkably practical problem in terms of the loss of energy in the chlor-alkali industry. Usually, the potential drop across the electrolyte is calculated using Ohm's law if the medium is homogenous. However, if the gas bubbles are generated at the electrode interface, the current *lines* go around the insulating gas bubbles, the specific conductivity of the medium decreases and accordingly the increase in ohmic drops. The technical data from the De Nora mercury cells show that the gas bubble effects contribute ca. 4% of the total cell voltage [6]. The ohmic resistance dependence on the electrode configurations (vertical, horizontal upwards or downwards), current densities and bubble froth layer thickness has been investigated by Kiuchi et al [58]. Numerous efforts of theoretical analysis and experimental observation have been made upon the electrochemical gas evolving electrodes [59]. As a matter of fact, it is very delicate to get a comprehensive understanding for the complex electrode process. To simplify, tractable model and experimental setup are designed purposefully to isolate the individual effect concerned to the electrode process. The characteristic parameters of bubbles such as the residence time, the size and size distribution of detached bubbles have been determined by using see-through cells with the help of video camera and laser Doppler velocimetry [60, 61]. The electrochemical events of gas bubble evolution occurred on the electrode surface (and vicinity of electrode surface if froth layer is taken into consideration) cause the chaos of the electrochemical system. As an alternative of the optical technique, the analysis of the electrochemical signal fluctuation (fluctuation of potential or current signal) is a powerful tool in the monitoring of electrochemical events occurred on the electrode surface.

Considerable attention has been paid to the electrochemical noise signals analysis in the fields of corrosion studies [62], electrode process in lithium batteries [63], estimating the electrode surface morphologies using electrochemical noise data [64]. Electrochemical noise analysis is also being used to extract information of gas evolving behaviour on the electrode/electrolyte interface. The characteristic parameters such as bubble size, detachment rate can be deduced from the noise data by using suitable noise analysis techniques [54]. The amplitude and shape of the signal fluctuations can be correlated with the electrochemical events occurred. The signal analysis is mainly based on the mathematic algorithms and computerized data processing. Different approaches have been proposed for the noise data analysis: statistical, spectral and chaos theory-based methods [65].

2.3 Sol-gel synthesis

The sol-gel process is a versatile solution-chemical process widely used in the fields of materials science and ceramic engineering. The sol-gel methods are used primarily for the preparation of metal oxides starting from a chemical solution which acts as the precursor for the build-up of metal oxide networks. The starting materials used typically in the preparation of the sol are usually inorganic metal salts or metal organic compounds such as metal alkoxides, which undergo various forms of hydrolysis and polycondensation reactions. The formation of a metal oxide involves the connection of metal ion centers with oxo (-O-) or hydroxo (-OH-) bridges. Thus the metal-oxo or metal-hydroxo bonds are generated in the colloid solution (sol). The transition of the liquid sol into a solid phase (gel) by removing the liquid solvent requires a drying process, in which the significant shrinkage and densification of the network occur. Afterwards, a post-sintering process is often necessary in order to favour the further polycondensation and enhance the mechanical properties and structural stability for the final practical applications.

Applying the sol-gel process, it is possible to fabricate ceramic materials in a wide variety of forms: ultra-fine powders, thin film, coatings, ceramic fibers, microporous inorganic membranes, or extremely porous aerogel materials. One of the distinct features of the sol-gel technique compared to the conversional solid state reactions or thermal decomposition routes is the molecular-scale structural homogeneity, especially for the preparation of mixed oxide materials. Moreover, the structural densification is often achieved at a relative low sintering temperature.

2.3.1 The hydrolysis and condensation reactions

The preparation of SiO_2 by sol-gel technique is the most thoroughly investigated process, which can be traced back to 1880s since the first observation of the hydrolysis reaction of

tetraethyl orthosilicate ($Si(OC_2H_5)_4$, or $Si(OR)_4$ where R = C_2H_5, abbreviated as TEOS) under acidic conditions.

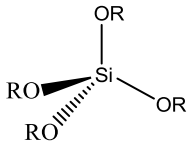

The $Si(OR)_4$ forms a stable solution in the absence of water. The introduction of water into the system initiates the hydrolysis reactions by the nucleophilic attacks. The first step hydrolysis reaction occurs by replace one OR group with one OH group, as follow:

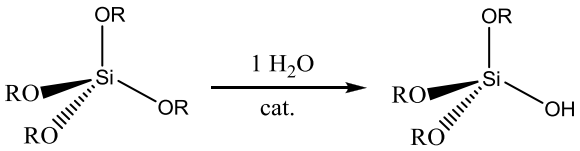

Depending on the amount of water and catalyst present, hydrolysis reactions may proceed to completion (the leftmost path in Figure 2.5), so that all of the OR groups are replaced by OH groups, as follows:

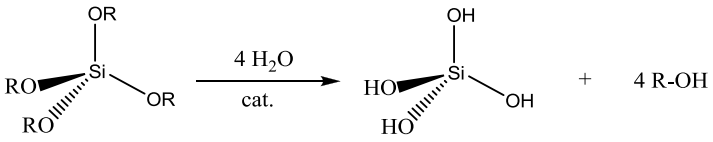

A series of intermediate species $Si(OR)_n(OH)_{4-n}$ would be produced as the result of partial hydrolysis. Variation in the number of *n* has profound consequences for the morphology and structure of the resulting Si-O-Si networks.

The first step condensation occurs after the first step hydrolysis reaction by linking two $Si(OR)_3(OH)$ molecules (nucleophilic substitution) and releasing one molar H_2O to form the first Si-O-Si bond in the colloid solution. Afterwards, the successive and overlapped hydrolysis and condensation reactions proceed to form the three-dimensional Si-O-Si macromolecule networks. The competitive hydrolysis and condensation reactions would dominate the final network towards linear (the rightmost path in Figure 2.5, low water concentration or slow hydrolysis rate) or branched structure (the middle paths in Figure 2.5), which is one of the most critical aspects of sol-gel process.

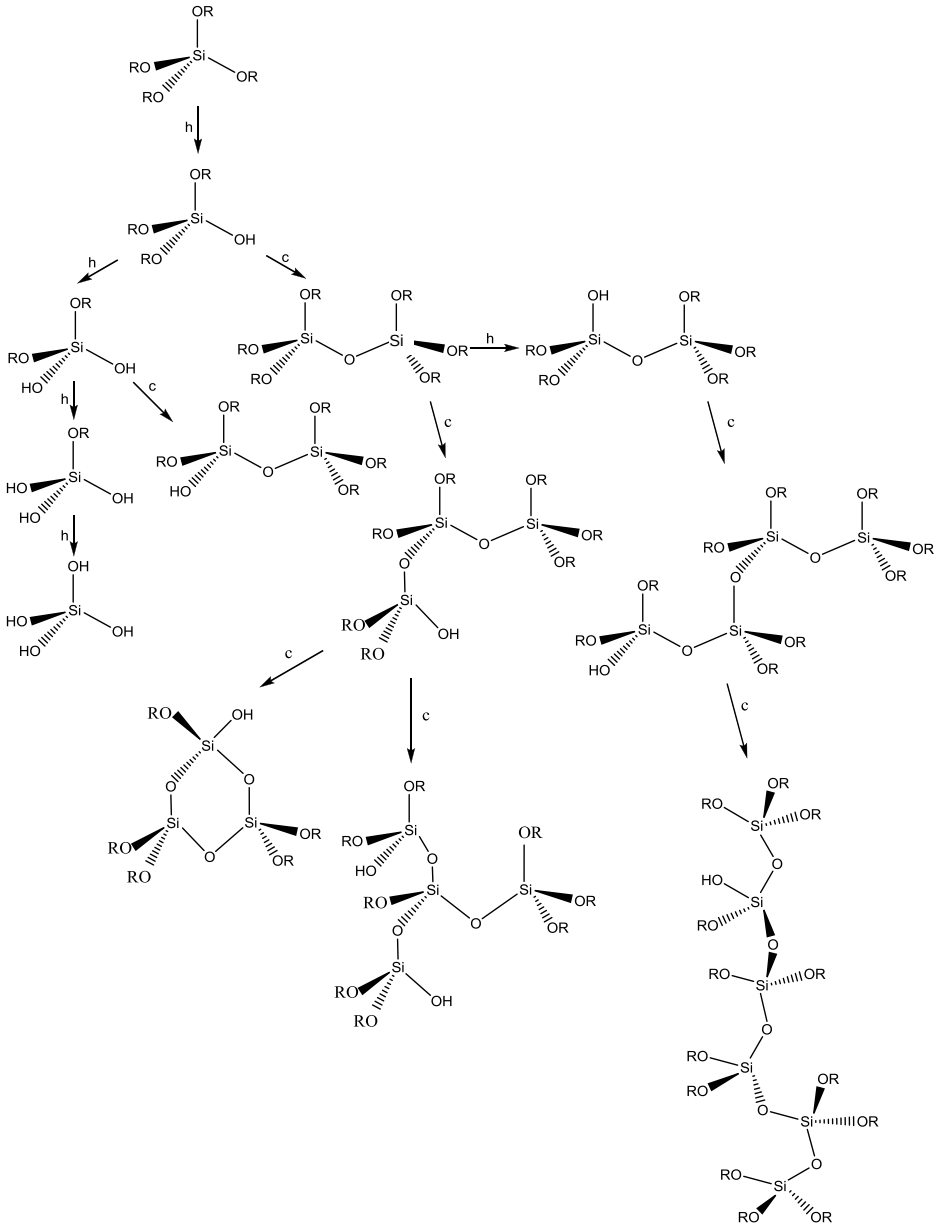

Figure 2.5. The formation of O-Si-O networks from the precursor $Si(OR)_4$ by the successive and overlapped hydrolysis (h) and polycondensation (c) reactions.

The oxidation state ($z = 4$) and coordination number ($N = 4$) of silicon are equal. However, in this case of $z < N$, such as the sol-gel process of vanadium pentoxide (V_2O_5) started from the sodium metavanadate aqueous solution ($NaVO_3$), the coordination expansion occurs owing to the attack of nucleophilic reagents [66]. After acidification performed through ion exchange, the colorless solution turns into yellow solution of vanadic acid. The H_3VO_4 (or $VO(OH)_3$) is obtained by further aging, and the coordination expansion of $VO(OH)_3$ occurs via the nucleophilic addition of two molar H_2O giving the hexa-coordinated

$VO(OH)_3(OH_2)_2$, in which one molar H_2O attached to V ion center along the *z* axis opposite to the VO double bond, the second one is in the direction of *y* axis opposite to an OH group.

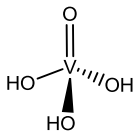

H_3VO_4

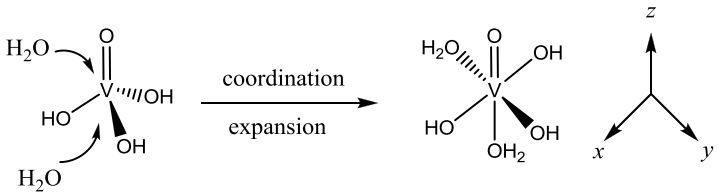

$VO(OH)_3(OH_2)_2$

A distinct feature of the condensation reaction is that it cannot proceed along the *z* axis. Fast olation reactions (a condensation process in which a hydroxyl bridge is formed between two metal centers, M-OH-M') along the *y* axis give rise to corner sharing chain, nevertheless, the oxolation reactions (a condensation process in which an oxo bridge is formed between two metal centers, M-O-M') along the *x* axis result in the edge sharing double chains. The difference in the linkage manner of the basic building-block based on the controllable hydrolysis and condensation reaction rate is a prominent nature of the sol-gel process, which is particularly important for the preparation of desired structure of metal oxide with respect to the oxide with various polymorphs.

A similar effect has been demonstrated for the titanium (IV) isopropoxide ($Ti(O^iPr)_4$). TiO_2 is another class of material particularly important in the sol-gel chemistry. Titanium dioxide (TiO_2) exists in nature as rutile, anatase and brookite. The crystalline form, size, and morphology of titania are critically important with reference to its performance for most of the applications. The microstructure and the related properties could be well modulated by various parameters in the sol-gel chemistry, such as solution pH, chelating reagent, the nature of the precursor.

The lower the electronegativities of the transition metals, the more susceptible are their alkoxides against the hydrolysis. Complexing ligands such as bidentate acetylacetonate

(acac) can be used to slow down the fast hydrolysis and condensation reactions. For the preparation of mixed oxide, the complexing ligands could control the competitive hydrolysis and condensation reaction rates of the different precursors.

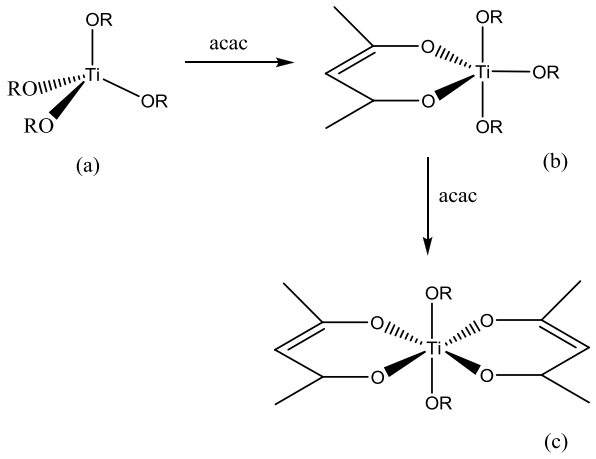

Figure 2.6. Partial substituation of $Ti(O^iPr)_4$ (a) by acac. One or two O^iPr^- ligands is substituted by acac to form $Ti(O^iPr)_3(acac)$ (b) and $Ti(O^iPr)_2(acac)_2$ (c) [67].

The analogous ligand displacement can also be obtained by using organic acids, such as formic acid, acetic acid, propionic acid and butyric acid [68]. The alkyl-peroxo complexes $Ti(OOR)_n(O^iPr)_{4-n}$ (R = Me, Et, Pr, Bu, etc.) are produced in this case and the organic acid acts as solvent for the precursors simultaneously.

The basic building-block of the various TiO_2 polymorphs is octahedral TiO_6. The rutile phase is characterized by linear chains of TiO_6 octahedra that share a pair of opposite edges, while in anatase a TiO_6 octahedron shares four edges with its neighbors to form the zigzag ribbon structure. In the brookite phase, three edges of TiO_6 octahedron are shared by other octahedra.

2.3.2 The formation of sol-gel coatings

The formation of films is one of the most important aspects of the sol-gel process. Various techniques such as dip coating, spin coating, brush coating, spray coating have been applied to obtain the desired film structures and properties. The simple coating technique facilitates the up-scaling operation for large scale application in industrial process. The substrate with various complex geometric shapes such as mesh, rod, and foam can be deposited with the particulate precursors by liquid-based coating techniques.

The preparation of the coating solution, the selection of the coating technique, and the control of the post treatment conditions are critical factors in tailoring the resulting coating structure and performance. Composite oxides can be obtained by doping and mixing the corresponding precursor salts into the coating solutions. The stable coating solution, which can be exposed to air and moisture without the formation of sediments, is very important for the practical application. The coating thickness, microstructure and morphology can be well controlled by using suitable coating technique. The crystallization route of the initial amorphous materials could determine the final phase structure, phase composition. Therefore, the electrocatalytic properties of sol-gel oxide coatings can be governed effectively by controlling the preparation parameters and details.

2.3.3 The drying and post-sintering

After applying the wet coating solution onto the substrates, the subsequent thermal treatment steps (drying, sintering) are followed to densify the films and finish the crystallization transformation of the initial amorphous structure. As liquids evaporate from the wet gel films during the drying process, the M-O-M' networks begin to shrink by expelling the liquids towards the exterior in order to balance the capillary tension (see Figure 2.7). For sol-gel films deposited onto a substrate, the networks shrink more on the drying side and warping occurs, as observed in Figure 2.8. The difference in shrinkage rate between the inside and outside of the gel body, and the mismatching of the thermal

expansion coefficient between the substrate and the film are the cause of tensile stress (see Figure 2.8).

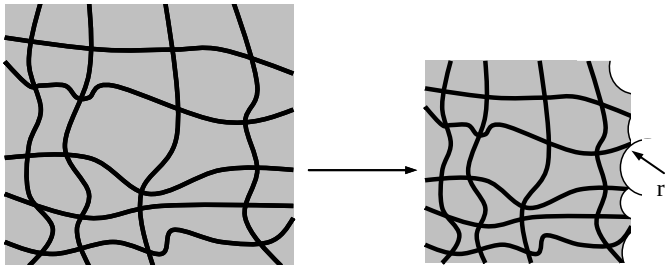

Figure 2.7. Schematic illustration of the shrinkage of gel networks during the drying process [69]. The initial networks (left) lose liquid and accordingly the capillary tension develops in the liquid (right, *r* is the radius of the meniscus, which is related to the radius of pore, *a*, and the contact angle, θ) and draws back the network into the liquid until the network stiffens.

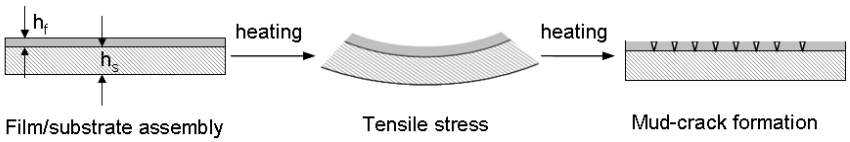

Figure 2.8. Tensile stress evolution and crack formation in gel films under heat-treatment (such as drying and sintering) [70].

For the film/substrate assembly structure (Figure 2.8) with given substrate (material and thickness), the tensile stress (σ) in coatings is associated with the thickness of oxide coatings (h_f) according to Stoney's equation:

$$\sigma = \frac{E_s}{6(1-\nu_s)} \frac{h_s^2}{h_f} \left(\frac{1}{R_2} - \frac{1}{R_1}\right) \tag{2.20}$$

where E_s and ν_s are elastic constant and Poisson's ratio of substrate, respectively, h_s and h_f are thickness of substrate and coating, respectively, R_1, R_2 are the radii of curvature of the substrate before and after deposition. Note that thinner coating and lower tensile stress will reduce the difference between R_1 and R_2 and depress the possibility of crack formation.

Kozuka et al. [70, 71] have demonstrated that crack-free thick films (> 1 μm) can be obtained by the single-step dip-coating method by using poly(vinylpyrrolidone) (PVP) as stress-relaxation agent. The idea behind is to retard the condensation reactions (which results in the gel pore collapse under heat-treatment) and simultaneously to promote the structural relaxation through strong hydrogen bonding interaction between the C=O groups of the PVP and the OH groups of the gel bodies. Stepwise heat treatment was executed and a sintering temperature up to 700 ^{o}C was used to decompose the PVP. However, the preparation of crack-free coatings using PVP-containing sol solution is not suitable in this work because the complete decomposition of PVP is difficult, especially when the single layer is thick (> 1 μm). Note that for the preparation of titanium supported oxide electrode coatings, high sintering temperature (>500 ^{o}C) has to be avoided due to the possible formation of the insulating TiO_x interlayer. Besides, the existence of the residual PVP in the oxide matrix as contaminants could cause negative effects, such as the influence in oxide layer conductivity, electrochemical stability.

2.4 Experimental methods

2.4.1 Structural characterization

For the substrate supported electrocatalyst, the most commonly used technique to disclose the structure and surface information are the diffraction techniques (X-ray diffraction, electron diffraction, neutron diffraction), electron microscopic techniques (SEM, TEM), and vibrational spectroscopic techniques (IR, Raman).

2.4.1.1 X-ray diffraction

In 1895, W.C. Röntgen (a German physicist) discovered the X-rays. In 1921, M. v. Laue (a German physicist) discovered that X-rays can be diffracted or scattered by the orderly arrays of atoms in a crystal. The three-dimensional atomic arrangement in a crystal is deduced from the directions and intensities of the diffracted X-ray beams. Crystalline material can be considered as an infinite recurrence of parallel atomic planes with an interplanar distance *d*. When a beam of monochromatic X-rays is incident on the atoms in a crystal, the wavelets scattered by the atoms in each plane combine to form a reflected wave. The interference patterns of the scattered radiation are recorded by a detector. The interference is constructive when the Bragg condition for diffraction is fulfilled, i.e., $n\lambda = 2d\sin\theta$, where n is diffraction order, λ is X-ray wavelength, θ is Bragg angle or incident angle.

The X-ray diffraction patterns allow the qualitative and quantitative crystal structure characterization concerning the crystallite size and distribution, phase composition and percentage, lattice parameters from the position, intensity (which depends on the type of atoms in the elementary cell and their positions, site occupancy, scattering factor etc.) and shape of the diffraction peaks. The volume-weighted crystallite size (*D*, the mean size of the ordered domains or the mean dimension of the coherently diffracting domains) can be estimated from the main diffraction peak by using Scherrer's equation:

$$D = \frac{0.9\lambda}{\beta \cdot \cos\theta} \tag{2.21}$$

where λ is the X-ray wavelength, β is the full width at the half-maximum intensity (FWHM) in radians, and θ is the Bragg angle.

Various factors can result in the peak broadening, such as the crystallite size (which is caused by the finite size of domains diffracting essentially incoherently with respect to one another), instrumental distortion, lattice microstrain (which is caused by the displacements of the atoms with respect to their reference-lattice position) [72, 73]. In contrast, the Warren and Averbach's method, which is based on the Fourier deconvolution of the measured peaks and the instrument broadening since the measured peak profile is actually the convolution of a function for the pure peak profile and a function of the instrumental broadening, is capable of providing the information of area-weighted crystallite size, crystallite size distribution and lattice microstrain. Rietveld refinement analysis [74], which uses a least-squares fit approach to refine a theoretical line profile until it matches the measured diffraction profile, is a powerful tool for quantitative phase analysis. More reliable structure parameters, crystalline components can be obtained.

2.4.1.2 Scanning electron microscopy (SEM)

For particles with sizes down to nanometer~submicrometer, it is essential to use electron microscopy rather than optical microscopy to examine them. The sample surface topography can be visualized by scanning it with a high-energy beam of electrons (typical energy range 5~20 keV) in a raster scan pattern. Secondary electrons (generated by inelastic scattering during the energy exchange between the electron beam and the sample) are the common type to produce the SEM signals by the interactions between the electron beam and the atoms at or near the sample surface. The size of the interaction volume depends on the electron energy, the atomic number of the specimen and the density of the specimen.

2.4.1.3 Energy dispersive X-ray spectroscopy (EDX or EDS)

EDX coupled with SEM analysis is used to obtain the qualitative element analysis from the emission of characteristic X-rays from a specimen when a material is bombarded with electrons in an electron beam instrument. When the sample is bombarded by the electron beam of the SEM, electrons are ejected from the atoms comprising the sample surface. A resulting electron vacancy is then filled by an electron from the higher shell, and an X-ray is emitted to balance the energy difference between the two electrons. The EDX X-ray detector counts the emitted X-rays and measures their energy.

2.4.1.4 Transmission electron microscopy (TEM)

TEM is an imaging technique with a significantly higher resolution than light microscopes owning to the small de Broglie wavelength of electrons. A beam of electrons (typical energy range 100~400 keV) is transmitted through an ultra thin solid sample, interacting with the specimen. The transmitted beam containing information about the electron density, phase, and periodicity is used to form an image.

2.4.1.5 Selected area electron diffraction (SAED)

SAED is a crystallographic technique, coupled with TEM to obtain the information of spots of interest from the TEM images. In this case high-energy electrons pass through the specimen, electrons with a wavelength of a fraction of a nanometer, and the spacing between atoms in a solid is slight larger than the electron wavelength. Thus the atoms act as a diffraction grating to the electrons. Part of the electrons will be scattered, determined by the crystal structure of the sample, while others pass through without deflection. As a diffraction technique, the SAED can be used to identify the crystal structures and study the crystal defects in an area as small as several hundred nm. The crystal structure, lattice parameters of the unit cell can be deduced from the reciprocal lattice of the sample crystal.

2.4.1.6 Raman spectroscopy

In the Raman technique, the sample is illuminated with monochromatic light, usually generated by a laser. Two types of scattered light are produced. Rayleigh scattering emerges with exactly the same energy and wavelength as the incident light. Raman scattering, which is usually much less intensive then Rayleigh scatter, emerges at either longer or shorter wavelength than the incident light. As a consequence, the vibrational transition of frequency was reflected from the Raman lines. Each peak in a Raman spectrum corresponds to a particular vibrational transition. For inorganic solids, the lattice vibrations give rise to peaks in the region about 100~700 cm^{-1}. Raman spectroscopy is sensitive to the small lattice vibrations in inorganic solid even with very low phase fractions. In contrast, X-ray diffraction patterns could provide information about the long-range order. Raman spectroscopy gives more reliable information than X-ray diffraction when applied to local structural analysis of inorganic materials. Due to the difference in principal selection rules, the active modes in Raman spectra and IR are different. They produce complementary information. The vibrational mode to be Raman active is that the vibrations involved must produce a change in polarizability [75].

2.4.2 Electrochemical characterization

2.4.2.1 Cyclic voltammetry (CV)

Cyclic voltammetry is used for obtaining qualitative information about the electrochemical reactions of an electrode surface, such as the redox processes, heterogeneous electron-transfer reactions or adsorption processes. It offers a rapid location of redox potential of the electroactive species or a current response at the working electrode as a function of the applied potential. The current response is monitored during the potential sweep (Figure 2.9). The potential sweep range (E_{min}~E_{max}) and the sweep rate can be controlled experimentally. Additionally, CV can provide information about the reversibility of the charging/discharging process.

Cyclic voltammetry can produce informative characterization of oxide coatings if taken in conditions where no Faradaic process occurs and the solvent is not electrochemically decomposed. A non-faradaic process involves the accumulation of charges at the metal/solution interface, which is called the electrical double layer. However, Faradaic processes are associated with electron transfer across the interface, result in redox of species. The shape of the voltammograms provides evidence of intermediate species, surface redox transitions or phase formations.

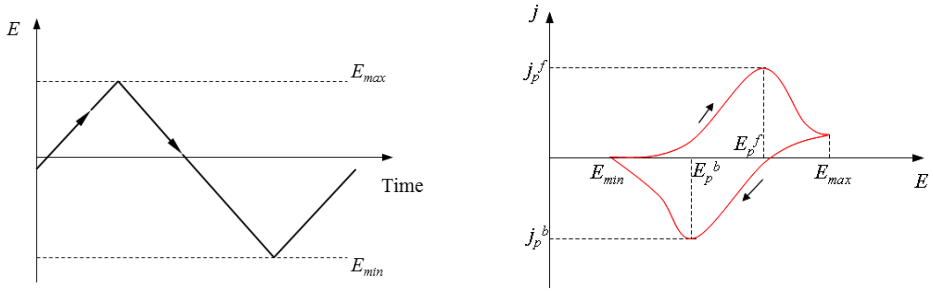

Figure 2.9. (left) The triangular potential sweep waveform (one cycle is shown) used for the CV measurement. (right) The typical cyclic voltammogram recorded corresponding to the potential sweep.

To investigate the capacitor-like behaviour of oxide electrodes, the voltammetric charge density (q_a) can be obtained by graphical integration of the voltammograms in the potential range without the Faradaic reaction and calculated by using the equation:

$$q_a = \frac{S}{\nu} \tag{2.22}$$

where S, (mA V cm^{-2}) is the integrated area of the anodic branch, and υ, (mV s^{-1}) is the potential sweep rate. It provides some diagnostic criteria to assess the morphology and evaluate the relative electroactive surface area of oxide electrodes, assuming that the voltammetric charge density is proportional to the surface concentration of active sites. The dependence of the voltammetric charge density on the sweep rate could provide information about the oxide coating morphology.

2.4.2.2 Chronopotentiometry (CP)

The electrocatalytic activity of the electrode coatings can be evaluated in a relative way by comparing the electrode potential for a given constant current density (termed as chronopotentiometry). The CP measurement is performed generally by stepping from an initial current, typically zero, to some finite value (left in Figure 2.10) and monitoring the potential vs. time (right in Figure 2.10). The overall redox reaction rate (current density) is fixed, and the potential of the working electrode is then monitored as a function of time. Generally, the CP curves contain plateaus that correspond to the steady-state redox potential of electroactive species. The analysis of the noise in the recorded potential signal can help the identification of the physico-chemical process associated with the noise source at the electrode surface.

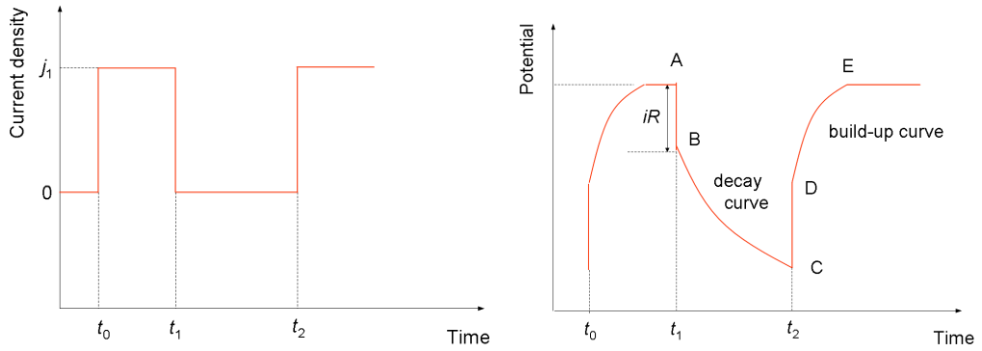

Figure 2.10. (left) Current excitation signal for a chronopotentiometry measurement with an interrupt from t_1 to t_2. (right) Potential-time profile for the CP measurement corresponding to the current signal.

For the CP measurement with a current interrupt, the potential response vs. time is shown in the right panel in Figure 2.10. The current is interrupted at time t_1, the potential drops from the steady state A to B instantaneously with a potential difference of iR and then decays with time. The potential decay curve is also called as potential relaxation curve. After sufficiently long time, the potential will decrease to the open circuit potential. At time t_2 the current is applied once again, the potential jumps immediately and then increases non-linearly until reaches again the steady-state value. The potential build-up

curve is also called as pseudocapacitor charging curve or potential transient curve. The decay process and charging process are non-steady-state processes. Note that both the charging/discharging of the double layer and the Faradaic process contribute to the non-steady-state process. The characterization of the rough or porous electrode surface can be carried out by analysing the charging/discharging behaviour at the electrode/electrolyte interface. Note that the double-layer capacitance arises from the electrostatic charging of the electrode surface, whereas the pseudocapacitance involves the electrochemical adsorption/desorption of reactive species along with the electron transfer [76].

2.4.2.3 Galvanostatic polarization

The *E-I* polarization curves of a given electrode can be measured either galvanostatically or potentiostatically. The former measures the potential under steady-state conditions by applying a constant current. The latter records the steady-state current by imposing a constant potential. Prior to the polarization measurement, the electrode should be activated firstly. For the galvanostatic polarization measurement, current is applied stepwise with or without intermediate current interrupt (Figure 2.11). The parameters for the experiments are the current value and the length of the current steps (current interrupt is optional). This Tafel slope can be determined from the polarization curves (potential vs. log-current curves) after the *iR*-correction.

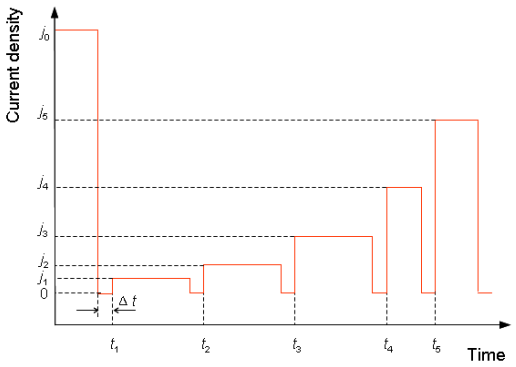

Figure 2.11. Current steps profile for the galvanostatic polarization measurements. Electrodes were activated at current density, j_0, for a certain time before starting the current steps (j_1, j_2,…).

2.4.2.4 Electrochemical impedance spectroscopy (EIS)

Impedance spectroscopy (IS) is a powerful tool for the investigation of frequency-dependent electrical properties of materials and their interfaces. The Electrochemical impedance spectroscopy (EIS) measurements are performed by applying a stimulus current (or potential) to the electrode and observing the potential (or current) response at different frequency. In a galvanostatic impedance measurement, the monochromatic excitation current, expressed as a function of time, has the form $I_t = I_0 \sin(\omega t)$, where I_t is the current at time t, I_0 is the amplitude of the excitation signal, and $\omega = 2\pi f$ is the angular frequency. For a linear electrochemical system, the resulting potential response, $E_t = E_0 \sin(\omega t + \phi)$, is shifted in phase ϕ. The complex impedance $Z(\omega)$ is obtained from the complex potential and current, $Z(\omega) = \frac{E_t}{I_t} = Z_{re} + iZ_{im}$, where $i = \sqrt{-1}$. The impedance is therefore expressed in terms of a magnitude $|Z|$ and a phase shift ϕ. The most common representation of impedance data is the Nyquist-plot ($-Z_{im}$ is plotted versus Z_{re}) or Bode-plot ($|Z|$ and ϕ are plotted as a function of log frequency).

For an electrode-solution interface with the occurrence of a Faradaic charge-transfer reaction, which is controlled by the charge-transfer step, an equivalent circuit $R_e(R_{ct}C_{dl})$ is normally used to represent the interface, where R_e is the solution resistance, R_{ct} is the charge-transfer resistance, and C_{dl} is the double layer capacitance. More than one semi-circle could present from the Nyquist plot for a complex system. For the porous or rough electrode surface, a suppressed semicircle in the Nyquist plot originating from the frequency dispersion of the interfacial impedance can be observed. A constant phase element (CPE) is often used to replace the capacitance element. When the electrode reaction is controlled by the mass-transfer step, the Warburg element (W) can be involved in the equivalent circuit. Accordingly, the Warburg straight line can be observed in the low frequency region of the Nyquist plot.

3 Experimental

This section contains the experimental details regarding the electrocatalyst preparation by sol-gel based routes, followed by the structural characterization and electrochemical performance analysis of electrocatalysts for chlorine evolution reactions.

3.1 Preparation of electrocatalyst coatings

3.1.1 Pre-treatment of Ti-substrates

Titanium plates with a diameter of 15 mm and a thickness of 2 mm (Goodfellow, purity: 99.6%) were sandblasted (one side) and etched in 10% oxalic acid at 80 °C for 2 h to clean and roughen the surface and then rinsed with isopropanol and dried in a nitrogen flow. Afterwards, the titanium substrates were freshly coated with sol solutions. For up-scaling, expanded titanium metal (100×100 mm^2) used as substrates were pre-treated by following the same procedure.

3.1.2 Sol-gel synthesis of mixed oxide coatings

All chemicals used were listed in *Appendix* A1 and applied without further purification. Two different routes of acetic acid and propionic acid catalyzed sol-gel procedures were applied to prepare the sol solutions.

3.1.2.1 $RuTiO_2$ sol solutions prepared by acetic acid-isopropanol route

The general sol-gel recipe used to prepare 0.1125 M $RuTiO_2$ binary oxides is as follows. The molar ratio of precursors, chelating agent, acetic acid and water is:

$$Ru : Ti : DAA : CH_3COOH : H_2O = n : (1\text{-}n) : 3 : 6/40 : 1$$

where DAA is 4-hydroxy-4-methyl-2-pentanone, synonym: diacetone alcohol; *n* is the molar content of ruthenium in $RuTiO_2$ binary oxide.

Addition sequence:

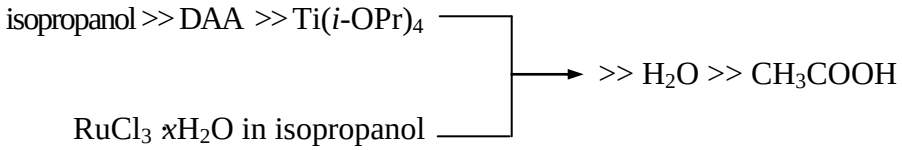

Embodiment of the preparation procedure: The preparation of 0.1125 M $Ru_{0.4}Ti_{0.6}O_2$ sol solutions, for example, were obtained by dissolving 168.5 mg $RuCl_3$ *x*H_2O (36% Ru) (0.6 mmol Ru) into 6 mL isopropanol, and stirred overnight (Solution A). 266.5 µL Ti(*i*-OPr)$_4$ (0.9 mmol Ti) was added into the premixed solution of 561.5 µL (4.5 mmol) 4-hydroxy-4-methyl-2-pentanone in 6.47 mL isopropanol (Solution B) and keep stirring for 30 min. Solution A and Solution B were ultrasonically mixed to acquire a clear solution. Afterwards, 27 µL deionized water (1.5 mmol) and 12.9 µL acetic acid (0.225 mmol) were added into the above solution. The as-prepared solution was covered and kept stirring overnight at room temperature.

3.1.2.2 $RuTiMO_x$ sol solutions prepared by propionic acid-isopropanol route

The general sol-gel recipe used to prepare $RuTiMO_x$ multicomponent oxides is carried out by using hot isopropanol and propionic acid mixture (1 : 1 in volume) as co-solvents to dissolve the precursor salts for the preparation of $RuTiMO_x$, where M is doping element such as Ir, V, Sn, Mo, Zr etc.

Embodiment of the preparation procedure: The preparation of 0.1125 M $Ru_{0.1}Ir_{0.1}V_{0.05}Sn_{0.4}Ti_{0.35}O_x$ sol solutions, for example, were obtained by adding 49.8 mg Ru(acac)$_3$ (0.125 mmol), 61.2 mg Ir(acac)$_3$ (0.125 mmol), 16.6 mg VO(acac)$_2$ (0.0625 mmol), 207.6 mg Sn(*i*-OPr)$_4$ C_3H_7OH (0.5 mmol) and 129.5 µL Ti(*i*-OPr)$_4$ (0.4375 mmol) into 1.11 mL isopropanol and 1.11 mL propionic acid mixture, respectively. The above solutions were refluxed at 150 °C for 30 min with vigorous stirring and then

mixed after cooling down to room temperature. The mixed solutions were homogeneous and transparent with wine-red colour.

3.1.2.3 Preparation of Ti substrates supported oxide coatings

Titanium plates were drop-coated with 50 µL coating solutions (0.1125 M) using a micropipetter. The wet coatings were air-dried and sintered at 250 °C for 10 min and then 450 °C for 10 min in static air conditions. The dropping/drying/sintering cycle was repeated 8 times, corresponding to a total metal loading amount of 45 µmol per Ti-plate (1.77 cm^2 geometric surface area). After deposition of the final coating (the 8^{th} coating), the coated titanium plates were sintered at 450 °C for another 1 h to finish the preparation process.

3.1.3 Preparation of crack-free coatings

The crack-free and impermeable coatings were obtained by repetitious soaking-withdrawing technique after obtaining the sol solutions. The photograph of home-made dip-coater is shown in Figure 3.1.

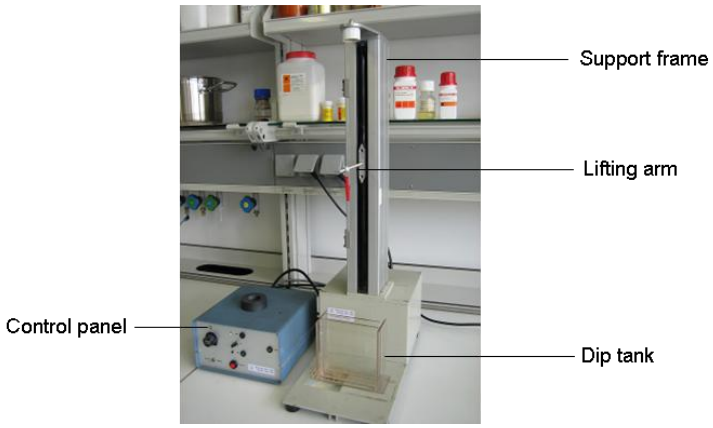

Figure 3.1. Image of the home-made sol-gel dip-coater device. The lifting arm movement speed can be changed by each 1 mm min^{-1} and with a maximum of 200 mm min^{-1}.

The titanium substrates were immersed in the coating solutions for 20 s and then withdrawn upwards vertically from the coating solutions with a controlled withdrawal

speed. The wet coatings were air-dried and sintered at 250 °C for 10 min or 90 °C for 30 min and then 450 °C for 5 min in static air conditions. The soaking-withdrawing-drying-sintering cycles were repeated many times in order to obtain thicker crack-free coatings. The single layer thickness of oxide coatings can be changed by the withdrawing speed and the concentration of sol solutions.

3.1.4 Preparation of porous coatings

The coating solutions were obtained by adding a certain amount of $La(NO_3)_3 \cdot 6H_2O$ or polyvinylpyrrolidone (PVP) into the sol solutions prepared as described above. The coating processes were same as described before. Pores were created by chemical leaching (soaking the coated titanium plates into the 5% HCl aqueous solution, at a temperature of 60 °C for 15 min with slight stirring) for the coatings prepared from La-containing sol solutions or by organics burning for the coatings prepared from the PVP-containing sol solutions.

Embodiment of the preparation procedure: To prepare $Ru_{0.3}Sn_{0.7}O_2$ porous coatings, for example, the coating solutions were obtained by dissolving 37.9 mg $RuCl_3 \cdot xH_2O$ (36% Ru) (0.135 mmol) into 1.33 mL isopropanol, and keep stirring overnight (Solution A). 130.8 mg Sn(*i*-OPr)$_4$ C_3H_7OH (0.315 mmol) was added into the mixture of 1.34 mL isopropanol and 1.33 ml propionic acid, and then refluxed at 150 °C for 30 min with vigorous stirring (Solution B). Afterwards, 39 mg $La(NO_3)_3 \cdot 6H_2O$ (0.09 mmol) was added into the hot Solution B and kept stirring for another 20min until the solutions cool down to room temperature. Finally, Solution A was added dropwise into the above solutions with vigorous stirring. The titanium plates were drop-coated with 50 μL coating solution using a micropipetter. The wet coatings were air-dried and sintered at 250 °C for 10 min and then 450 °C for 10 min in static air conditions. The coated titanium plates were soaked in the 5% HCl aqueous solution, at a temperature of 60 °C for 15 min with slight stirring to leach away the lanthanum oxide. The coating-sintering-leaching cycle was repeated for 8 times, corresponding to a total ruthenium loading amount of 13.5 μmol per Ti-plate (1.766 cm^2 geometric surface area), followed by a final sintering at 450 °C for 1 h to finish the preparation process.

3.1.5 Combined sol-gel and solvothermal synthesis

$RuTiO_2$ sol solutions were prepared by the acetic acid-isopropanol route as described above. Titanium substrates were drop-coated with 50 µL coating solutions (0.1125 M) per single layer using a micropipetter, the process was repeated for 8 times with intermediate air-drying, and thermal stabilization at 200 °C (or 100 °C, 250 °C) for 10 min each time.

Figure 3.2 Images of autoclave pressure vessel and heating oven (left), Teflon liner (middle), and the schematic diagram (right) for solvothermal processing of electrode coatings.

A 250 mL teflon sealed stainless-steel autoclave (Figure 3.2 left, middle) was used for solvothermal processing of the above obtained amorphous coatings. The coated Ti-plates were put into a glass vial and located into the 30 mL diluted sol solutions (or 30 mL isopropanol) filled autoclave (Figure 3.2 right). The Ti-plate was isolated with the filled sol solutions by the glass vial. The autoclave was heated to 150 °C with a heating rate of 10 °C/min, and held at 150 °C for 24 h, then furnace cooled down to room temperature. The solvothermally processed coating was taken out and post-sintered at 450 °C for 1h under static air conditions.

3.2 Structural characterization of electrocatalysts

3.2.1 X-ray diffraction (XRD)

The phase structure of the prepared coatings was identified using a Siemens D500 diffractometer (Cu $K\alpha_{1,2}$ radiation, $\lambda_{K\alpha1}$ = 1.5406 Å, $\lambda_{K\alpha2}$ = 1.5444 Å) operated at 35 kV and 26 mA over a 2θ range of 20-60 ^{o} with a scanning step of 0.02^{o} / 4s. The crystal structures of the solvothermally processed coatings were refined using the analytical software TOPAS 2.1 based on the Rietveld methods to obtain the corresponding phase weight percentage, lattice parameters (*a*, *c*) and crystallite size with the kind help of Prof. Dr. Klaus Stöwe (Technical Chemistry, Universität des Saarlandes). Degussa P-25 TiO_2 powder was used as standard for the instrumental calibration [77].

High temperature X-ray diffraction (HT-XRD) was conducted on a Siemens D-5000 diffractometer with Cu $K\alpha$ radiation operated at 40 kV and 30 mA to characterize the phase evolution with temperature of the gel powders from room temperature to 600 ^{o}C with a 20 ^{o}C interval and a 30 ^{o}C min^{-1} heating rate at a 2θ range of 22~44^{o}.

3.2.2 Raman spectroscopy

The purpose for the measurements of the Raman spectrum is to obtain the lattice vibration information of a crystal [78]. A HORIBA-Jobin-Yvon LabRAM ARAMIS Raman spectrometer using a 632.8 nm excitation (He-Ne laser, 10 mW) was employed to record the Raman spectra and a silicon single-crystal was used for instrument calibration. The laser light was focused onto the sample using a 100 × objective lens.

3.2.3 Scanning electron microscopy and energy dispersive analysis (SEM-EDS)

The microstructure and elemental distribution were analyzed by scanning electron microscopy (SEM) and energy dispersive spectrometer (EDS) using JOEL JSM-7000F operated with an accelerating voltage 20 kV.

3.2.4 Transmission electron microscopy and electron diffraction (TEM-ED)

The transmission electron microscopy (TEM) and selected area electron diffraction (SAED) were carried out using a JEOL JEM-2010 microscope operated at 200 kV.

3.3 Electrochemical characterization

The electrochemical measurements of electrode coatings were carried out using a home-made medium-throughput multi-cell. The schematic diagram of the three-electrode configuration of a single cell is shown in Figure 3.3. The photographs of the electrochemical test cell are shown in Figure 3.4. The raw data were acquired by EC-Lab® software for further analysis.

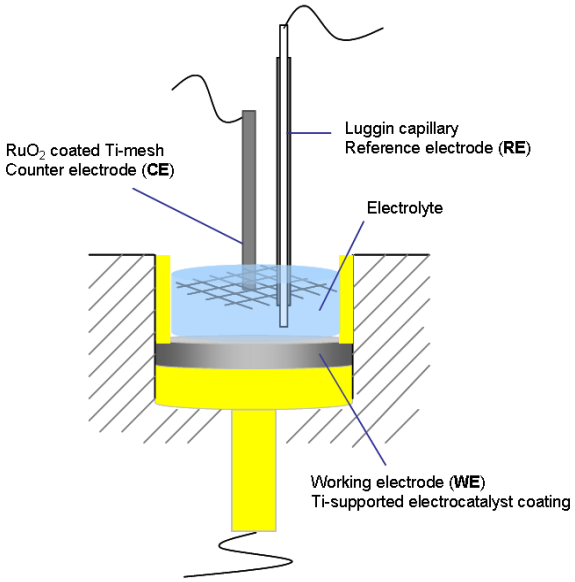

Figure 3.3. Schematic diagram of the three-electrode configuration cell for the electrochemical performance measurements of electrocatalyst coatings. Ti plates (15 mm in diameter) supported sol-gel coatings were used as working electrode with an exposed geometrical area of 1 cm^{-2}, RuO_2 coated titanium mesh (prepared by using sol-gel coating solutions) as counter electrode and Ag/AgCl/KCl(saturated) as reference electrode. The reference electrode was carefully positioned close to the working electrode by using a Luggin capillary to minimize the uncompensated electrolyte resistance.

The working electrode and the counter electrode are connected to a DC power supplier through an ampemeter. The potential of the working electrode is measured with respect to a reference electrode. The potential difference between the working electrode and the reference electrode consists of the potential of the working electrode and ohmic drop (*iR*) from the electrolyte between the reference and working electrode. The *iR*-correction can be done by using electrochemical impedance spectroscopy measurement or using current interruption technique.

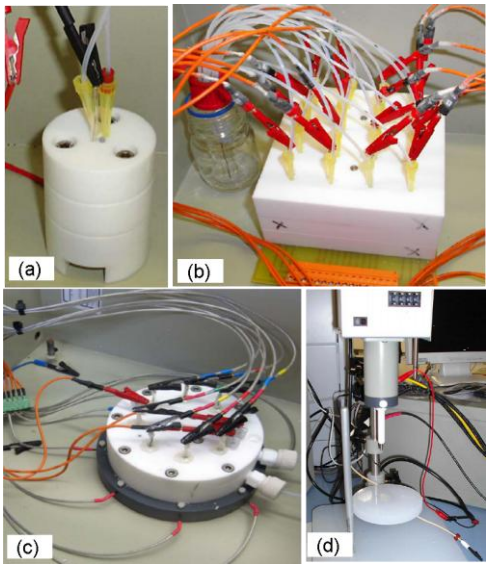

Figure 3.4. Electrochemical test cells (a) single cell, (b) 16-cell array, (c) 8-cell array with forced convection of electrolyte; and (d) Electrochemical impedance instrument.

Electrochemical performance measurements (CV, CP, galvanostatic polarization, and EIS) were performed in 3.5 M NaCl, pH 3 at room temperature unless otherwise noted. EIS measurement of rotating disk electrode facing downwards (2000 rpm, exposed area 1.77 cm^2) was carried out using in a galvanostatic mode (i = 100 mA). The frequency range was from 1 kHz to 1 Hz. The raw data acquired by EC-Lab® was exported into ZSimpWin for impedance data analysis. Then the data were fitted using appropriate equivalent circuit by ZSimpWin analysis software.

4 Results and discussion

The results obtained in this work are presented in this chapter. Four sections are included: the optimization in chemical composition of mixed $RuTiMO_x$ oxide electrocatalysts prepared by sol-gel route in Section 4.1; the preparation of the oxide coatings with controlled morphologies, such as the crack-free coatings, porous coatings and the electrochemical property characterization in Section 4.2; the modification in the phase structure of the mixed RuO_2-TiO_2 oxide coatings by solvothermal processing of the xerogel coatings in Section 4.3; and the analysis of gas bubble behaviour of electrolytic chlorine evolution at the gas-evolving electrodes in Section 4.4.

4.1 Chemical compositions of the electrocatalysts

4.1.1 Influence of preparation parameters

Prior to the deposition of oxide coatings onto the titanium substrates, the substrates were pre-treated by sand blasting and chemical etching to clean and roughen the surface. The surface topography of the Ti-substrates (15 mm in diameter) after the pre-treatment (sand blasting and chemical etching) was studied by Atomic Force Microscopy (AFM) (Surface Imaging Systems, SIS GmbH), as shown in Figure 4.1. The clean and rough surface (mean roughness: 1.37 μm) is desirable for good adhesion between the substrate and oxide coating.

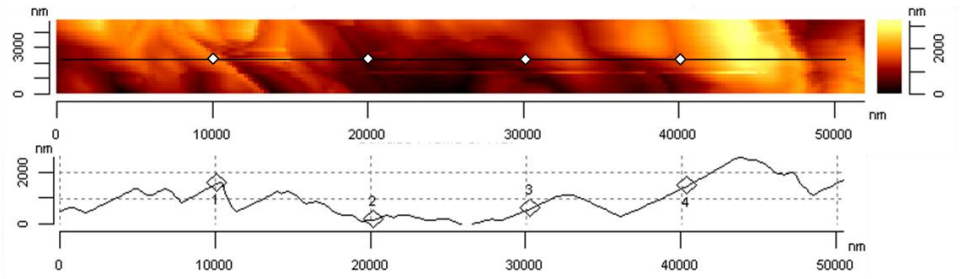

Figure 4.1. Surface topography analysis of titanium metal substrate after pre-treatment by sand blasting and chemical etching. Top: AFM image; Bottom: cross section analysis. Statistical data of the region of interest: Maximal height difference: 3.232 μm; Mean roughness: 1.373 μm; Root mean square: 0.6371 μm.

4.1.1.1 Oxide loading amount and coating thickness

Oxide loading amount is one of the important parameters related to the coating service life. As shown in Figure 4.2, the electrode potential of the $Ru_{0.25}Ti_{0.75}O_2$ coatings exhibits a linear decrease with the oxide loading amounts at the range of 3.5~12.5 g m^{-2} due to the effective utilization of the active sites depends on the penetration depth of the electrolytes into the inner parts of the mud-crack oxide coatings. It has been reported that the active surface area (corresponding to the voltammetric charges measured by cyclic voltammetry method) increases with coating thickness until it reaches to a plateau value [79]. The further increase in the thickness of the oxide coating can only prolong its service life. Another important factor concerning the available active surface area is the coating surface morphologies (mud-crack layer, porous layer, crack-free compact layer, etc.), which will be discussed in Section 4.2.

The commercially available anodes for chlorine evolution reactions consist of the standard composition of $Ru_{0.3}Ti_{0.7}O_2$ deposited onto titanium substrates [11,28] and with an oxide loading amount about 20~30 g m^{-2} [29]. For comparison purposes, in this work the oxide coatings were prepared by sol-gel method with the constant metal molar amounts of 4.5×10^{-5} mol per Ti-substrate plate (diameter 15 mm) and a fixed number of oxide layers (8-layer films). Accordingly, the mass of the oxide coatings could vary with the chemical composition and the molar ratio of the components. (For instance, for a coating with $Ru_{0.3}Ti_{0.7}O_2$, the oxide loading amount is 24.4 g m^{-2}.) Therefore, the decrease in noble

metal percentage means a decrease in the absolute quantity of the noble metal in the resulting coatings.

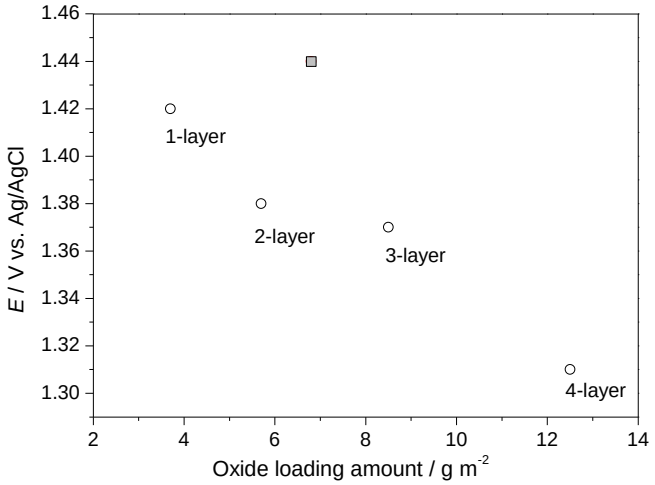

Figure 4.2. Dependence of performance on the oxide loading amounts of $Ru_{0.25}Ti_{0.75}O_2$ coatings. Electrode potential measured under galvanostatic mode at a current density of 100 mA cm^{-2} in 3.5M NaCl, pH 3, room temperature. The number of the oxide layers is marked out corresponding to the oxide loading amount. Square dot indicates crack-free coating prepared by dipping-withdrawing method (see Section 3.1.3).

4.1.1.2 Influence of sintering conditions on the crystallization, phase transition of powders

Thermal sintering is a necessary preparation step to obtain the mechanical and electrochemical stability of the ceramic oxide coatings. The crystallinity degree, crystallite size, voltammetric charge etc. depend on the sintering conditions, such as the sintering temperature and sintering time [33,80]. Increase in the sintering temperature could increase the degree of crystallinity, enhance the coating stability, and on the other hand promote the crystal growth, reduce the active surface area, induce the growth of insulating TiO_x interlayer due to the oxidization of underlying substrate under higher temperatures (> 500 ^oC) and O_2-containing ambience.

Although the powders behave differently from the coatings in the phase transition behaviour and their properties [81], some helpful information for optimizing the

preparation parameters for coatings can be obtained by using powders as research objects. Thermogravimetry and differential scanning calorimetry (TG-DSC) (Figure 4.3a), and high temperature X-ray diffraction (HT-XRD) (Figure 4.4) were performed to investigate the decomposition of residual organics and the amorphous-to-crystalline transition process of xerogel powders during sintering.

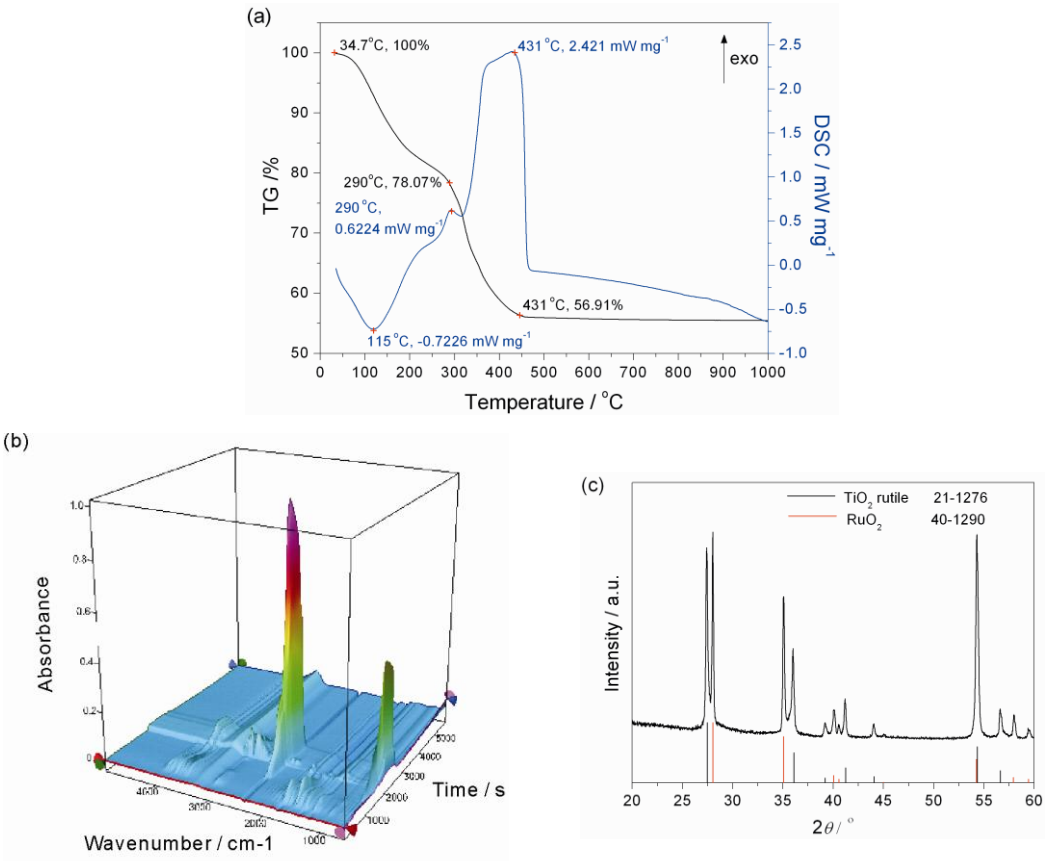

Figure 4.3. (a) TG-DSC data for air-dried $Ru_{0.25}Ti_{0.75}O_2$ xerogel powders (prepared by using acetic acid as catalyst for the hydrolysis and condensation reactions) recorded by elevating the temperature from 35 °C to 1000 °C with a ramping rate of 10 °C min^{-1} under mixed N_2 (5 ml min^{-1}) + air (15 ml min^{-1}) flow. (b) The coupled FTIR spectra are recorded continuously as a function of temperature (Time index was shown in place of temperature) for the evolved products analysis. (c) Metastable rutile solid solution $Ru_{0.25}Ti_{0.75}O_2$ powders decomposed into two separate RuO_2 and TiO_2 phases after TG-DSC measurements.

The TG curve exhibits mass loss characteristics of the gel powders (Figure 4.3a). A weight loss of 43% from room temperature to 450 ^{o}C and a slight weight loss of 0.7% from 450 ^{o}C to 1000 ^{o}C were observed. The wide endothermic peak around 115 ^{o}C associated with the first weight loss between 90~180 ^{o}C can be assigned to the elimination of adsorbed moisture and residual organic solvent, which can be confirmed from the absorption band of hydroxyl stretch vibration, ν_{OH} at 3500~4000 cm^{-1} and –CH_3 at 1500 cm^{-1} (Figure 4.3b). The decomposition of carbonaceous compounds in the gel powders was confirmed by the appearance of CO_2 and CO as the decomposition products detected in the range 200~450 ^{o}C (Figure 4.3b). The two exothermal peaks are therefore evident from the residual organic combustion along with the amorphous-to-crystalline transformation, since crystallization starts at 260 ^{o}C from HT-XRD results (Figure 4.4). The wide exothermal peak from 320~470 ^{o}C implies that the decomposition of organics may occur progressively.

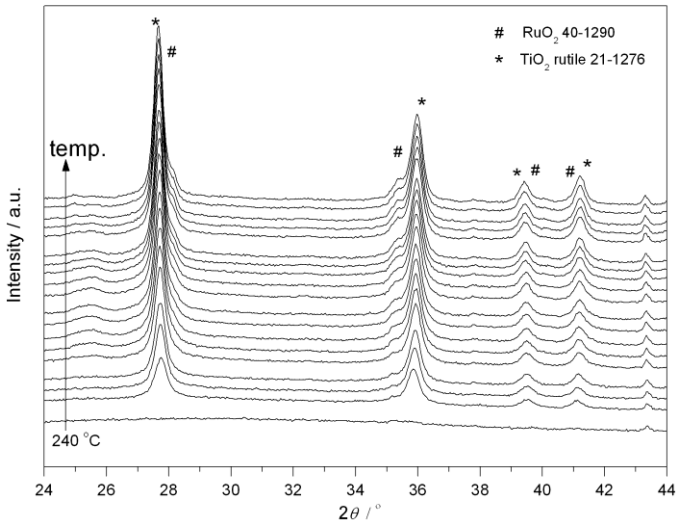

Figure 4.4. HT-XRD patterns of air-dried $Ru_{0.25}Ti_{0.75}O_2$ xerogel powders recorded on a Siemens D-5000 diffractometer from 240 ^{o}C to 600 ^{o}C with a 20 ^{o}C interval (diffraction patterns of powders with temperatures lower than 240 ^{o}C were amorphous and not shown here) and 30 ^{o}C min^{-1} heating rate at a 2θ range of 24~44^{o}.

As shown from HT-XRD (Figure 4.4), the crystallization of xerogel powders starts at 260 ^{o}C with the formation of rutile solid solution. From 260 ^{o}C to 600 ^{o}C, the single rutile solid solution phase was transferred into a mixed RuO_2 and rutile solid solution phases and

accompanied by the position shift of the (110) diffraction peaks of the solid solution phases toward the TiO_2 side. Furthermore, the rutile RuO_2-TiO_2 solid solution decomposed completely into separate RuO_2 and rutile TiO_2 phases for the powders after TG-DSC measurements (Figure 4.3c).

Table 4.1. Dependence of the properties of $Ru_{0.25}Ti_{0.75}O_2$ powders prepared by acetic acid-isopropanol route on the sintering temperature.

Sintering temperature / ^oC	S_{BET} / m^2 g^{-1}	Median pore radius / nm	Crystallite size* / nm
250	222.5	2.74	amorphous
450	55.2	3.24	23
600	12.6	7.97	> 25

* Calculated from the X-ray diffraction peaks using Scherrer's equation.

Table 4.1 summarizes the surface area, median pore radius measured by the BET gas adsorption technique and the crystallite size as a function of the sintering temperature for the $Ru_{0.25}Ti_{0.75}O_2$ powders. The BET specific surface area decreases with increasing sintering temperature due to the grain coarsening as usual. In contrast, the pore size showed a slight increasing trend with the sintering temperature. The increase in the pore size from 250 ^oC to 450 ^oC is possibly due to the continuous combustion of organic impurities. Further increase in the pore size from 450 ^oC to 600 ^oC is likely due to the decomposition of the metastable rutile solid solution phase into separated phases, which results in the interpenetration of neighbouring pores.

Note that the specific surface area of powder samples obtained from BET results is the geometric surface area. For the electrocatalysts used as coating form in the electrolyte environment, only the electroactive surface area should be taken into account. It has been observed that there is no simple linear relationship between the voltammetric charge density for coatings against the BET surface area for powders [82,83].

4.1.1.3 Influence of sintering conditions on the phase transition, surface morphology and electrochemical properties of coatings

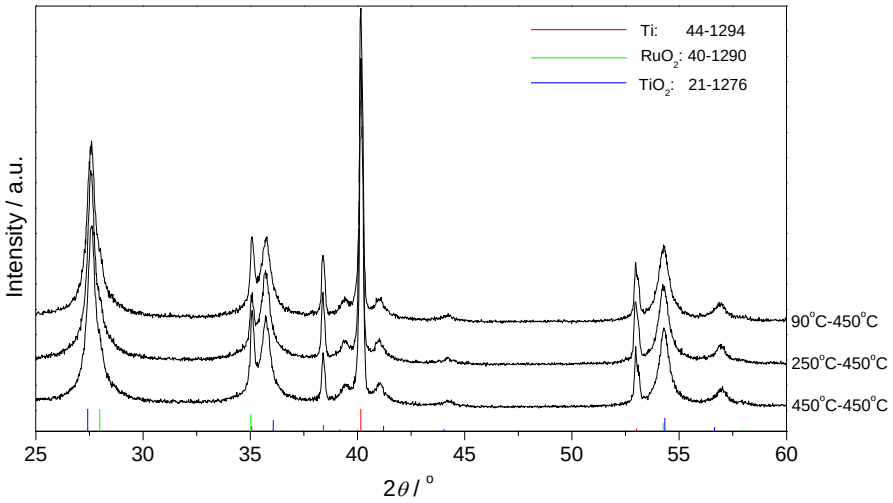

Figure 4.5. XRD patterns of $Ru_{0.4}Ti_{0.6}O_2$ coatings prepared by two-step sintering (1st at 90, 250, and 450 °C for 10 min, then 2nd at 450 °C for 10 min) of air-dried coatings.

For the preparation of oxide coatings, repetitious coating/sintering were employed in order to obtain the desired oxide loading amount, and a two-step sintering process was generally used to remove the solvent at the 1st step under relative lower temperature, and then stabilize and crystallize the oxide coating at the 2nd step under higher temperature. The influence of the sintering temperature in the 1st and 2nd steps on the XRD patterns of $Ru_{0.4}Ti_{0.6}O_2$ coatings is shown in Figure 4.5 and Figure 4.6. Although there are no obvious differences of the final phase structures in Figure 4.5, the relatively mild sintering conditions (250 °C, 10 min) were used as the 1st sintering treatment in the following sections, except where otherwise noted. By keeping the same conditions in the 1st sintering steps, the amorphous-like structure was observed when the temperature of the 2nd sintering was lower than 250 °C, whereas the decomposition of the metastable rutile RuO_2-TiO_2 solid solution was confirmed by the presence of RuO_2 (110) shoulder when the 2nd sintering temperature is 550 °C (Figure 4.6).

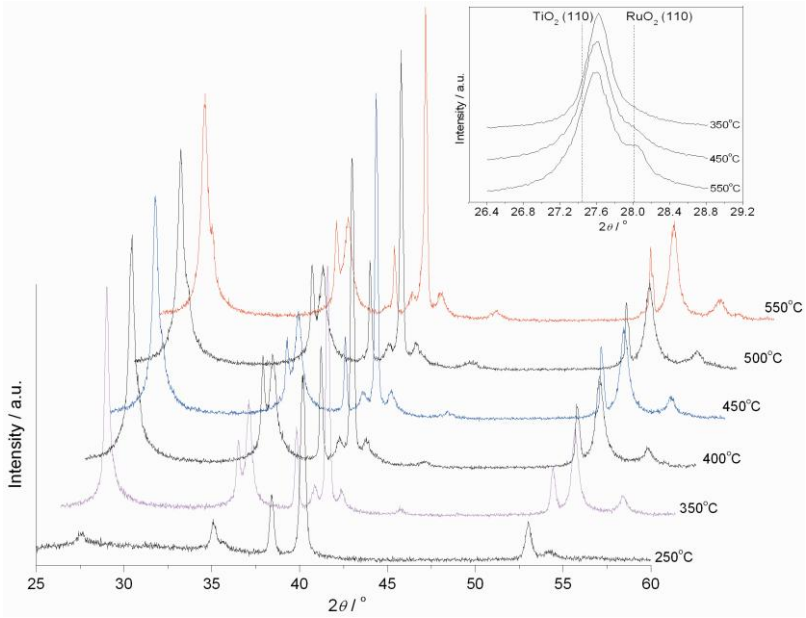

Figure 4.6. XRD patterns of $Ru_{0.4}Ti_{0.6}O_2$ coatings prepared by two-step sintering (1st at 250 °C for 10 min, then 2nd at 250, 350, 400, 450, 500, 550 °C for 10 min) of air-dried coatings. Inset: Local enlarged rutile (110) peaks of $Ru_{0.4}Ti_{0.6}O_2$ coatings corresponding to coatings with the 2nd sintering temperatures of 350, 450, 550 °C.

Sintering treatment of the titanium substrate supported oxide coating leads to a build-up of the in-plane tensile stress in the oxide layer. The mud-crack structure is formed to release the thermal mismatch stress between the substrate and the oxide layer when the magnitude of this tension is high enough [84]. The cracks also promote the subsequent sintering. Figure 4.7 shows the typical mud-crack surface morphologies of sol-gel coatings sintered at different temperatures. There is no obvious difference in the size of the cleavage block (*island*) with the increase in sintering temperature, but the islands turn up at higher temperatures due to the further shrinkage and densification. The formed gaps between the islands are favourable for the free access of electrolytes into the inner catalytic active sites. Meanwhile, this encourages the passivation of the underlying substrate during the long-term employment due to the direct chemical and electrochemical attack on the substrate by electrolyte. The design and control in coating morphologies in order to protect the underlying substrate will be discussed in Section 4.2.

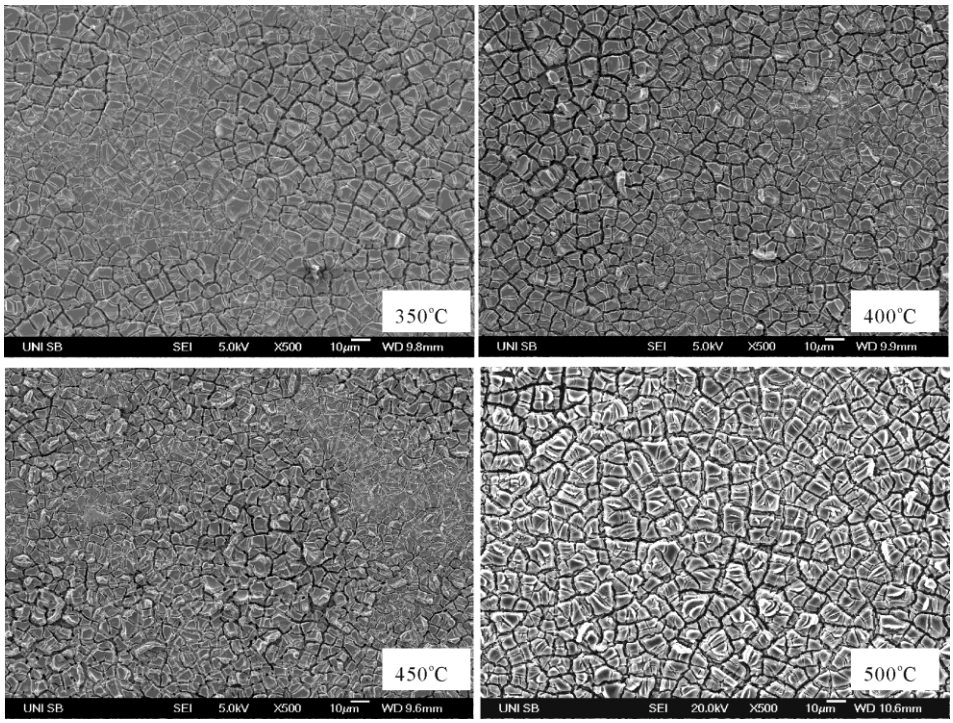

Figure 4.7. SEM images of surface morphologies of $Ru_{0.4}Ti_{0.6}O_2$ coatings sintered at different temperature (1st step sintering at 250 °C for 10 min). Scale bar: 10 μm.

The sintering conditions have significant influence on the final electrochemical performance of oxide coatings. As shown in Figure 4.8, with the increase of sintering temperatures from 350 °C to 500 °C, the voltammetric charges (i.e. the electrochemically active surface area of oxide electrode), evaluated by integrating the anodic branches of the cyclic voltammograms, decrease from 47 mC cm^{-2} to 12 mC cm^{-2}. Accordingly, the electrode potential for the chlorine evolution reactions increases by about 120 mV with the increase of the sintering temperature from 350 °C to 500 °C (Figure 4.8).

RuO_2-based electrode coatings contain the partial hydrated $RuO_x(OH)_y$, which accounts for the pseudo-capacitive properties. For the CV curves recorded in the potential sweep window without Faradaic chlorine evolution reactions, the solid-state surface redox transition of active species is represented by the pseudo-capacitive protonation/deprotonation [85,86]:

$$RuO_x(OH)_y + \delta H^+ + \delta e^- \rightleftharpoons RuO_{x-\delta}(OH)_{y+\delta},\ 0 \le \delta \le 2 \qquad (4.1)$$

The continuous change of δ during the proton exchange process occurs over a window of about 1.2 V [87]. Indeed, the amorphous-like $RuO_2 \cdot nH_2O$ is the target structure employed as electrochemical supercapacitors [88,89]. The capability of the proton exchange of the RuO_2-based electrode coatings with the solution could be alleviated by thermal sintering, which dehydrates the hydrated ruthenium species, and is responsible for the decrease in the voltammetric charge density with the increase of sintering temperature.

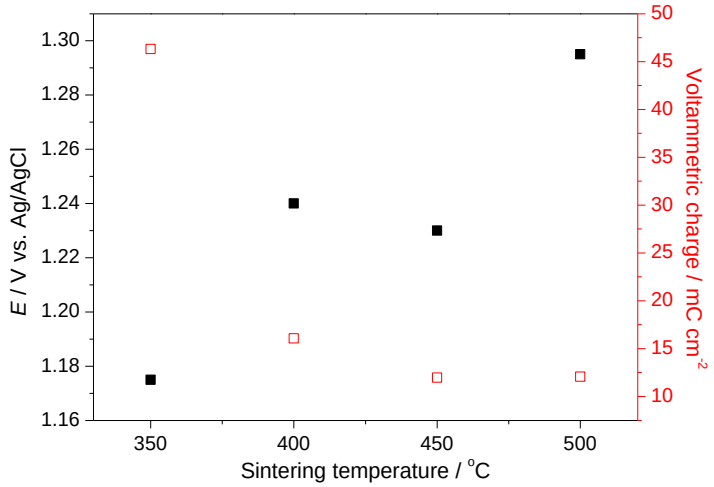

Figure 4.8. Dependence of voltammetric charges density (□) and electrode potential (■) (measured at a current density of 100 mA cm^{-2} in 3.5M NaCl, pH3, room temperature) on the sintering temperature of $Ru_{0.4}Ti_{0.6}O_2$ coating corresponding to Figure 4.6.

4.1.2 Chemical composition of electrocatalysts

Mixed oxides using the electrocatalytically active component RuO_2 (Table 2.2) and/or IrO_2 combined with inert oxide(s) TiO_2, SnO_2, V_2O_5, ZrO_2, CeO_2 etc. represent the most widely studied electrocatalyst materials in the attempt to enhance the catalytic activity, to modify the microstructure, to reduce the material costs [90,91,92,93]. The noble metal oxides provide the active sites and conductive paths, whereas inert oxides are used to dilute and stabilize the active component.

Thin coatings of RuO_2-based oxide can be deposited onto heat resistant substrates by the thermal decomposition of corresponding metal salts. The metal salts are usually dissolved into suitable solvents and the substrates are wetted with the coating solutions by various techniques such as brushing, spraying. After drying, the substrate supported wet coatings are sintered in air at high temperature to decompose the salts and to burn the carbonaceous residues to get the final oxide or mixed oxide. This process can be only applicable for the metal substrate which does not oxidize at the required temperature. Since the beginning temperature for the titanium oxidation is about 500 ^{o}C, the incomplete decomposition of ruthenium precursor salts is one of the main problems encountered in the preparation process. Heterogeneity in microstructure is another intrinsic drawback of the oxide coatings prepared by the conventional thermal decomposition technique [33] and it could limit the ability to develop new electrocatalysts by optimized combination of multicomponent composite oxides. The inhomogenous elemental distribution could be due to (i) the different solubilities of the precursor salts during the drying process, (ii) some nuclei of single oxide are formed before the firing step, (iii) the differences of the salts oxidation rate [94]. Thus multi phase components with local enrichment of one phase is the main feature of thermal decomposition derived oxide coatings.

In the aspect of the microstructural homogeneity of composite oxides, the low-temperature sol-gel route prefers the formation of homogenously distributed oxo bridges between metal centres (M-O-M') by the hydrolysis and condensation reactions of molecular precursors. High crystallinity of oxides at lower sintering temperatures with less phase impurities of the sol-gel derived materials have demonstrated higher activity and stability in comparison with those prepared by thermal decomposition route [29,48,95]. However, few studies have been devoted to evaluate the multi-doping effects of sol-gel derived composite oxide electrocatalysts so far with respect to nanoscale structural homogeneity (Table 2.3).

4.1.2.1 Doping effect of mixed oxides

Although IrO_2 is less active than RuO_2 for chlorine evolution reaction (Figure 4.13), the partial replacement of RuO_2 by IrO_2 was done in order to reduce the material cost (considering the fluctuations in the market price). In addition, iridium has the ability to

enhance the durability of the RuO_2-TiO_2 oxide coatings [46,96]. IrO_2 has the same rutile tetragonal structure as RuO_2 and TiO_2. XRD patterns show that the diffraction peaks become broader with the increase in Ir content in the $Ru_{0.4-x}Ir_xTi_{0.6}O_2$ mixed oxide (Figure 4.9), indicating the decrease in crystallite size (Figure 4.12). As a consequence, the voltammetric charge density increases with the doping of Ir into binary $RuTiO_2$ system (Figure 4.12).

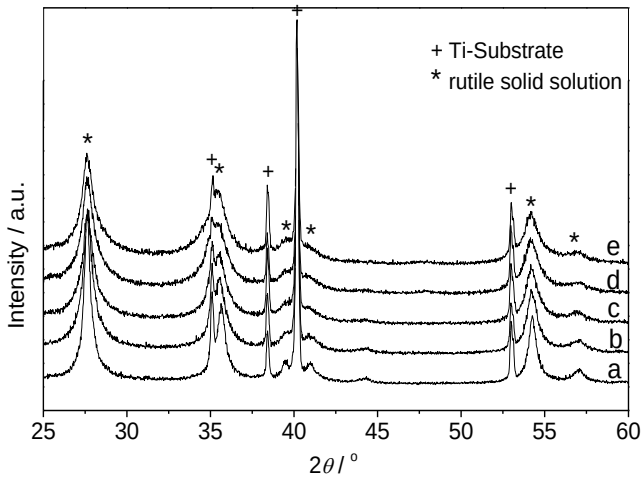

Figure 4.9. XRD patterns of $Ru_{0.4-x}Ir_xTi_{0.6}O_2$ coatings prepared by acetic acid-isopropanol route. ($IrCl_3$ was used as precursor salt and with the addition of HNO_3 to dissolve the $IrCl_3$, other preparation details are described in the experimental section.) (a) x = 0, (b) x = 0.1, (c) x = 0.2, (d) x = 0.3, (e) x = 0.4.

Table 4.2. Structural data for some metal oxides with rutile structure [97].

	TiO_2	RuO_2	IrO_2	SnO_2	CrO_2	NbO_2	VO_2
Metal ionic radii / nm	0.068	0.067	0.068	0.071	0.062	0.074	0.063
Lattice parameters, c/a	0.6441	0.6905	0.7011	0.6726	0.6596	0.6255	0.6260
Cell volume / $Å^3$	62.43	62.78	64.13	71.51	57.03	71.20	59.15

Compared to the reported XRD phase analysis results for the industrial IrO_2-RuO_2-TiO_2/Ti electrode with a molar ratio of Ir:Ru = 1:1 [96], the relative intensity of the rutile (110) diffraction peaks at $2\theta = 27.62^o$ is weaker for the present electrode using the diffraction

peaks from Ti-substrate as reference. The stronger and narrower X-ray diffraction peaks from the industrial electrode could arise from the larger crystallite size rather than the thicker oxide layer.

SnO_2 has been used as dopants added into $RuTiO_2$ system to replace TiO_2. The substitution of Ti by Sn in the $Ru_{0.4}Sn_xTi_{0.6-x}O_2$ mixed oxide results in the obvious shift of the rutile diffraction peaks towards the SnO_2 side and the broadening of diffraction peaks (Figure 4.10). The rutile structure has edge-sharing octahedrally coordinated metal ions which form chains along the [001] direction [97]. The M-O bond distances are not equal for the MO_6 octahedra with different metal ion centers. Thus, with the existence of the dopant ions in the host lattice, the lattice structural distortion could be caused by the difference in the metal ionic radii (Table 4.2), M-O bond distances. In contrast, for the $RuIrTiO_2$ system, due to the similarity in the metal ions radii and unit cell volume of the dioxide, there is no position shift observed in the diffraction peaks (Figure 4.9).

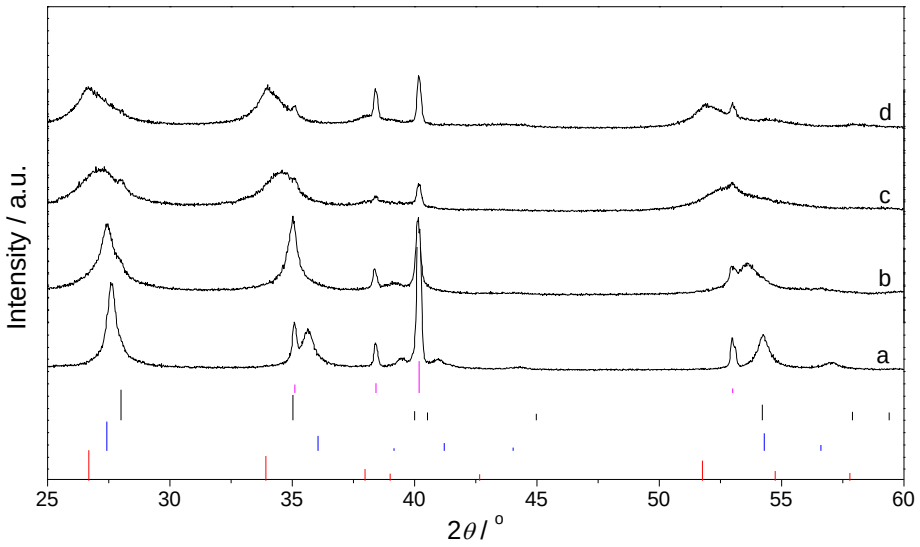

Figure 4.10. XRD patterns of $Ru_{0.4}Sn_xTi_{0.6-x}O_2$ coatings prepared by acetic acid-isopropanol route. (a) x = 0, (b) x = 0.2, (c) x = 0.4, (d) x = 0.6. The position of the diffraction peaks from the JCPDS database of Ti-substrate (44-1294), RuO_2 (40-1290), TiO_2 (21-1276), SnO_2 (41-1445).

A single phase of rutile structure was formed for the $Ru_{0.4}Sn_{0.4}Ti_{0.2}O_2$ ternary oxide with a crystallite size of about 5 nm (Figure 4.12). The growth of crystal has been inhibited in the multicomponent system. The voltammetric charge density increases four times compared to the one of the binary $Ru_{0.4}Ti_{0.6}O_2$ oxide. Since the voltammetric charge density represents the amount of protons exchanged between the oxide coating and the aqueous electrolyte, and the SnO_2 does not show any notable redox behaviour in the CV potential sweep range [98], therefore the surface redox equilibria (Eq. (4.1)) are dominated by the ruthenium species both for the binary $Ru_{0.4}Ti_{0.6}O_2$ coatings and ternary $Ru_{0.4}Sn_{0.4}Ti_{0.2}O_2$ coatings. The electrode potential for chlorine evolution reduces to about 1.16 V for the $Ru_{0.4}Sn_{0.4}Ti_{0.2}O_2$ coatings, i.e., a reduction of 90 mV compared to the $Ru_{0.4}Ti_{0.6}O_2$ coatings (Figure 4.13). The improvement in the electrocatalytic activity for oxygen evolution reactions by the substitution of Ti by Sn in the $Ru_{0.3}Sn_xTi_{0.7-x}O_2$ has also been reported [99].

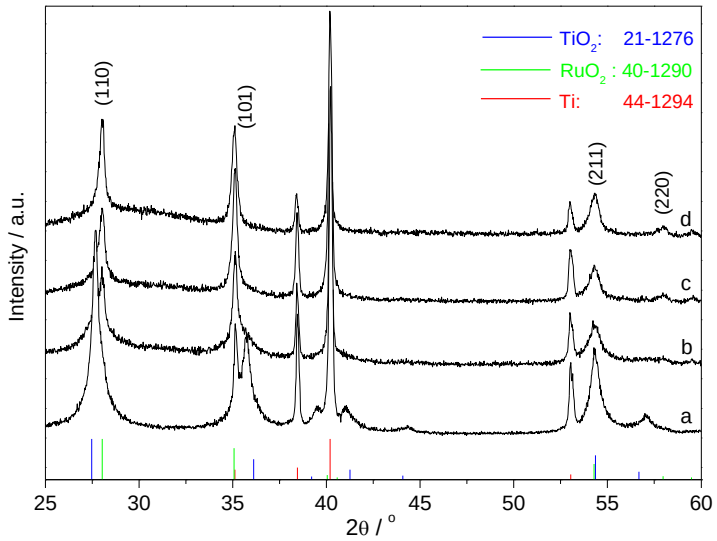

Figure 4.11. XRD patterns of $Ru_{0.4}Ti_{0.6-x}La_xO_2$ coatings prepared by acetic acid-isopropanol route. (a) x = 0, (b) x = 0.05, (c) x = 0.10, (d) x = 0.15.

The doping of lanthanum into $RuTiO_2$ system is different from the homogeneous doping of Ir, Sn. The La_2O_3 has hexagonal crystal structure and the ionic radius of La^{3+} is 0.1016 nm [100], which is very large in comparison with Ti^{4+} and Ru^{4+} (Table 4.2). Due to the heterogeneous doping, the substitution of La^{3+} for Ti^{4+} could affect the lattice symmetry significantly.

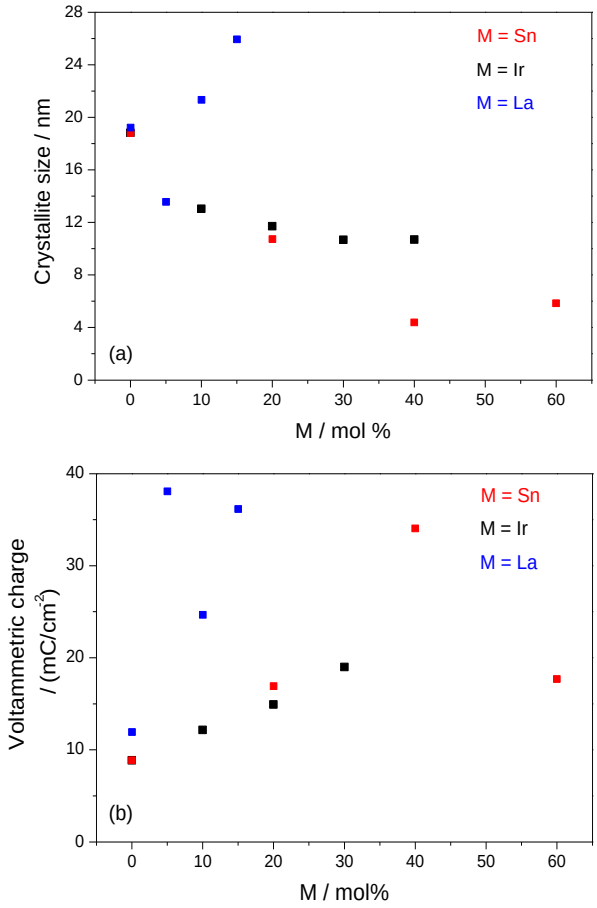

Figure 4.12. (a) Dependence of the crystallite size (calculated by using Scherrer's equation) on the coating composition $Ru_{0.4}Sn_xTi_{0.6-x}O_2$, $Ru_{0.4}La_xTi_{0.6-x}O_2$, $Ru_{0.4-x}Ir_xTi_{0.6}O_2$. (b) Dependence of the voltammetric charge density on the coating composition $Ru_{0.4}Sn_xTi_{0.6-x}O_2$, $Ru_{0.4}La_xTi_{0.6-x}O_2$, $Ru_{0.4-x}Ir_xTi_{0.6}O_2$. Potential sweep rate: 50 mV s^{-1}.

With the doping of lanthanum, the (110), (101), (220) diffraction peaks shift towards RuO_2 side (Figure 4.11). No separate phase was observed for the coatings containing different amount of lanthanum dopants. The lanthanum dopant does not have a significant influence on the crystallite size (Figure 4.12). Interestingly, the voltammetric charge density increases evidently for the lanthanum-containing coatings, although the crystallite size is larger than in the iridium- or tin-containing coatings (Figure 4.12). This is due to the leaching characters of lanthanum oxide in the acidified solution, which creates accessible pores in the oxide matrix and accordingly provides higher active surface area. The apparent electrocatalytic activity was enhanced by the geometric effect (Figure 4.13).

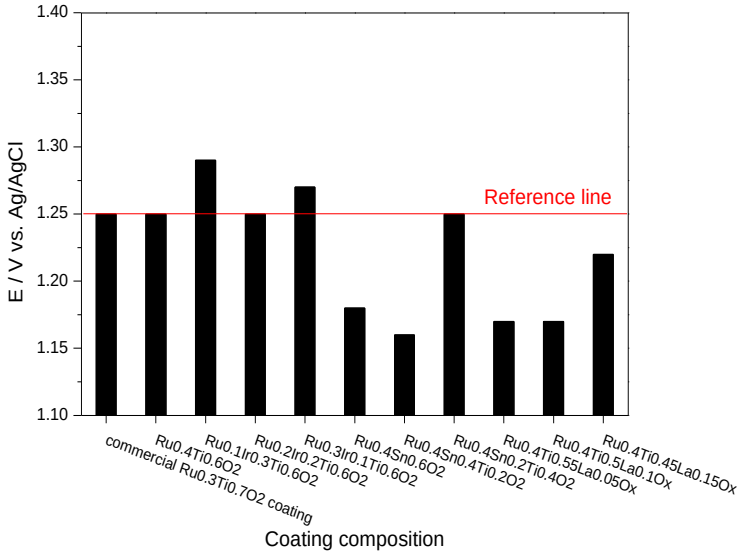

Figure 4.13. Electrode potential measured by chronopotentiometry in 3.5 M NaCl, pH 3, at j = 100 mA cm^{-2}, at room temperature for different coatings. The measurement error of potential is about 20 mV. The red reference line is the electrode potential value of the commercial $Ru_{0.3}Ti_{0.7}O_2$/Ti electrode measured under the same conditions.

Although the $RuTiMO_x$ coatings with M = Sn, La shows improved electrocatalytic performance (Figure 4.13), the high content of ruthenium in the mixed oxide could reduce the oxygen/chlorine electrode potential difference [21], since the selectivity for the oxygen/chlorine evolution reactions depends on the chemical composition of oxide coatings [101]. Therefore, the addition of suitable dopants into the $RuTiO_2$ system to reduce the ruthenium molar content is not only technically necessary but also economically important.

Figure 4.14 compares the electrocatalytic performance of some ternary oxide $RuTiMO_x$ coatings with M = V, Zr, Cr, Mo prepared by the propionic acid-isopropanol route. The molar percentage of ruthenium is 25% or 15%, which is below that of the commercial electrode (30%). $Ru_{0.25}Ti_{0.7}V_{0.05}O_x$ coatings show the best performance with an electrode potential of about 1.17 V. Unlike the oxides of Sn, Zr, Cr, Mo, the vanadium oxides such as V_2O_5, VO_2 exhibit electrochemical activity, which has been widely investigated as electrochemical supercapacitors [88,102,103]. The mechanisms for the enhancement of the electrochemical properties for chlorine evolution reactions with vanadium-containing mixed oxide coatings are worth to be investigated further.

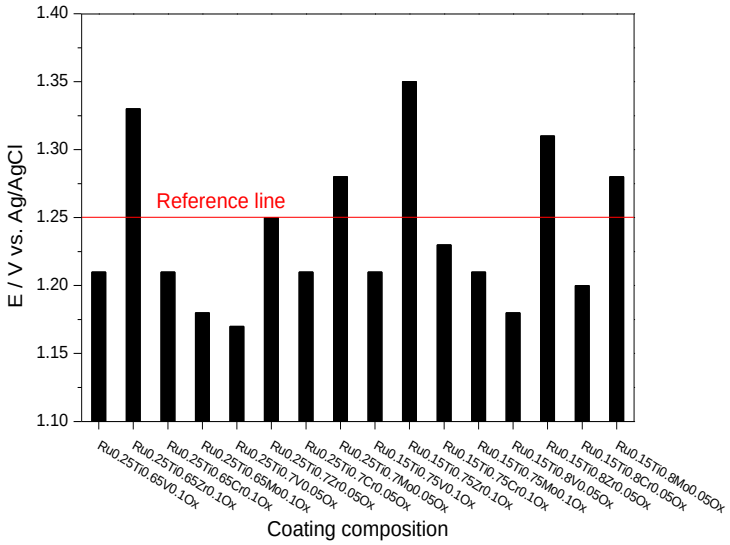

Figure 4.14. Electrode potential measured by chronopotentiometry in 3.5 M NaCl, pH 3, at j = 100 mA cm^{-2}, at room temperature for different coatings. The measurement error of the potential is about 20 mV. The red reference line is the electrode potential value of the commercial $Ru_{0.3}Ti_{0.7}O_2$/Ti electrode measured under the same conditions.

4.1.2.2 Microhomogeneous mixed oxide prepared by propionic acid-isopropanol route

On the basis of the above obtained results that the ternary $RuTiMO_x$ electrocatalysts with M = Sn, V exhibit improved electrocatalytic activity compared to the binary RuO_2-TiO_2 oxide, further optimization of the electrocatalytic properties by using pentanary composite oxides $Ru_{0.1}Ir_{0.1}V_{0.05}Sn_{0.4}Ti_{0.35}O_x$ with reduced noble metal content were investigated herein.

It is difficult experimentally to obtain stable sol solutions using the previous acetic acid-isopropanol route for the preparation of the pentanary oxide. Indeed, mixed phases with enrichment of individual component have been observed by other researchers by using the sol-gel route to prepare the mixed oxide $RuIrTiO_2$ [46], $RuTiO_2$ [104] due to the unsuitable recipe. The presence of amorphous structure due to the incomplete crystallization, metallic ruthenium due to the incomplete hydrolysis reactions and single anatase TiO_2 due to the competitive hydrolysis reactions are undesirable for application as electrocatalysts [104]. No special advantages could be achieved from the sol-gel route in comparison with the

conventional thermal decomposition route if the problems mentioned above can not be resolved effectively.

To obtain stable and homogenous initial sol solutions, carboxylic acid acting as solvent, acid catalysts and also chelating reagents have been reported to overcome some common difficulties encountered in the sol-gel synthesis of composite oxides, due to the difference in hydrolysis reactivity and dissolvability among various precursors [105,106,107,108]. Once the metal alkoxides or acetylacetonates dissolve separately in the hot mixed propionic acid and isopropanol solvents, the ligand exchange reaction occurs [109]. Various metal cations are chelated due to the carboxylation and the formation of metal propionates. The propionate end groups act as steric hindrance to keep the dispersion of the metal ions. Thus the differences in reactivity against hydrolysis of the various precursors could be harmonized. After various metal precursors were dissolved and stabilized into propionic acid and isopropanol mixture, they were mixed to allow the further hydrolysis and condensation reactions to build up the M-O-M' network.

The pentanary oxide was prepared herein by propionic acid-isopropanol route to investigate the microstructural homogeneity of the composite oxide materials. For comparison, $Ru_{0.4}Ti_{0.6}O_2$ and $Ru_{0.25}Ti_{0.7}V_{0.05}O_x$ coatings were prepared in the same way and characterized under identical conditions.

Figure 4.15 shows the phase structures of the composite oxide coatings deposited onto titanium substrates for the binary $Ru_{0.4}Ti_{0.6}O_2$ and pentanary $Ru_{0.1}Ir_{0.1}V_{0.05}Sn_{0.4}Ti_{0.35}O_x$. Single phase rutile-type solid solutions were formed in both cases. The inhibition effect of crystal growth is more distinct in the pentanary oxide compared to the binary oxide observed from the weaker and broader diffraction peaks of rutile configuration. The crystallite size was estimated from the rutile (110) peaks by using Scherrer's equation. The calculated results were 4 nm and 16 nm for the pentanary composite and binary composite, respectively. Due to the multi-doping in the composite oxides, different metal ions coordination and high structural distortion effects could be responsible for the inhibition of crystal growth against the thermal sintering. The decrease in the crystal dimension down to a few nanometres could increase the coordinatively unsaturated sites of active component and therefore the catalytic reactivity [110].

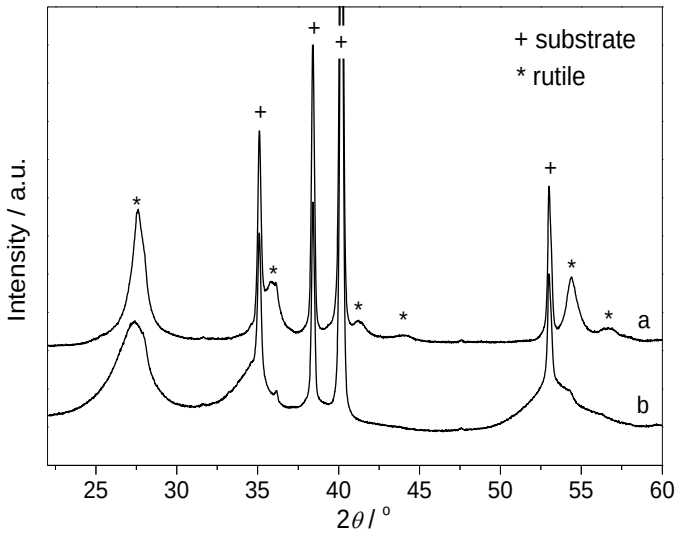

Figure 4.15. X-ray diffraction patterns of the electrode coatings prepared by the propionic acid sol-gel route: (a) $Ru_{0.4}Ti_{0.6}O_2$, (b) $Ru_{0.1}Ir_{0.1}V_{0.05}Sn_{0.4}Ti_{0.35}O_x$.

The microstructural homogeneity of the $Ru_{0.1}Ir_{0.1}V_{0.05}Sn_{0.4}Ti_{0.35}O_x$ coatings was investigated by SEM-EDS. The EDS elemental mapping results for the pentanary oxide are shown in Figure 4.16. Due to the long acquisition time (20 min), the inevitable specimen drift is monitored by comparing the SEM images before and after the acquisition, as shown in Figure 4.16a-b. Several agglomerates observed from the SEM images on the coating surface were selected as reference points. Irrespective of the drift of the specimen towards left-down during the acquisition, there is no indication of individual element enrichment observed from the EDS mapping images at the positions corresponding to the several agglomerates attached on the coating surface. Uniform elemental distributions in the whole ranges were observed from the EDS maps, thus one may suspect that there are no discrepancies in the chemical composition between the agglomerates and the flat coating surfaces, and the multi-components of Ru, Ir, V and Sn are micro-homogenously dispersed throughout the oxide matrix.

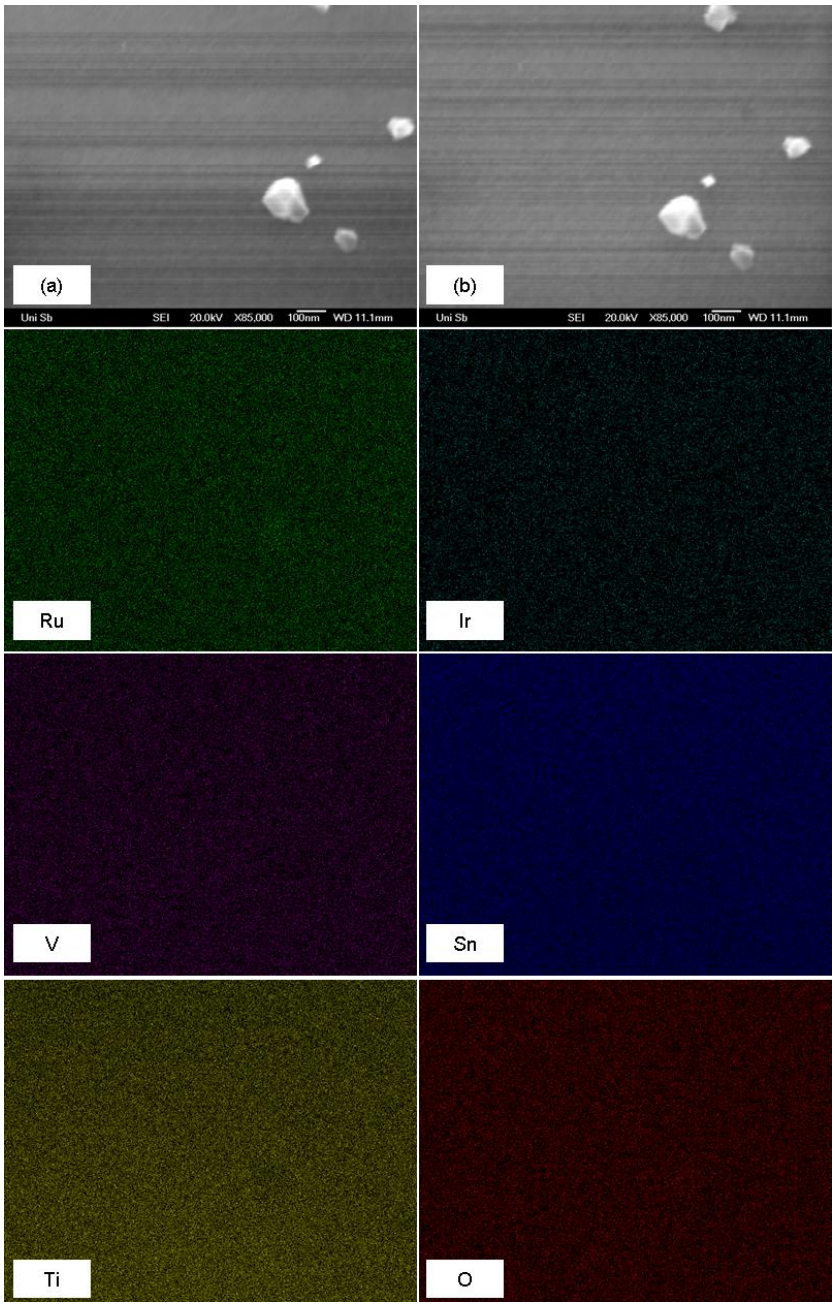

Figure 4.16. SEM images before (a) and after (b) EDS mapping showing the slight specimen drift during the 20min acquisition time, and the corresponding EDS elemental mapping images of $Ru_{0.1}Ir_{0.1}V_{0.05}Sn_{0.4}Ti_{0.35}O_x$ oxide coatings. Magnification: ×85000.

The quantitative elemental composition analysis of the pentanary oxide obtained from the SEM-EDS (Figure 4.17) shows the molar ratio of Ru, Ir, V, Sn, which is close to the nominal composition. The content of Ti identified is higher than the nominal value owing to the electrons' penetration through the oxide layers for the EDS analysis. The electron-

specimen interaction volume contains then parts from the underlying titanium substrate with the applied acceleration voltage.

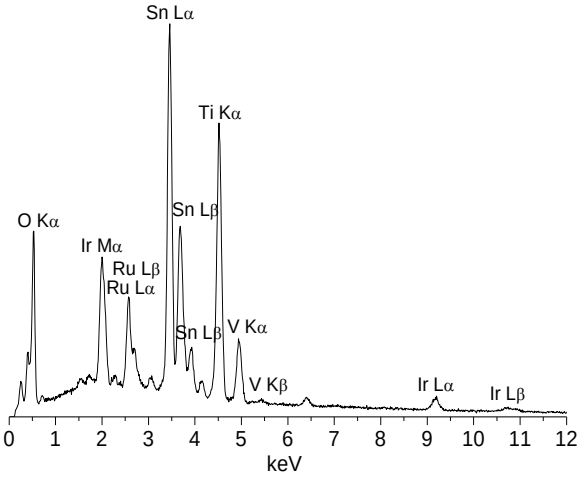

Figure 4.17. Energy dispersive X-ray spectroscopy (EDS, the X-ray intensity vs. X-ray energy) of the $Ru_{0.1}Ir_{0.1}V_{0.05}Sn_{0.4}Ti_{0.35}O_x$ coating. The sample areas for EDS analysis corresponds to the SEM image Figure 4.16a. The elemental compositions identified quantitatively were (at %): 2.29 Ru, 2.06 Ir, 1.24 V, 11.27 Sn, 13.00 Ti, 70.14 O.

Electrochemical cyclic voltammetry analysis for the obtained pentanary oxide is shown in Figure 4.18. The voltammetric charge density calculated by the integration of the anodic branch was 15.5 mC cm^{-2} for the $Ru_{0.1}Ir_{0.1}V_{0.05}Sn_{0.4}Ti_{0.35}O_x$ coatings, which is about fourfold larger than the one for $Ru_{0.4}Ti_{0.6}O_2$ coatings. It is well known that the voltammetric charge density is a measure of the amount of the accessible electroactive sites of the electrode surface. The dopants of Ir, Sn contribute to the decrease in the crystallite size as confirmed in the previous section. The addition of V is in order to increase the electrocatalytic activity for chlorine evolution. The Ru is partially substituted by Ir with the intent of reducing the material costs and enhancing the stability of the electrocatalysts [46].

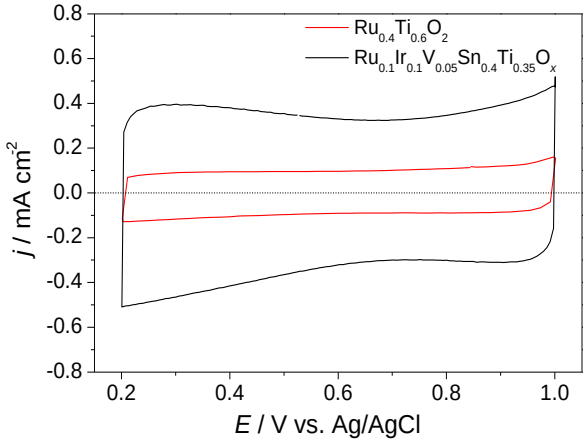

Figure 4.18. Cyclic voltammograms of the $Ru_{0.4}Ti_{0.6}O_2$ coating and the $Ru_{0.1}Ir_{0.1}V_{0.05}Sn_{0.4}Ti_{0.35}O_x$ coating. The cyclic voltammetry was measured in 3.5 M NaCl, pH 3, room temperature, Ag/AgCl as reference electrode. The potential was scanned from 0.2 to 1.0 V with a potential sweep rate υ = 20 mV s^{-1}. Exposed electrode surface areas: 1 cm^2.

The galvanostatic polarization measurements for the $Ru_{0.1}Ir_{0.1}V_{0.05}Sn_{0.4}Ti_{0.35}O_x$ coatings and $Ru_{0.4}Ti_{0.6}O_2$ coatings are shown in Figure 4.19. For the current density steps from 0.5 to 100 mA cm^{-2}, i.e., from the slight to the intensive chlorine evolution region, the electrode potential response was recorded. Lower electrode potentials for chlorine evolution were observed for the $Ru_{0.1}Ir_{0.1}V_{0.05}Sn_{0.4}Ti_{0.35}O_x$ coatings than for the $Ru_{0.4}Ti_{0.6}O_2$ coatings and the difference is larger at higher current densities. The electrode potential difference is about 80 mV at the current density of 100 mA cm^{-2}. Compared to the commercial $Ru_{0.3}Ti_{0.7}O_2$ coatings (Figure 4.13), a decrease of electrode potential of about 30mV is achieved for the $Ru_{0.1}Ir_{0.1}V_{0.05}Sn_{0.4}Ti_{0.35}O_x$ coatings measured under the same conditions. However, the $Ru_{0.4}Ti_{0.6}O_2$ coatings show worse performance than the commercial $Ru_{0.3}Ti_{0.7}O_2$ coatings. The geometric effect could contribute to the higher activity for the commercial coatings in this case, due to the possible porous structure of the inner oxide layer [11,96].

The electrode potential value is stable at lower current densities, but increases continuously at higher current densities during the chlorine evolution reaction. The reasons for the linear drift of the electrode potential are not known. The polarization curves, plotted by taking the middle value for the drift potential signal versus log j (Figure 4.20), are characterized by

two Tafel slopes for both electrodes, indicating the kinetic and mass transfer controlled reaction mechanisms.

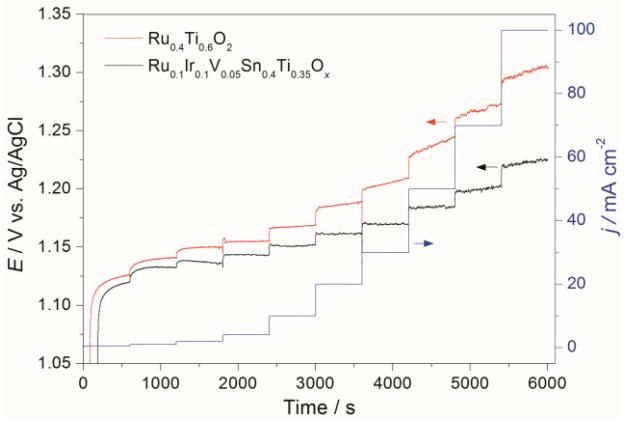

Figure 4.19. Galvanostatic polarization profiles of $Ru_{0.4}Ti_{0.6}O_2$ and $Ru_{0.1}Ir_{0.1}V_{0.05}Sn_{0.4}Ti_{0.35}O_x$ coatings measured in 3.5 M NaCl, pH 3, 50 °C, Ag/AgCl as reference electrode. The applied current densities were j / (mA cm^{-2}) = 0.5, 1, 2, 4, 10, 20, 30, 50, 70, 100. Exposed electrode surface areas: 1 cm^2.

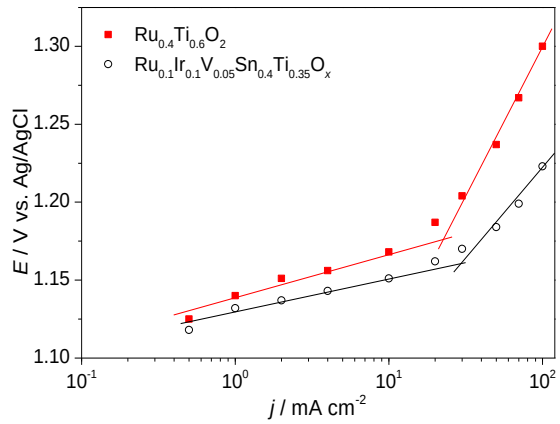

Figure 4.20. The E-log j curves obtained from Figure 4.19 without the iR-correction.

The electrochemical impedance analysis allows separating various factors, such as ohmic resistance of electrolyte, oxide film, and interface response of the electrocatalytic coating exposed to the electrolyte. Figure 4.21 shows the impedance spectra of the composite oxide coatings. The semicircles corresponding to charge transfer for chlorine evolution reactions were observed in the Nyquist plots (Figure 4.21a). The double logarithmic plots

of $-Z''$ vs. f (Figure 4.21b) show clearly that one relaxation time exists [111]. Using a proposed equivalent circuit $R_e(Q_{dl}R_{ct})(Q_fR_f)$ [112], where R_e is the electrolyte ohmic resistance, R_{ct} and R_f are the charge transfer resistance and oxide film resistance, respectively, while Q_{dl} and Q_f are constant phase elements related to the capacitance of the charge transfer process and oxide film, respectively. The fitted parameters are summarized in Table 4.3.

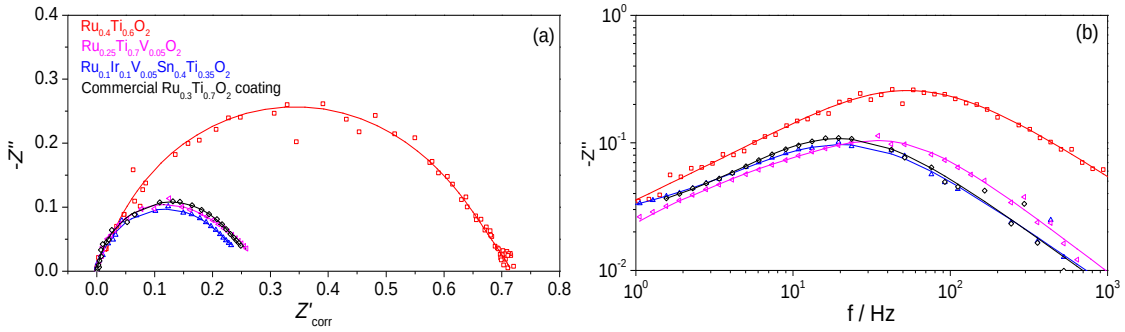

Figure 4.21. Impedance diagram for the sol-gel-derived $Ru_{0.4}Ti_{0.6}O_2$, $Ru_{0.25}Ti_{0.7}V_{0.05}O_x$, $Ru_{0.1}Ir_{0.1}V_{0.05}Sn_{0.4}Ti_{0.35}O_x$ coatings and commercial coating with the nominal composition $Ru_{0.3}Ti_{0.7}O_2$ measured in 3.5 M NaCl, pH 3 at room temperature, using in a galvanostatic mode (applied current, i = 100 mA). Exposed surface area: 1.77 cm^{-2}. (a) Nyquist plots, for better clarity, the real parts were corrected by removing the electrolyte ohmic resistance. (b) The double logarithmic plots of $-Z''$ vs. f. Solid lines represent the fitted results using equivalent circuit $R_e(Q_{dl}R_{ct})(Q_fR_f)$.

It was found that the oxide film resistance of the composite oxide ceramic coatings was so small (~ 0.075 Ω) even for the coating containing 10% Ru and 10% Ir, which are different from the reported critical concentration of 25~30% Ru or Ir to keep metallic conductivity of oxide matrix [113]. This behaviour can be well explained by the microstructural homogeneity of the composite oxides. Unlike the thermal decomposition prepared materials, in which poorly doped composite oxides consist of individual domains of conductive noble metal oxide and inert and insulating valve metal oxide, the highly dispersed Ru and/or Ir in the composite oxides prepared by the propionic acid-isopropanol route assure the continuous conduction path.

Table 4.3. Parameters of the equivalent circuit ($R_e(Q_{dl}R_{ct})(Q_fR_f)$) used to describe the impedance behaviour of the composite oxide coatings.

	R_e (Ω)	Q_{dl}*		R_{ct} (Ω)	Q_f*		R_f (Ω)
		Y_0 ($\Omega^{-1}s^n$)	n #		Y_0 ($\Omega^{-1}s^n$)	n	
$Ru_{0.4}Ti_{0.6}O_2$	0.6624	0.01133	0.84	0.6677	2.11	0.99	0.03158
$Ru_{0.25}Ti_{0.7}V_{0.05}O_x$	0.2746	0.03087	0.93	0.1994	0.8138	0.79	0.07984
$Ru_{0.1}Ir_{0.1}V_{0.05}Sn_{0.4}Ti_{0.35}O_x$	0.2359	0.06159	0.88	0.2174	5.712	0.60	0.07528
Commercial coating	0.2196	0.05100	0.90	0.2484	5.307	0.98	0.02885

* A constant phase element (Q) instead of capacitance (C) is used to describe a practical electrode with different degrees of surface roughness or a nonuniform distribution of surface active sites. n is a number between 0 and 1 (n = 1 for a pure capacitance). It means that the capacitor element has characteristics intermediate between a capacitor and a resistor.

The reciprocal of the charge transfer resistance, $1/R_{ct}$, reflects the electrocatalytic activity of the oxide coatings for the chlorine evolution reactions [112]. Based on the fitted parameters, the activity of the coatings follows the sequence: $Ru_{0.25}Ti_{0.7}V_{0.05}O_x$ > $Ru_{0.1}Ir_{0.1}V_{0.05}Sn_{0.4}Ti_{0.35}O_x$ > commercial coating > $Ru_{0.4}Ti_{0.6}O_2$ (Table 4.3). This order is consistent with the electrode potential measured by chronopotentiometry.

Owing to the decrease in crystallite size, the pseudocapacitance of the pentanary oxide was twice that of the ternary oxide, which means the active surface areas increase twice, although the pentanary oxide contains less content of noble metal. The commercial $Ru_{0.3}Ti_{0.7}O_2$ coating has larger pseudocapacitance than the $Ru_{0.4}Ti_{0.6}O_2$ coating, which confirms the assumption that the porous inner oxide layer of the commercial coating contributes to the apparent electrocatalytic activity as geometric factor by increasing the accessible surface area.

4.1.3 Conclusion

In this section, the mixed oxide electrocatalyst $RuTiMO_x$ coatings were prepared by two different sol-gel routes to investigate the influence of chemical composition on the electrocatalytic activity for chlorine evolution reactions of the oxide coatings and their structure-property correlation.

An initial study of the influence of the coating preparation parameters on the coating performance has been carried out to establish experimentally the suitable oxide loading amount, sintering conditions. The acetic acid-isopropanol route is suitable for the preparation of binary $RuTiO_2$ system, whereas the propionic acid-isopropanol route possesses the advantage for the synthesis of mixed multicomponent $RuTiMO_x$ system, such as the ternary and pentanary oxide.

The substitution of Sn, V, Cr, La for the Ti in the $RuTiMO_x$ system increases the electrocatalytic activity effectively. The decrease in crystallite size and the corresponding increase in the voltammetric charge density can be realized by the doping of Ir, Sn into the $RuTiO_2$ system. Compared to the commercial $Ru_{0.3}Ti_{0.7}O_2$ coating, the simultaneous enhancement in the electrocatalytic activity and the reduction of noble metal content have been achieved by using the $Ru_{0.25}Ti_{0.7}V_{0.05}O_x$ or $Ru_{0.1}Ir_{0.1}V_{0.05}Sn_{0.4}Ti_{0.35}O_x$ coating.

The geometric factor could also play a critical role for the improvement of the apparent electrocatalytic activity. Porous structure of oxide layer is favourable for the practical applications. This has been deduced from the electrochemical properties of $RuTiLaO_x$ coating and commercial coating. The fabrication of pores with the intent of enhancing the apparent catalytic activity will be discussed in the next section.

4.2 Morphology-controlled preparation

This section presents two different ways to control the coating morphology, including the fabrication of crack-free coating as inner layer to protect the substrate against passivation, and the preparation of porous coating as outer layer to increase the electrode specific surface area.

Traditionally, the electrode coatings prepared by thermal decomposition of the corresponding inorganic salts exhibit a mud-crack surface morphology. Similarly, the typical surface morphologies of the sol-gel-derived oxide coatings are shown in Figure 4.22. The surface consists of islands with the size ca. 4 μm in length, boundary gaps ca. 1~3 μm in width, close-stacked particles with a diameter ca. 30 nm, inter-grain regions and pores. These *flaws* (such as cracks, cavities and gaps) facilitate the penetration of electrolytes and provide high accessible inner active surface areas, which are responsible for the electrocatalytic properties as a geometrical factor, in contrast to the intrinsic electrocatalytic activity related to the electrocatalyst materials (Section 4.1).

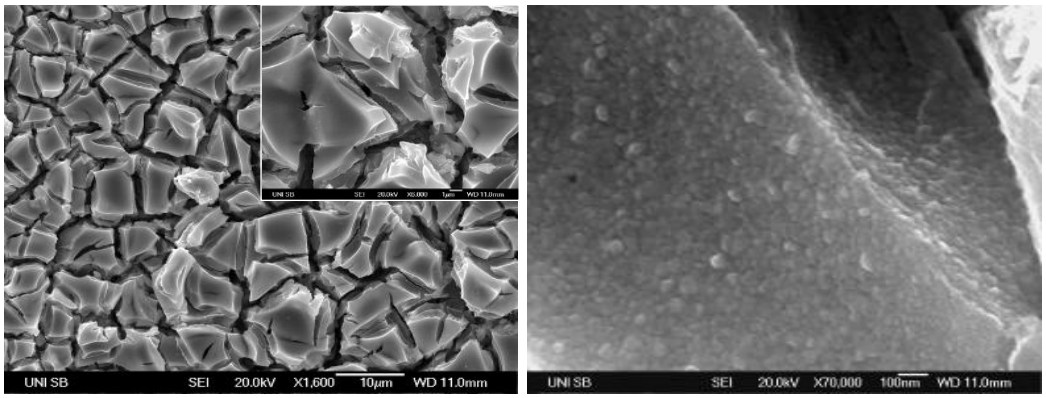

Figure 4.22. Representative SEM images of $Ru_{0.4}Ti_{0.6}O_2$ coating show the typical *mud-crack* characteristics of the sol-gel drop-coating prepared coatings. Scale bar: Left 10 μm; Inset in Left 1 μm; Right (enlarged image of the island): 100 nm.

4.2.1 Crack-free coatings

Controlled-preparation in surface morphologies, such as the number of pores, pore size, particle size, cracks are critical to the enhancement in the electrocatalytic performance. On the other hand, the penetration of electrolytes onto the underlying substrates through the cracks could accelerate the deactivation of electrode due to the growth of an insulating TiO_x interlayer between the substrate and the oxide layer, as described above. A protective and crack-free inner layer has been taken into account in this section.

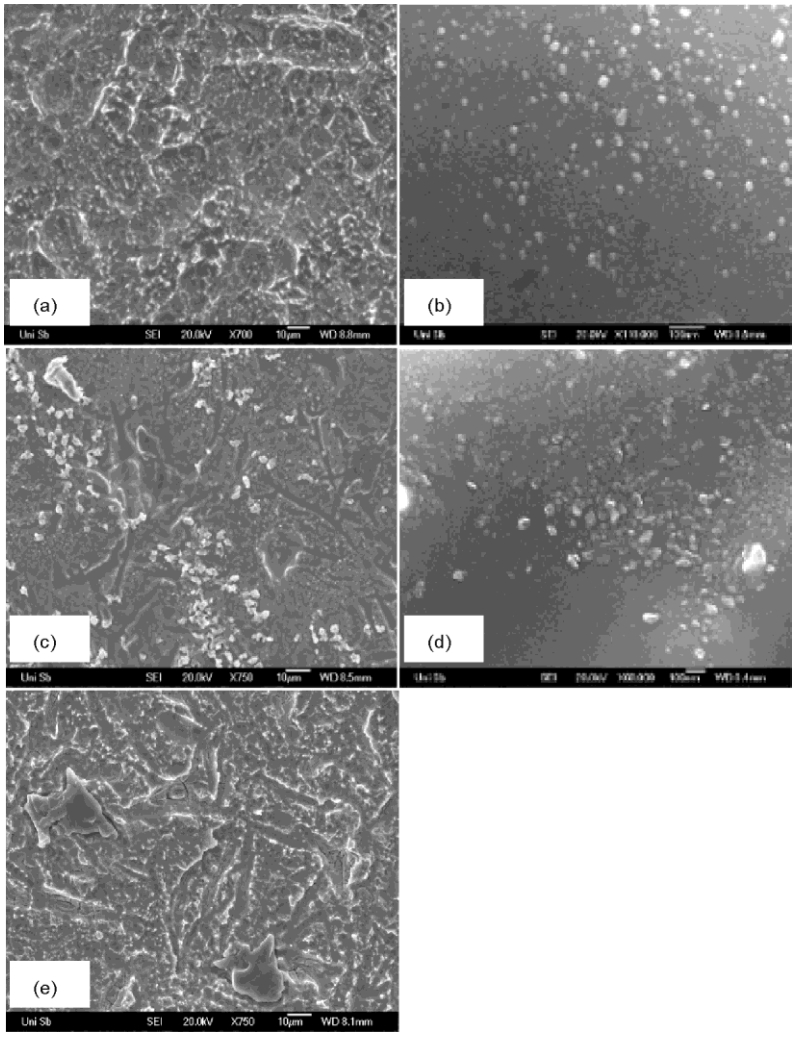

Figure 4.23. SEM images of crack-free $Ru_{0.25}Ti_{0.75}O_2$ coatings prepared by dip-coating method by (a, b) propionic acid-isopropanol route, (c, d) acetic acid-isopropanol route, 25 layers, with oxide loading of 4.2 g m^{-2} from 0.1125 M precursor solution; and (e) acetic acid-isopropanol route, 6 layers, with oxide loading of 3.7 g m^{-2} from 0.45 M precursor solution. Scale bar: (a, c, e) 10 μm, (b, d) 100 nm.

Herein a repetitive sol-gel dipping-withdrawing technique was performed to prepare crack-free coatings (see: Section 3.1.3). In this case, the tensile stress was relaxed right away through plastic deformation for each single thin layer after the heat-treatment without the formation of cracks. It is critical to control the single layer thickness (should be below a critical thickness, i.e. the maximal thickness without the formation of cracks) and thicker crack-free coatings have been obtained by increasing the repetitive times of dipping/drying/sintering. Acetic acid-isopropanol route and propionic acid-isopropanol route were used to prepare the sol solutions. As shown in Figure 4.23, in order to obtain the crack-free coatings with comparable oxide loading amount or thickness, more dipping-withdrawing/drying/sintering cycles are required if the concentration of coating solutions is lower. The coating solution and its concentration, and the substrate withdrawing rate are important factors to obtain crack-free coatings.

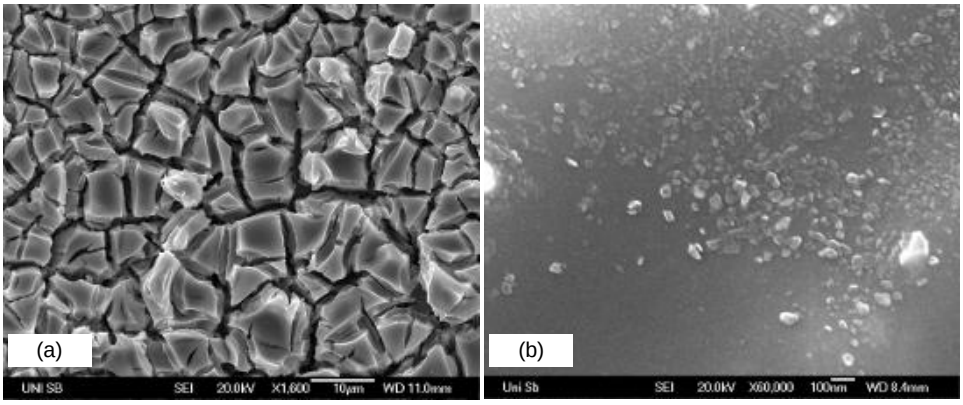

Figure 4.24. SEM images of surface morphologies of $Ru_{0.25}Ti_{0.75}O_2$ coatings (a) crack-mud coating prepared by drop-coating, (b) crack-free coating prepared by dipping-withdrawing method. Scale bar: (a) 10 μm, (b) 100 nm.

Except for the direct observation of the mud-crack or crack-free surface morphologies by SEM (Figure 4.24), electrochemical cyclic voltammetry provides in-situ characterization of the electrolyte penetration into the inner cracks and the electrochemical response of the surface (outer surface, islands, inner cracks, gaps) to the applied potential sweep (Figure 4.25). One of the prominent characteristics of the crack-free coating is the impermeability for electrolytes and accordingly the protective properties for the underlying titanium substrates.

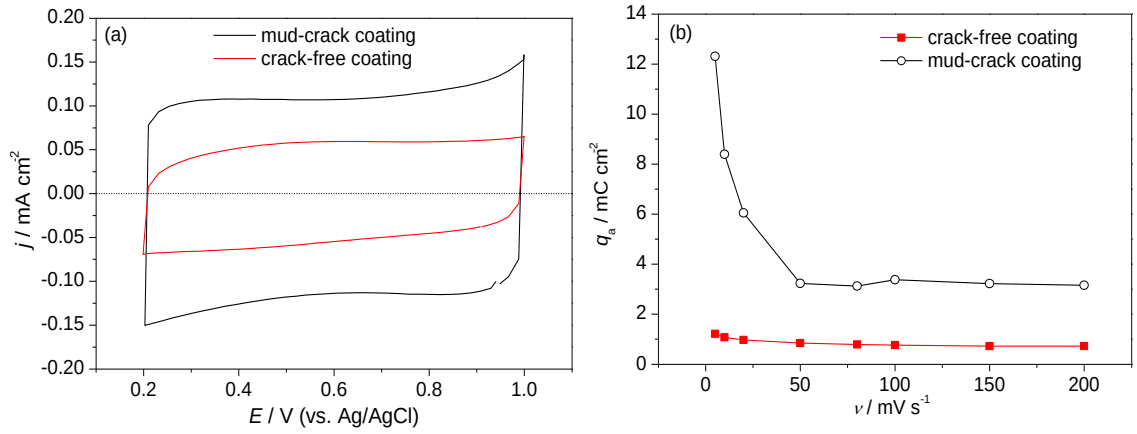

Figure 4.25. (a) CV curves of $Ru_{0.25}Ti_{0.75}O_2$ coating with different surface morphologies corresponding to Figure 4.24, recorded in 3.5M NaCl, pH 3, at room temperature, with a scan rate of 50mV s^{-1}. (b) Dependence of voltammetric charges (q_a) on the potential sweep rates (υ) for the coating with crack-free or typical mud-crack surface morphology.

The penetration behaviour of electrolyte through the oxide coatings (or the wetting of oxide coating by electrolytes) as a function of potential sweep rate was evaluated by plotting the voltammetric charges (q_a) against the potential sweep rates (υ), as shown in Figure 4.25. The voltammetric charges for the mud-crack coating show an initial sharp decrease with the potential sweep rate from 5~50mV s^{-1} and then keep constant when the potential sweep rate exceeds 50 mV s^{-1}. In contrast, the voltammetric charges for the crack-free coating are independent of the potential sweep rate.

This phenomenon can be explained from the relationship between the q_a with the electrochemically accessible surface of the oxide coated electrodes. At very high potential sweep rate, only the outermost oxide layer gives response to the fast potential sweep, whereas for the slower potential sweep, the electrochemical response from the much deeper inside layer contributes to the total voltammetric charges by the progressively penetration of electrolyte through the *flaws*. The crack-free coatings prepared in this work show the unique impermeable characteristics for the electrolyte of aqueous solution sodium chloride. This provides the possibility to protect the underlying titanium substrate from passivation due to the direct contact with electrolyte under the harsh chlorine evolution environment. Further investigation to evaluate the long-term service life of the oxide layer with the protective inner crack-free layer is necessary.

4.2.2 Porous oxide film coated electrodes

Porous electrodes are widely used in many technological applications, such as energy storage, capacitive deionization, water desalination, and fuel cell materials [114]. Porous structures are usually employed to facilitate the electrolyte penetration through the pore gaps and increase the material usage by creating highly available surface areas. Porous electrodes are expected to maximize the coating capacitance. Pore size and distribution are the critical factors related to the increase of the pseudo-capacitance of materials. A confinement of solvation ion in nano-channel has also been reported by Ohkubo et al.[115]. In the case if the pore size is smaller than the corresponding ion size, then there is no room to accommodate one ion per pore. The charge-storage mechanism in nanoporous materials has been developed [116]. Traditional double-layer model was used to describe the outer surface charging, and the double-cylinder model was applied to the inner pores. Other researchers proposed that the pore space within the electrode is filled with electrolyte, exchanging ions with a thin double-layer ‘‘*skin*’’ on the electron-conducting electrode matrix [114].

Nano-pores have been created by chemical leaching routes by mixing leachable elements (lanthanum for instance) into the oxide matrix ($RuTiLaO_x$). The electrode coating $RuTiLaO_x$ was prepared by multiple dropping-drying-sintering cycles. The increase in the number of pores by the subsequent leaching of lanthanum oxide will increase the electrochemically accessible surface areas. The in-situ electrochemical cyclic voltammetry was used to monitor the change of electrode surface area by the cyclic potential sweep in 0.5 M hydrochloric acid. Figure 4.26 shows the voltammetric charge density (q_a, obtained by means of the EC-Lab software by integrating the anodic branches of the cyclovoltammograms) of electrodes as a function of the voltammetric cycling times for $Ru_{0.4}Ti_{0.45}La_{0.15}O_x$ (dotted line) and $Ru_{0.4}Ti_{0.6}O_2$ (solid line). The q_a of the $Ru_{0.4}Ti_{0.6}O_2$ coating is independent of the voltammetric cycling times, indicating that there are no changes in the characteristics of the oxide electrode. However, a continuous increase in the q_a for the $Ru_{0.4}Ti_{0.45}La_{0.15}O_x$ coating was observed from the 2^{nd} potential cycle to the 79^{th} potential cycle. This is caused by the continuous leaching of lanthanum oxide away from

the oxide matrix during the voltammetric cycling and the simultaneous increase of the coating porosity. Open pores rather than closed pores are created by the chemical leaching route, which can be utilized fully in the aqueous solution system.

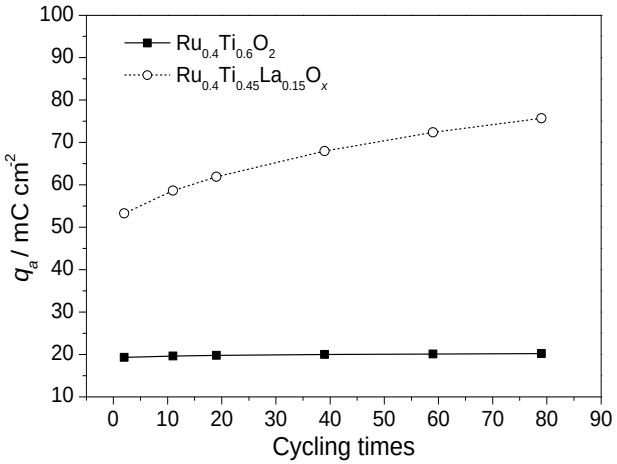

Figure 4.26. The voltammetric charge density (q_a) of electrodes as a function of the voltammetric cycling times for the $Ru_{0.4}Ti_{0.6}O_2$ coating (solid line) and $Ru_{0.4}Ti_{0.45}La_{0.15}O_x$ (dotted line). The cyclic voltammetry was measured in 0.5 M HCl, room temperature, Ag/AgCl as reference electrode. The potential was scanned from 0.2 to 1.0 V with a potential sweep rate υ = 50 mV s^{-1}. The exposed electrode areas is 1 cm^2.

4.2.2.1 Porous electrode coating $Ru_{0.3}Sn_{0.7}O_2$

In order to investigate systematically the electrochemical properties of porous electrode coatings, $Ru_{0.3}Sn_{0.7}O_2 \cdot x\ La_2O_3$ coatings (x = 0, 0.05, 0.1, 0.2) were deposited onto titanium substrates by propionic acid based sol-gel route. Porosity is obtained by chemical leaching of La_2O_3 with 1.63 M HCl (13.5 mL 37 wt% HCl were diluted to 100 mL with water) at 60 °C for 10 min with slight stirring after the deposition of each single layer. Coatings were obtained by 8 dropping-drying-sintering-leaching cycles and a final sintering at 450 °C for 1h.

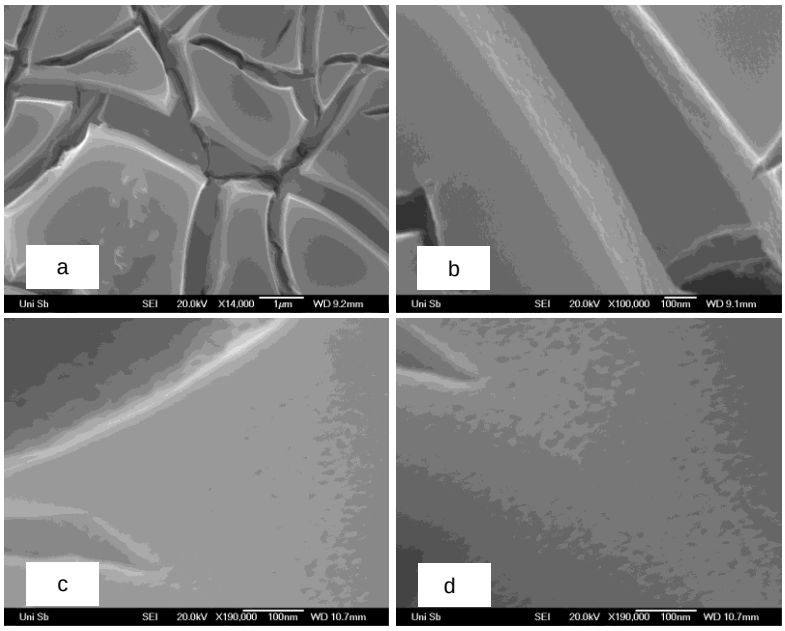

Figure 4.27. SEM images of (a, b) $Ru_{0.3}Sn_{0.7}O_2$ and (c, d) $Ru_{0.3}Sn_{0.7}O_2 \cdot 0.20\ La_2O_3$ after lanthanum oxide leaching prepared by propionic acid sol-gel method. Scale bar: (a) 1 µm, (b, c, d) 100 nm.

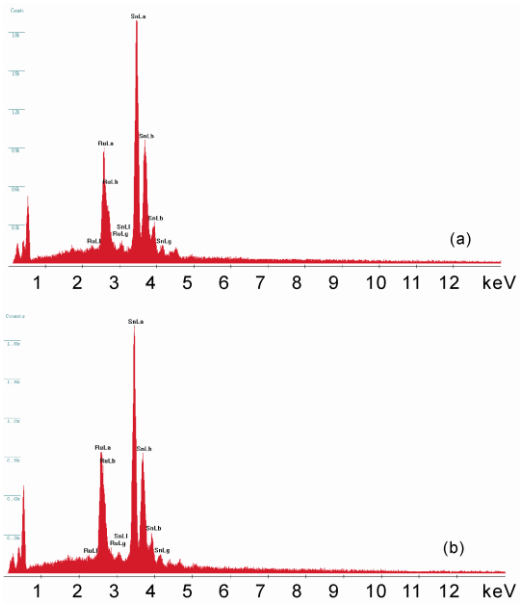

Figure 4.28. Energy-dispersive X-ray spectroscopy (EDS) of (a) $Ru_{0.3}Sn_{0.7}O_2$ / Ti and (b) $Ru_{0.3}Sn_{0.7}O_2 \cdot 0.20\ La_2O_3$ / Ti after lanthanum oxide leaching. The absence of lanthanum species (La $L_{\alpha 1}$ 4.651 keV, La $L_{\beta 1}$ 5.042 keV) inside the oxide layer was confirmed.

A comparative observation of the surface morphologies of the $Ru_{0.3}Sn_{0.7}O_2 \cdot x\,La_2O_3$ coatings (x = 0, 0.20) is shown in Figure 4.27. The film electrodes prepared by the dropping-sintering-leaching cycles possess typical mud-crack structures. The cracks provide a facilitated penetration path for the electrolyte for the electrode reactions.

Meanwhile, the split islands compose the entity of the electrocatalyst materials. Nanopores with a diameter around 15 nm (mesopores) were observed from the $Ru_{0.3}Sn_{0.7}O_2 \cdot 0.20\ La_2O_3$ coating after lanthanum oxide leaching. Energy-dispersive X-ray spectroscopy (EDS) in Figure 4.28 shows that there is no residual lanthanum left in the final oxide matrix.

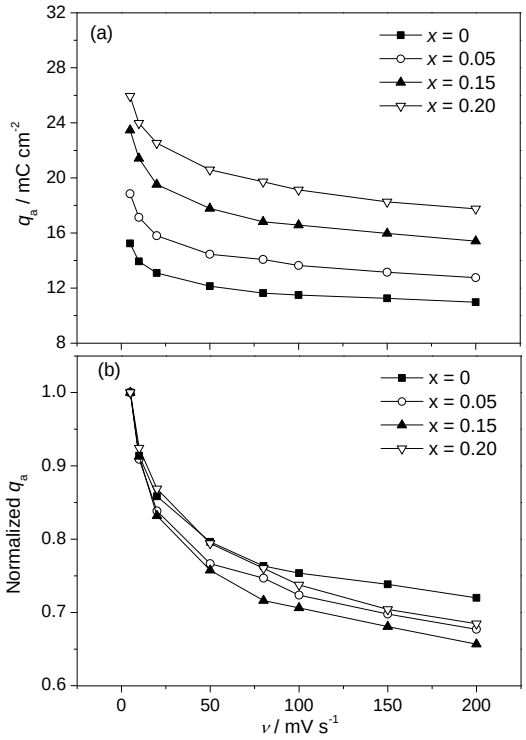

Figure 4.29. (a) Anodic charges as a function of potential scan rate as obtained by integration of the cyclic voltammograms for $Ru_{0.3}Sn_{0.7}O_2 \cdot xLa_2O_3$ film electrodes in 3.5 M NaCl, pH 3 at room temperature. (b) Normalized voltammetric charges as a function of potential scan rate obtained by dividing the voltammetric charges by the voltammetric charges measured at 5 mV s^{-1}.

The pores created by lanthanum oxide leaching increase the electrochemically accessible sites effectively as confirmed by the increase in voltammetric charge densities (q_a) in

Figure 4.29a. Accordingly, the inner active sites contribute more to the electrochemical response than the outer active sites for the porous electrodes, observed from the normalized voltammetric charges (Figure 4.29b).

A possible explanation for this phenomenon is that the embedded lanthanum clusters within the split islands were leached away after the leaching of the outwards exposed lanthanum clusters attached on the cracks and cavities, which results in the formation of three dimensional interpenetrating networks of inner pores within the islands. Ultimately, the porous islands represent electrodes with higher inner geometric surface area. These pores in-situ created by hydrochloric acid liquid-phase-diffusion will be electrocatalytically accessible to the NaCl electrolyte.

4.2.2.2 Impedance behaviour of porous electrode coatings

The substrate/oxide coating/electrolyte interfaces can be well investigated by using the electrochemical impedance spectroscopy (EIS). The electrode interface response to the applied small-signal stimulus in the frequency domain represents the information of adsorption, diffusion, electron transfer at the electrode/electrolyte interface. The electrochemical system can be described by using the serial and/or parallel combinations of various circuit elements, such as resistor, inductor and capacitor.

Typically, the impedance data are analyzed by fitting the data to an equivalent circuit. The most often used equivalent circuit for mixed metal oxide electrode coatings is shown in Figure 4.30a, which contains a ohmic resistance element (R_e), a double layer capacitance (C_{dl}) in parallel with a charge transfer resistance for chlorine evolution reaction (R_{ct}), a film capacitance (C_f) in parallel with a film resistance (R_f). All capacitors can be replaced by constant phase elements (Q) to account for the inhomogeneities in the electrode system. The impedance of this equivalent circuit $R_e(C_{dl}R_{ct})(C_fR_f)$ has the expression:

$$Z\ \omega\ = R_e + \frac{1}{j\omega C_{dl} + \frac{1}{R_{ct}}} + \frac{1}{j\omega C_f\ + \frac{1}{R_f}} \tag{4.2}$$

For the porous electrode coatings, the porosity or roughness of the oxide matrix could be expected to lead to a frequency dispersion of the interfacial impedance. A transmission line

model is generally used to describe the electrode system considering that the electrochemical reaction could take place down the depth of the pore [117]. Figure 4.30b shows the physical model of electrode coatings with cylindrical pores. Accordingly, the impedance of this equivalent circuit $R_e(C_{dl,out}R_{ct,out})(C_{dl,in}R_{ct,in})(C_fR_f)$ has the more complex expression:

$$Z(\omega) = R_e + \frac{1}{j\omega C_{dl,out} + \frac{1}{R_{ct,out}}} + \frac{1}{j\omega C_{dl,in} + \frac{1}{R_{ct,in}}} + \frac{1}{j\omega C_f + \frac{1}{R_f}} \tag{4.3}$$

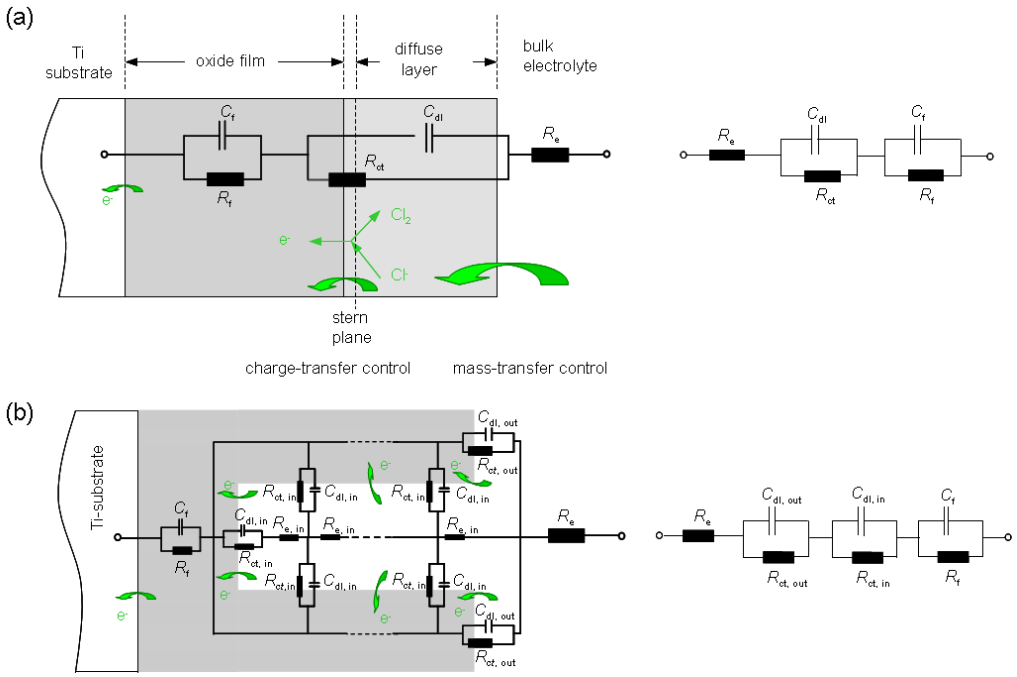

Figure 4.30. Physical model and equivalent circuit used to simulate the electrode response and to fit the impedance data for the present electrodes with $Ru_{0.3}Sn_{0.7}O_2 \cdot x\, La_2O_3$ coatings. (a) The conventional mixed metal oxide electrode, (b) porous electrode with a cylindrical pore accessible to the electrolyte [118,119]. R_e describes the ohmic resistance of the electrolyte, (R_fC_f) describes the coating/substrate interface, ($R_{ct}C_{dl}$) describes the active coating/solution interface, R_{ct} describes the charge transfer resistance and C_{dl} describes the double layer capacitance.

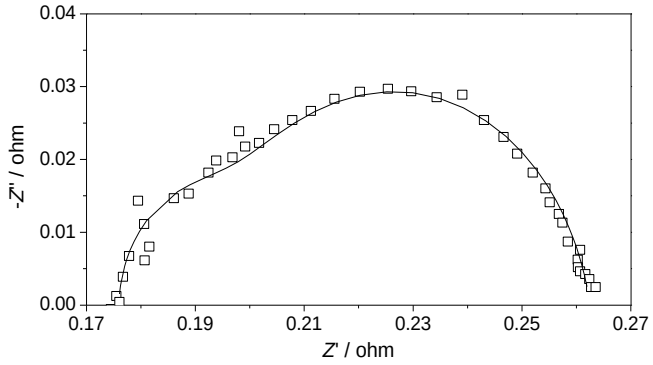

Figure 4.31. Nyquist plot (dotted points) for the film electrodes $Ru_{0.3}Sn_{0.7}O_2$ measured with a rotating disk electrode (2000 rmp) at an applied current density of 56.6 mA cm^{-2} in 3.5 M NaCl, pH 3 at room temperature. Solid curves show the fitting results by using equivalent circuit: *R*(*CR*)(*CR*).

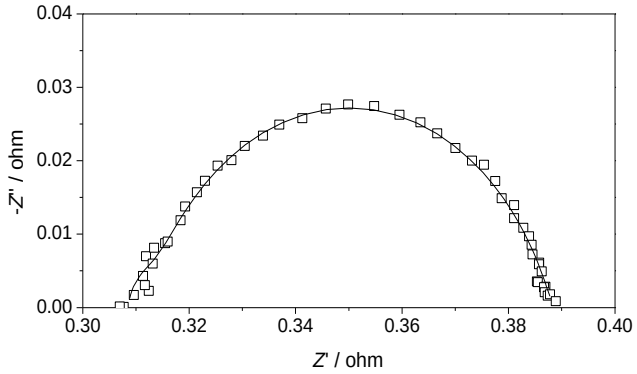

Figure 4.32. Nyquist plot (dotted points) for the film electrodes $Ru_{0.3}Sn_{0.7}O_2 \cdot 0.15\ La_2O_3$ measured with a rotating disk electrode (2000 rmp) at an applied current density of 56.6 mA cm^{-2} in 3.5 M NaCl, pH 3 at room temperature. Solid curves show the fitting results by using equivalent circuit: *R*(*CR*)(*CR*)(*CR*).

The electrochemical impedance spectroscopy was recorded in 3.5 M NaCl, pH 3 at room temperature using a rotating disk electrode (2000 rmp, exposed surface areas 1.77 cm^2) at applied current density 56.6 mA cm^{-2} (Figure 4.31, Figure 4.32), where the electric double-layer responds jointly with the Faradaic redox processes. The strongly scattered data points arising from the gas bubble-induced fluctuations in recording the electroanalytical signals have been rejected for further data fitting analysis. The impedance data in the low frequency region reflects the chlorine evolution reactions at the interface between the oxide coating and the electrolyte solution, whereas the impedance data at the high frequency

region is related to the oxide coating properties. A very good fit ($\chi^2 < 1 \times 10^{-4}$) for the impedance data has been achieved by using the equivalent circuit described in Figure 4.30. Two characteristic time constants ($\tau_c = \frac{1}{\omega} = RC = \frac{1}{2\pi f}$) corresponding to the two semicircles (Figure 4.31) were obtained for the $Ru_{0.3}Sn_{0.7}O_2$ coatings, whereas three characteristic time constants corresponding to the pore-containing coatings were observed.

Table 4.4. Parameters of the equivalent circuit used to describe the impedance behaviour of the $Ru_{0.3}Sn_{0.7}O_2 \cdot x\, La_2O_3$ coatings in 3.5 M NaCl, pH 3 at room temperature measured under galvanostatic impedance mode with a current density of 56.6 mA cm^{-2}. Physical units: Resistance, Ω; pseudocapacitance, mF.

x	0	0.05	0.15	0.20
Equivalent circuit	$R(CR)(CR)$	$R(CR)(CR)(CR)$	$R(CR)(CR)(CR)$	$R(CR)(CR)(CR)$
R_e	0.1775	0.2357	0.3096	0.737
C_{out}	1.901	1.039	1.649	2.188
R_{out}	0.05559	0.04595	0.04678	0.05381
C_{in}	-	11.75	22.14	53.70
R_{in}	-	0.02349	0.01973	0.01176
C_f	0.4153	0.1835	0.5598	1.061
R_f	0.02541	0.0124	0.01089	0.01399
χ^2	7.476E-5	8.827E-5	1.890E-5	6.652E-6

Conventional electrochemical techniques, such as cyclic voltammetry, encounter the problem when high current density is applied, that the bulk electrolyte ohmic drop will distort the measured electrode capacity behaviour. For impedance measurements, the bulk electrolyte ohmic drop (R_e) can be isolated from other electrochemical parameters (Table 4.4). The electrolyte ohmic drop depends on the distance between the working electrode and the reference electrode. The oxide film resistance R_f is about 0.01 Ω (Table 4.4) for the $Ru_{0.3}Sn_{0.7}O_2 \cdot x\, La_2O_3$ coatings corresponding to the small semicircle at high frequency

domain in the Nyquist plots (Figure 4.32). The film resistance originates from the mixed metal oxide coating and the interface between the oxide coating and titanium substrate. The small value in R_f indicates that the oxide coating is metallically conductive. Note that the R_f can be used for the investigation in electrode deactivation due to the passivation of titanium substrate. The parameter of C_{dl} reflects the number of electrocatalytically active sites, similarly to the voltammetric charge density (q_a) obtained in cyclic voltammetry measurements.

For the porous coatings $Ru_{0.3}Sn_{0.7}O_2 \cdot xLa_2O_3$ (x = 0.05, 0.15, 0.2), the outer surface response behaviour (C_{out}, R_{out}) is similar to the $Ru_{0.3}Sn_{0.7}O_2$ coatings, whereas the inner surface exhibits the distinct capacitive behaviour (C_{in}) due to the existence of numerous accessible nanopores. The effect of the electrode pore geometry, such as the pore radius and depth, is complicated and not well understood so far, especially for the gas-evolving electrodes. On the one hand, the electrodes should be designed by using nanoporous structures to maximize the specific electrode surface areas; on the other hand, the pores should be designed so that the movement and migration of reactant ions and product molecules are not inhibited. Some theoretical models have been developed to consider the pore geometry [120]. The dependence of the gradient of the potential distribution along the center of the pore and ion concentration on the pore radius and depth has been modelled using a planar electrode containing cylindrical pores. The charging time of the Stern layer (where the electrochemical reactions occur, such as the ion dissociation and redox couples) and the diffuse layer, the percentage distribution of the total charge within the Stern layer and the diffuse layer are governed by the surface potential, ion concentration, pore depth and radius. For low surface potential, the diffuse layer accounts for a larger percentage of the total charge than the Stern layer. The charging behaviour of porous $Ru_{0.3}Sn_{0.7}O_2$ electrode coatings will be discussed in the next section.

4.2.2.3 Charging behaviour of porous electrode coatings

The analytical technique to characterize the interfacial response of the electrode in the electrolyte are impedance, charging transient, and open circuit potential relaxation after interrupting the polarization current [121,122,123]. The electrochemically accessible

surface area of a rough and porous electrode was characterized herein based on the electrochemical charging behaviour of porous electrode coating under slightly galvanostatic polarization.

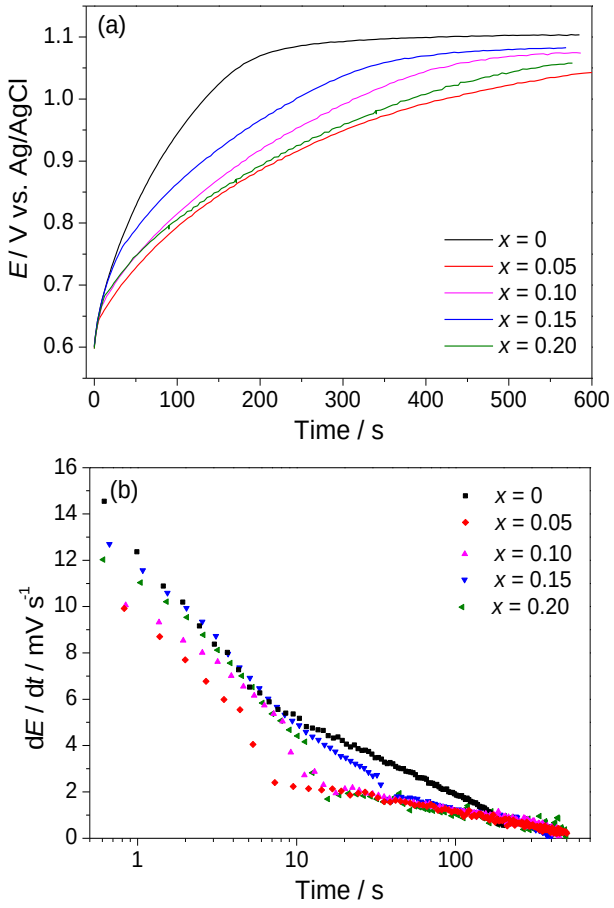

Figure 4.33. (a) Representative potential response of $Ru_{0.3}Sn_{0.7}O_2 \cdot x\, La_2O_3$ electrode coatings with different porosity to the suddenly applied current density step at j = 0.5 mA cm^{-2}. Conditions: forced electrolyte convection cell, 3.5 M NaCl, pH 3 at 50 ^{o}C. Time record length: 10 min. The data points were recorded with a time interval of 5 s. (b) The slope of the potential response versus log(t) corresponding to the recorded data in (a).

Galvanostatic charging behaviour of the porous electrodes was characterized at low polarization current density conditions (j = 0.5 mA cm^{-2}) in order to get a comprehension of the electrode potential $E(t)$ dependence on the porosity, as shown in Figure 4.33a. At low polarization current density conditions, the chlorine evolution reactions proceed mildly through molecular diffusion into bulk electrolyte rather than the formation of bubbles (see:

wavelet analysis of bubble-induced potential noise in Section 4.4.4). After the current supply, the initial potential increases instantaneously to about 0.6 V. The potential plateau was observed after 3 min for $Ru_{0.3}Sn_{0.7}O_2$ electrode coating, whereas the potential equilibration time or the response time of the system to a step current exceeds 10 min for the pore-containing electrode coatings, which indicates a progressively deeper penetration of the electrolyte into the inner spaces for the pore-containing electrode coatings.

The rate of the potential response (the charging dynamics) slows down linearly with the logarithm of time, log(*t*), (Figure 4.33b) with a turning point at around 10s. Before this turning point, the rates of potential response are close to each other for different coatings, indicating that the similar charging behaviour of the outer exposed surface and wider cracks, which is independent of the inner structure and morphologies. The decrease in the charging rate, especially for the pore-containing oxide coatings, after the turning point implies that the slow inner pore charging process prevails. For the anodic charging behaviour of RuO_2 film electrodes in $HClO_4$, it has been reported [124], similarly, that the potential response takes several to about 20 min to reach a final steady-state potential plateau. Galvanostatic anodic charging curves for the porous PbO_2/Ti electrodes in Na_2SO_4 solution show the same charging profiles [125].

Note that the time-dependent potential, in response to a current step, is the potential difference between the electrode and a point (where the tip of the Luggin capillary reference electrode is positioned) in the bulk solution. It consists of the potential difference across the Stern layer and the potential difference across the part of the diffuse layer according to the Gouy-Chapman-Stern model for the dilute solution [114]. For the concentrated solution (3.5 M NaCl as supporting electrolyte, for instance), the time evolution of the double layer, concretely, the expansion of the double layer due to the ion crowding into the nano-channels occurs until an equilibrium is reached.

The electrode/electrolyte interface behaves as a capacitor. In the absence of a redox couple at the electrode surface, the charge on the capacitor is proportional to the voltage drop across the capacitor. For the oxide film electrode, the capacitance is a function of the dielectric properties of the oxide material, electrode area, and the space between the electrode and the electrostatically bound ions (usually on the order of the Debye screening

length [126]). The charge-storage mechanism for the electric double-layer capacitor is that the energy is stored non-Faradaically by charging the electrochemical double-layer at the interface between the porous electrode and the electrolyte.

When the Faradaic reaction is involved at the electrode/electrolyte interface, the pseudocapacitance behaviour of the oxide film electrode originates from the ion diffusion and the parallel redox processes of the active species (Eq. (4.1)). For the redox pseudocapacitor, the total applied current ($i_0 = j_0 \cdot A = 0.5$ mA) at the porous electrode consists of the current for charging the double layer (non-Faradaic current or capacitive current, $\mathrm{d}Q_{\mathrm{dl}}/\mathrm{d}t$) and the current corresponding to the Faradaic charge transfer reaction (Faradaic current, i_{F}) at the electrode/electrolyte interface [127], i.e.:

$$\begin{aligned} i_0 &= i_{\mathrm{F}} + \frac{dQ_{\mathrm{dl}}}{dt} \\ &= i_{\mathrm{F}} + C_{\mathrm{dl}}\frac{dE}{dt} + E\frac{dC_{\mathrm{dl}}}{dt} \end{aligned} \tag{4.4}$$

The Faradaic current (i_{F}) depends on the electron transfer kinetics and the diffusion rate of the redox species to the electrode surface. For the mass transfer controlled process, the current is related to the diffusion rate of the redox species ($i = nFAJ$, where n is the number of electrons, F is Faraday's constant, A is electrode area, and J is the flux of the redox species to the surface governed by the Fick's law). At the slight polarization conditions, the electrode reaction is under kinetic control.

The charge of the double layer (Q_{dl}) is a function of the double layer capacitance (C_{dl}) and electrode potential (E), i.e., $Q_{\mathrm{dl}} = f(C_{\mathrm{dl}}, E)$. The C_{dl} is dependent on the surface coverage percentage of the electrode by gas bubbles at intensive gas evolution conditions. For simplicity, at low applied current density conditions the surface coverage of the electrode by gas bubbles is negligible, and then the electric double layer capacitance (C_{dl}) is assumed as constant at steady state. Before reaching the steady state, the electric double-layer capacitance increases due to the increasing utilization of the inner surface. In the case that the Faradaic current is substantially greater than the double layer charging current, the analysis of the capacitive behaviour of the porous electrodes based on the galvanostatic charging profiles becomes meaningless. For the non-ideally polarizable electrode (i.e., the Faradaic reaction is inevitable), when electrochemical Faradaic reactions are not

significant, after applying a current step, the chemical ions adsorption and desorption occur at the interface of outer plane surface and inner pores.

The charging processes investigated in this work for the porous RuO_2-based electrode coatings are more complicated than the characterization of the supercapacitance behaviour of electrode materials. The process involves the electric double-layer charging, the pseudocapacitive charging of the Faradaic protonation/deprotonation process $RuO_x(OH)_y + \delta H^+ + \delta e^- \rightleftharpoons RuO_{x-\delta}(OH)_{y+\delta}$ (Eq. (4.1)), and the interference of the chlorine evolution reactions (Eq. (2.5)). The quantitative separation of various factors is difficult.

4.2.3 Conclusion

In this section, the oxide coatings with the designed morphology have been achieved experimentally. With the intention to protect the underlying titanium substrate against passivation, the crack-free and impermeable inner oxide layer has been prepared. In order to increase the electrocatalytically accessible active surface area, a nanopore-containing oxide layer has been prepared, which can be used potentially as top layer onto the above mentioned crack-free inner layer.

The electrode coatings used for the chlorine evolution reactions possess the typical mud-crack surface feature, which is favourable to increase the utilization of the electrocatalyst materials due to the penetration of electrolyte into the gaps (with the size of about 1 μm). Unfortunately, the cracks facilitate simultaneously the direct contact of the electrolyte with the underlying substrate under the caustic conditions. Electrode deactivation occurs prior to the complete dissolution of the active ruthenium component as has been confirmed by other researchers. Therefore, crack-free oxide coatings were fabricated as protective inner layer. No cracks were observed at the surface of coatings from the SEM images from the scale bar 10 μm to 100 nm by controlling the reduplicate dipping/drying/sintering process. CV as an in-situ analysis technique confirms the impermeable character of the obtained crack-free coatings.

Nanopore-containing oxide coatings were prepared by the chemical leaching method. The increase in the electrocatalytic accessible surface area was investigated by CV and EIS. The existence of the inner pores within the oxide matrix exhibits the unique electrochemical response behaviour. The charging behaviour of the porous electrode coatings was studied by monitoring the time-dependent potential response under the slight galvanostatic polarization conditions. Further investigations of the pore size and shape and its possible influence on the bubble release have to be performed to obtain the optimal pore geometry.

4.3 Solvothermal-assisted synthesis

4.3.1 Phase structure of Ru-Ti-O system

The oxide materials prepared by sol-gel method are more often amorphous in the xerogel stage, post-sintering is necessary to crystallize the xerogel, to remove the residual organics, to reinforce the thermal and mechanical stability and to increase the wear resistance and durability. The final phase structure of the mixed oxide in the Ru-Ti-O system depends on the thermodynamic conditions. Rutile-type Ru-Ti-O solid solution is the most common structure used as active phase for chlorine evolution reactions. Depending on the preparation conditions such as sintering temperature [128], sintering atmosphere [129], Ru/ Ti ratio [130], the product form (such as powders, thin films) and the underlying substrates [131], anatase structure of single TiO_2 or anatase Ru-Ti-O solid solution presents a secondary phase or a major phase [104] coexisting with rutile structure.

In view of the Ru-Ti-O employed as electrocatalyst coatings for the chlorine evolution reactions, two necessary conditions have to be satisfied: i) the electronic conductivity of the oxide coating, ruthenium species as conductive components should ensure the continuous conductive path in the oxide coating matrix; ii) coating stability, which is obtained by thermal sintering of the gel body. Thus the feasibility to modify the Ru-Ti-O coating phase structure under the restricted conditions of Ru/Ti ratio (15~40 Ru mol%) and thermal sintering temperature (450 ^{o}C) becomes a remarkable issue.

At ambient pressure TiO_2 exists in three different polymorphs: anatase, rutile, brookite. The structure parameters are listed in Table 4.5. The phase transition from the metastable anatase to the thermodynamically stable rutile can be induced by various factors, such as ion impurities, thermal sintering etc., as shown in Figure 4.34. Further details concerning the effects of pressure-temperature on the TiO_2 polymorphs: anatase, brookite, rutile and TiO_2-II (orthorhombic, *Pbcn*), TiO_2-B (monoclinic, $P2_1/c$), please refer to [132,133].

Table 4.5. Data for some TiO_2 polymorphs [134].

Structure	Space group	Density / g cm^{-3}	Unit-cell parameters / Å
Rutile, tetragonal	$P4_2/mnm$	4.13	a = 4.5933, c = 2.9592
Anatase, tetragonal	$I4_1/amd$	3.79	a = 3.7852, c = 9.5139
Brookite, orthorhombic	$Pbca$	3.99	a = 9.17, b = 5.46, c = 5.14

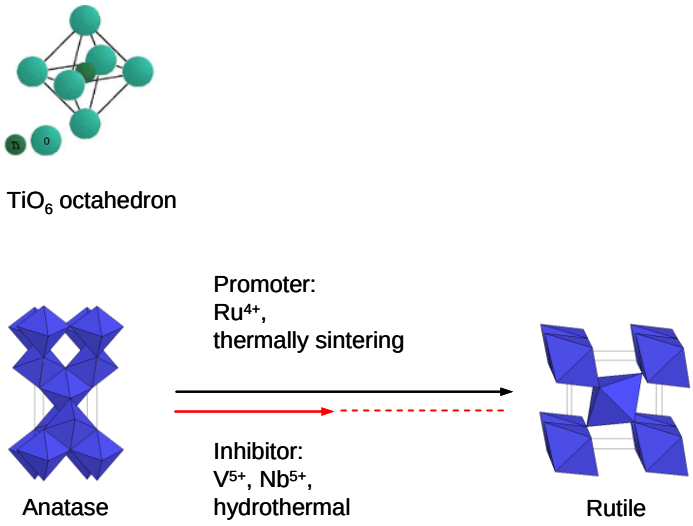

Figure 4.34. (top) The TiO_6 octahedron building block for various TiO_2 polymorphs. The linkage manners of the TiO_6 building block are different for the various TiO_2 polymorphs. (bottom) The linkage manners TiO_6 octahedra for anatase and rutile configuration and the anatase-to-rutile transition induced by various factors, among which the hydrothermal processing could inhibit the anatase-to-rutile phase transition.

For particular applications such as photocatalysts, the anatase phase is desirable. In such cases, the inhibition of the phase transition has been put into practice. The Gibbs free energies of the different polymorphs are temperature and pressure dependent ($\Delta G = \Delta U + P \cdot \Delta V - T \cdot \Delta S$). The high pressure-induced phase transition prefers the more dense structure with increased atoms or ions coordination number. On the contrary, the high temperature-induced transition favours the more open structure with lower atoms or ions coordination number [135]. Therefore, high pressure and high temperature cause opposite effects in the crystallization process. Based on this fact, a pressure-induced crystallization route was adopted in the following sections to modify the phase structure of the Ru-Ti-O coating system.

4.3.2 Solvothermal crystallization of Ru-O-Ti xerogel coatings

Solvothermal processing routes (or termed as hydrothermal when H_2O used as filling solvent) are widely used to convert amorphous materials to crystalline ones and increase their crystallinity. The solvothermal crystallization is a particular route operated under auto-generated pressure (the driving force for the phase transition) within a sealed autoclave at a temperature above the boiling point of the filling solvents (H_2O or organic solvents). The high pressure conditions are more often used to produce the metastable-phase materials.

Prior to the solvothermal processing, the amorphous Ru-O-Ti coatings were obtained by repeating the drop-coating, air-drying, thermal stabilization (at 200 ^{o}C for 10 min) processes. The thermal stabilizing step is necessary to facilitate the wetting of the next drop of sol solution onto the existing layer and thus to obtain a thick layer. 2-propanol (physical properties see Table 4.6) used as solvent with a filling fraction of 12% was added into a Teflon sealed autoclave. The amorphous Ru-O-Ti xerogel coatings supported onto titanium plates (see Experimental section) were located into the Teflon holder and then the autoclave was heated with a ramping rate 10 ^{o}C min^{-1} to 150 ^{o}C (lower than the critical temperature 235.2 ^{o}C of 2-propanol, subcritical domain) and kept for different time.

The auto-generated pressure in the sealed autoclave can be estimated by using the Peng-Robinson equation of state proposed in the review by Rajamathi [136]: (A comparison of the Peng-Robinson equation of state with the van der Waals equation of state, please refer to *Appendix* A5.)

$$p = \frac{RT}{V_m - b} - \frac{a}{V_m{}^2 + 2bV_m - b^2} \tag{4.5}$$

where R = 8.314 J mol^{-1} K^{-1} is the gas constant; p and T are the pressure and temperature, respectively; V_m is the molar volume of the liquid in the autoclave; the parameters a, b are given by:

$$a = \frac{0.45724 R^2 T_c^{\,2} \left[1 + f_\omega \left(1 - T_r^{\frac{1}{2}} \right) \right]^2}{p_c} \tag{4.6}$$

$$b = \frac{0.07780 R T_c}{p_c} \tag{4.7}$$

where T_c, p_c are the critical temperature and critical pressure of the solvent 2-propanol; $T_r = T / T_c$ is the reduced temperature; $f_\omega = 0.37464 + 1.54226\omega - 0.26992\omega^2$; ω is acentric factor. Thus, the estimated pressure in the autoclave of the present system is around 2×10^6 Pa.

Table 4.6. Physical properties of pure 2-propanol [137].

Molecular weight / g mol^{-1}	Boiling point / K at 1atm	Critical temperature / K	Critical pressure / Pa	Acentric factor
60.097	355.48	508.31	4.7343×10^6	0.66615

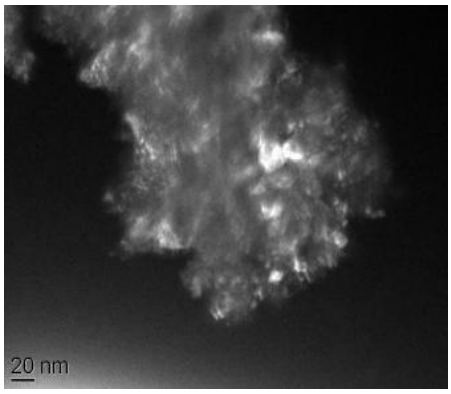

Figure 4.35. TEM image of powders scratched from the coating surface of as thermally stabilized (at 200 ^{o}C for 10min) $Ru_{0.25}Ti_{0.75}O_2$ coating.

$Ru_{0.25}Ti_{0.75}O_2$ coatings after thermal stabilizing treatment (200 ^{o}C) were amorphous-like (Figure 4.38). TEM image (Figure 4.35) of the powders scratched from the Ti-plate supported coatings shows the amorphous features. The amorphous coatings were crystallized under the subcritical curing conditions (gas-liquid co-existence state of 2-propanol). It is worth noting that the solvothermal processing of the xerogel coatings

(isolated from the filled solvent by a glass bottle) performed herein is different from the impregnating process of solvothermal reactions [138,139].

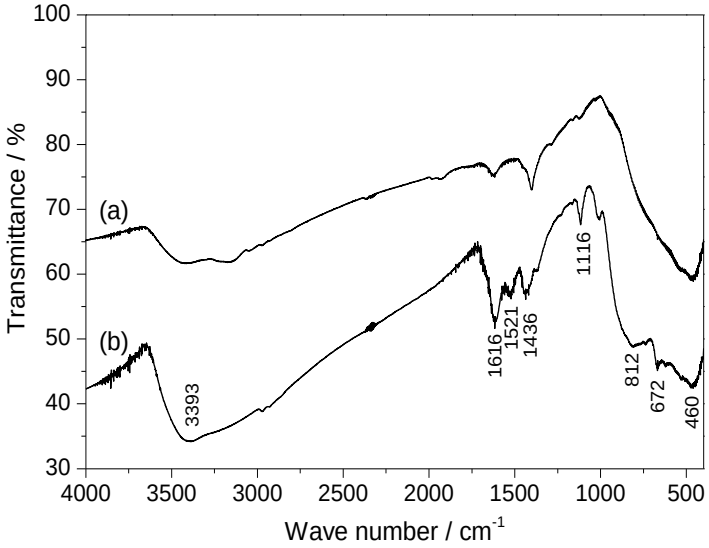

Figure 4.36. FTIR of $Ru_{0.25}Ti_{0.75}O_2$ xreogel powders measured using the KBr pellet method. (a) air-dried xerogel after solvothermal processing at 150 °C for 3 h, (b) air-dried xerogel. Xerogel powders were obtained by removing the solvents of the sol solution in uncovered glass bottle at room temperature. For solvothermal processing, powders were put into a glass bottle and then located in the Teflon holder.

The solvothermal effect in the decomposition of organics was investigated by powder FTIR spectroscopy (Figure 4.36). Xerogel powders were prepared by removing the solvents of the sol solution in uncovered glass bottle at room temperature for several days. For solvothermal processing, powders were put into a glass bottle and then located in the Teflon holder. The broad absorption band centered at 3393 cm^{-1} and weak absorption band at 1616 cm^{-1} in Figure 4.36 are associated with the physisorbed water [140]. Residual organic compounds were partially eliminated after solvothermal processing at 150 °C for 3 h, which can be confirmed by the decrease in absorption intensity at 1521cm^{-1} and 1436cm^{-1}(ν_{COO^-} vibrations) [141]. The vibration band at 812cm^{-1} in Figure 4.36b can be assigned to the O-O stretching mode of the Ti-OO-Ti or Ti-OOH groups [142]. The bands centered at 460cm^{-1} observed in the FTIR spectra are due to the Ru-O-Ti stretching vibrations [143]. The disappearance of the vibration band at 812 cm^{-1} after solvothermal

processing implies that the solvothermal processing promotes the further polycondensation reactions (oxolation reactions). The analysis of xerogel powders provides auxiliary information for the understanding of the structure evolution of xerogel coatings under the solvothermal curing conditions.

The surface morphologies of the solvothermally processed coatings were observed with SEM, as shown in Figure 4.37 (top, middle). The typical mud-crack structures were observed for the solvothermally processed coatings, both before and after post-sintering treatment. The initial cracks might have formed during the thermal stabilizing of the xerogel coatings at 200 ^{o}C (i.e. before the solvothermal processing). These cracks will help expose the inner layers of the coating matrix to the solvothermal curing atmosphere. After post-sintering, more cracks were formed due to the further release of the stress. The particle size of the $Ru_{0.25}Ti_{0.75}O_2$ after solvothermal curing and post-sintering was ca. 15 nm, observed from the TEM image (Figure 4.37, bottom).

Phase evolution as a function of post-sintering temperature of $Ru_{0.25}Ti_{0.75}O_2$ coatings without (Figure 4.38) and with (Figure 4.39) solvothermal processing was investigated by XRD. For the coatings prepared without solvothermal processing, the amorphous structure was observed below 300 ^{o}C. Above 350 ^{o}C, single rutile solid solution phase was formed. With the increase of sintering temperature until to 450 ^{o}C, the crystallinity was increased gradually. In contrast, for the coatings prepared with solvothermal processing, the distinct phase evolution behaviour was observed. The coating phase transition from amorphous to single anatase was observed after sintering at 300 ^{o}C. Therefore, we can deduce that the solvothermal processing is effective to help modify the coating phase structure. Post-sintering at higher temperatures (350~450 ^{o}C) results in the crystallization of the rutile phase. Thus the final structure was mixed anatase-rutile phase.

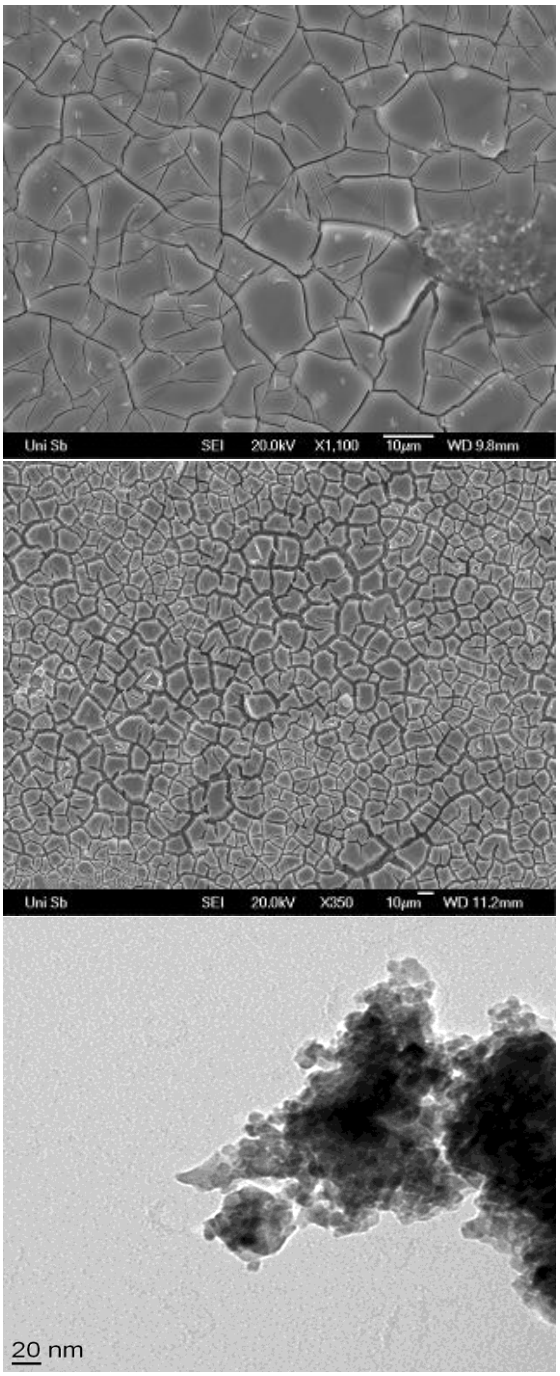

Figure 4.37. SEM images of surface morphologies for the solvothermally processed $Ru_{0.25}Ti_{0.75}O_2$ coatings (thermally stabilized at 200 ^oC for 10min) (top) and then post-sintered at 450 ^oC for 10min (middle). TEM images of powders scratched from the coating surface of $Ru_{0.25}Ti_{0.75}O_2$ coating after solvothermal processing and post-sintering at 450 ^oC for 10min (bottom).

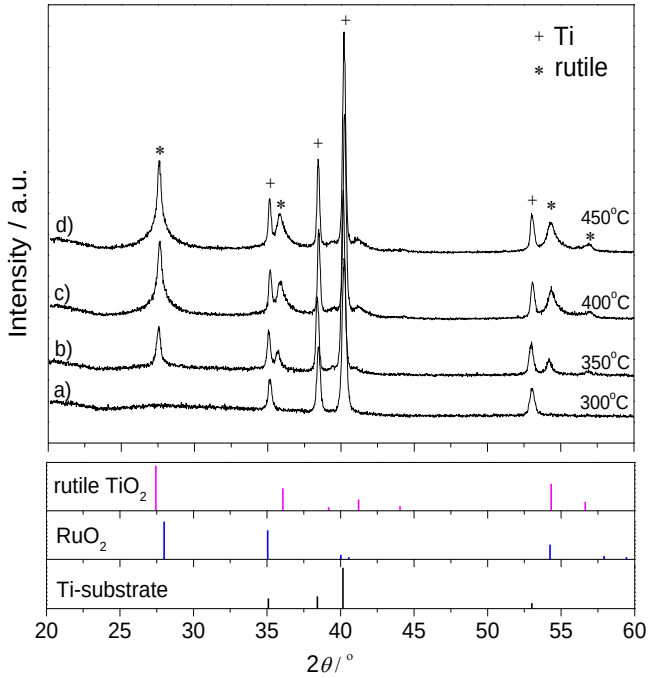

Figure 4.38. XRD patterns of $Ru_{0.25}Ti_{0.75}O_2$ coatings prepared by thermal stabilization at 200 °C for 10min each xerogel layer and then annealed at different temperatures for 10min.

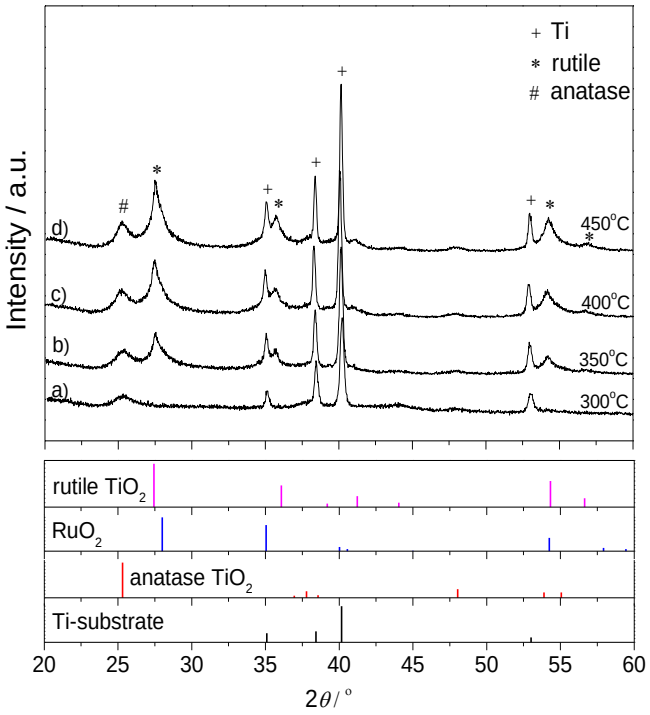

Figure 4.39. XRD patterns of $Ru_{0.25}Ti_{0.75}O_2$ coatings prepared by thermal stabilization at 200 °C for 10min each xerogel layer and then solvothermally processed at 150°C for 3 h, and finally annealed at different temperatures for 10 min.

4.3.3 Solvothermal processing parameters

To obtain the amorphous coatings for the subsequent solvothermal processing, the initial thermal stabilizing temperature is an important parameter, which can impose influence on the subsequent coating phase evolution and accordingly the electrochemical properties of $Ru_{0.25}Ti_{0.75}O_2$ coatings. Lower thermal stabilizing temperature provides more flexibility to modify the coating phase structure for the subsequent solvothermal curing. As shown in Figure 4.40, higher percentage of anatase phase was obtained in the final mixed anatase-rutile phase, when the coatings were prepared with the initial thermal stabilizing temperature of 100 ^{o}C. However, for the coatings prepared with the initial thermal stabilization temperature of 250 ^{o}C, as shown in Figure 4.41, only tiny anatase grains contained in the final anatase-rutile structure are observed. Compared with the exclusively thermal sintering prepared coatings, a common interest for the coatings prepared with solvothermal processing is that the anatase percentage in the final phase structure increases.

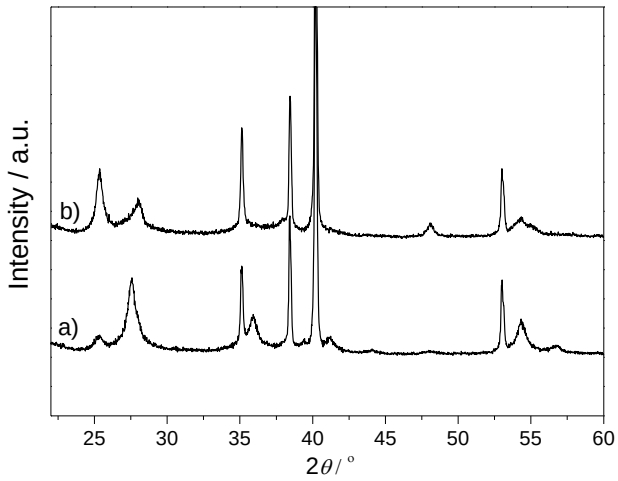

Figure 4.40. XRD patterns of $Ru_{0.25}Ti_{0.75}O_2$ coatings prepared by thermal stabilization at 100 ^{o}C for 10min each xerogel layer and then (a) thermally sintered at 450 ^{o}C for 1 h, (b) solvothermally processed at 150 ^{o}C for 24h, and finally sintered at 450 ^{o}C for 1 h.

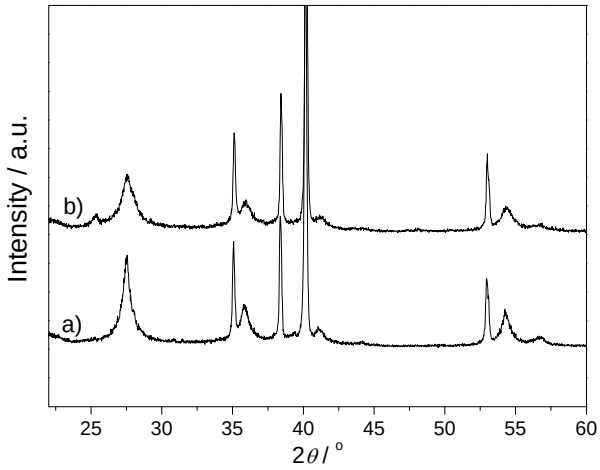

Figure 4.41. XRD patterns of $Ru_{0.25}Ti_{0.75}O_2$ coatings prepared by thermal stabilization at 250 °C for 10min each xerogel layer and then (a) thermally sintered at 450 °C for 1 h, (b) solvothermally processed at 150 °C for 24h, and finally sintered at 450 °C for 1 h.

The electrocatalytic activity of the solvothermally prepared coatings was evaluated by chronopotentiometry, as shown in Figure 4.42. The comparative investigation shows that the coatings prepared by exclusively thermal sintering possess higher electrode potential (ca. 1.42 V *vs.* Ag/AgCl) for the chlorine evolution reactions, whereas a decrease in electrode potential was observed for the coatings prepared by solvothermal curing. In particular for the coatings prepared with lower initial thermal stabilization temperature (100 °C), a decrease of electrode potential by ca. 170 mV has been achieved. This is extremely important as a demonstration for the reduction of energy-loss in the industrial chlor-alkali process. The explanation for the enhanced activity of the solvothermally processed coatings will be discussed in the following section.

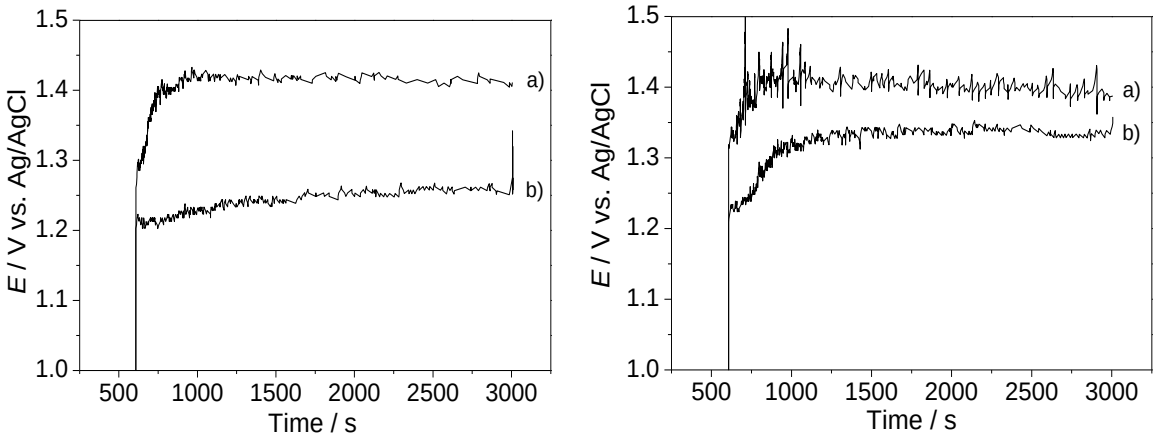

Figure 4.42. Chronopotentiometric curves of $Ru_{0.25}Ti_{0.75}O_2$ coatings recorded at a constant current density j = 100 mA cm^{-2} in 3.5 M NaCl, pH3 at room temperature. Left: corresponding to Figure 4.40; and Right: corresponding to Figure 4.41.

The molar content of ruthenium in the $Ru_xTi_{1-x}O_2$ binary oxide coatings is another important parameter to determine the electrocatalytic activity. The XRD patterns of coatings containing different ruthenium content are shown in Figure 4.43. In all three cases of x = 0.4, 0.25 and 0.15, the (110) peaks (after the peak position correction using the Ti-substrate (101) peak as reference, JCPDS 44-1294) were located in between the pure rutile TiO_2 (27.447^o) and pure RuO_2 (28.01^o), which indicates that the rutile solid solutions were formed. The (110) diffraction peak corresponding to rutile structure displays a shift toward higher angles with the increase of ruthenium content, which is related to the change in lattice parameters. The lattice parameters for the rutile RuO_2 and anatase, rutile TiO_2 are listed in *Appendix* A6. Except the $Ru_{0.15}Ti_{0.85}O_2$ coating, weak and broad anatase (101) peaks are present along with the rutile solid solution phase for the $Ru_{0.25}Ti_{0.75}O_2$ and $Ru_{0.40}Ti_{0.60}O_2$ coatings. $Ru_{0.40}Ti_{0.60}O_2$ coatings exhibit better apparent electrocatalytic activity for the chlorine evolution reactions than other coatings containing less ruthenium, as shown in Figure 4.44.

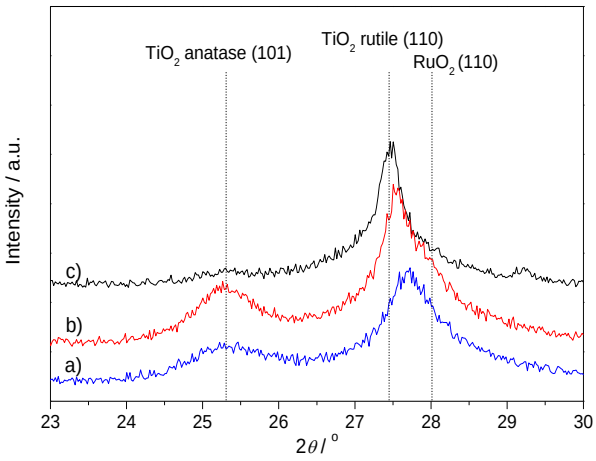

Figure 4.43. X-ray diffraction patterns of $Ru_xTi_{1-x}O_2$ coatings. (a) x = 0.4, (b) x = 0.25, (c) x = 0.15. Coatings were prepared by thermal stabilization at 200 °C for 10min each xerogel layer, and then solvothermally processed at 150 °C for 3 h and final post-calcination at 450 °C for 1 h.

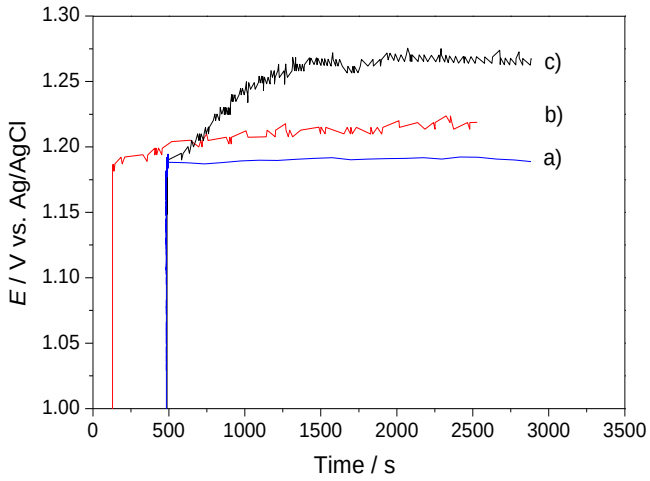

Figure 4.44. Chronopotentiometric curves of $Ru_xTi_{1-x}O_2$ coatings corresponding to Figure 4.43 recorded at a constant current density j = 100 mA cm^{-2} in 3.5 M NaCl, pH 3 at room temperature.

It is worth noting that the single anatase TiO_2 is an insulating phase, and pure TiO_2 is inert for chlorine evolution reactions. One of the motivations of using mixed RuO_2-TiO_2 binary oxides as electrocatalytic coating is that ruthenium (active component) and titanium have similar ionic radius and their oxides possess the same tetragonal rutile structure, which facilitates the formation of rutile solid solution structure (the active phase for chlorine evolution reactions).

It has been proven that the formation of anatase solid solution is possible for the $TiSnO_2$ [144] and $TiRuO_2$ systems [128], however, it is limited to lower Sn or Ru contents (< 10 mol%) and lower sintering temperatures (< 400 °C). In this case, the materials are worthless to be used as electrocatalysts for chlorine evolution reactions. It is a contradiction to obtain electrocatalysts with high activity (which requires the higher ruthenium content) and simultaneously with anatase solid solution structure.

4.3.4 Structure-property correlation of sol-gel/solvothermal prepared $Ru_{0.4}Ti_{0.6}O_2$ coatings

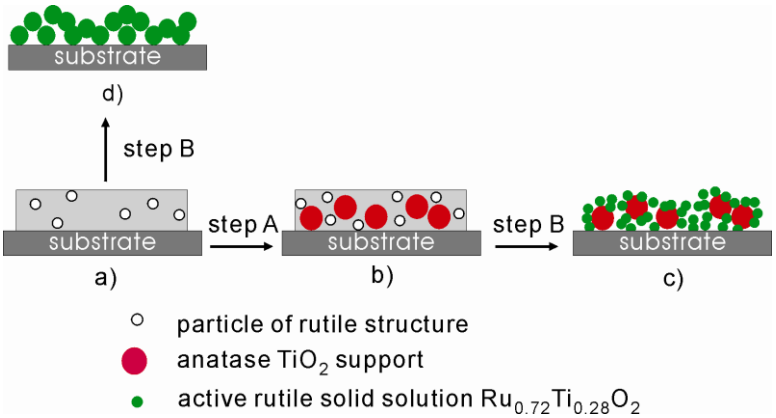

Figure 4.45. Schematic illustration of the coating structure formation of in-situ supported rutile nanocrystals $Ru_{0.72}Ti_{0.28}O_2$ onto anatase TiO_2. (a) Ru-O-Ti xerogel coating with rutile-type local order structure; (b) coating containing anatase TiO_2 pre-crystallized by solvothermal processing (step A, 150 °C for 24 h) of (a); (c) coating with supported structure of $Ru_{0.72}Ti_{0.28}O_2/TiO_2$ after post-sintering treatment (step B, 450 °C for 1 h) of (b); (d) coating with single rutile structure obtained by post-sintering treatment (step B) of (a).

To explain the experimental data for the observed enhancement of electrocatalytic activity of the mixed anatase-rutile $RuTiO_2$ coatings prepared by solvothermal curing, a systematic investigation of the structure-property correlation was carried out by using $Ru_{0.4}Ti_{0.6}O_2$ coating as an example. The detailed procedure to obtain the coating is illustrated in Figure 4.45. Starting from the Ru-O-Ti xerogel coating (Figure 4.45a), two different routes were

adopted to obtain the resulting coating: i) exclusive post-sintering treatment, a) → d); ii) solvothermal curing with subsequent post-sintering, a) → b) → c).

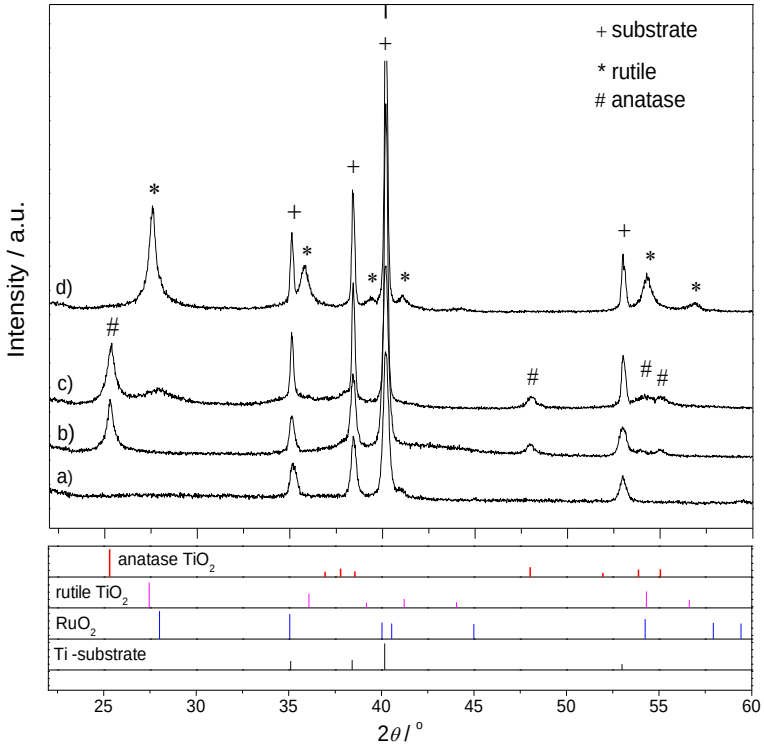

Figure 4.46. XRD patterns of electrodes with coatings (a), (b), (c) and (d) corresponding to (a), (b), (c) and (d) in Figure 4.45.

The phase development of the deposited Ru-O-Ti xerogel coatings on titanium substrates both with and without solvothermal processing was studied by XRD (Figure 4.46) and Raman spectroscopy (Figure 4.48). As shown in Figure 4.46a, the amorphous structure of the thermally stabilized Ru-O-Ti xerogel coatings was confirmed and only the presence of diffraction peaks from the titanium substrate (JCPDS 44-1294). Raman spectra, applied as a sensitive local probe (Figure 4.48a), show the vibration bands at 610, 114 cm^{-1}, assigned to the A_{1g} and B_{1u} mode of rutile lattice [145,146], suggesting the formation of rutile particles within the xerogel coatings. Post-sintering treatments of the xerogel coatings result in the densification and crystallization of the gel networks. Similarly to what has been reported, by exclusively direct thermal sintering of Ru-O-Ti xerogel coatings at 450 ^{o}C for 1 h (Figure 4.46d), a single rutile solid solution phase with a rutile crystallite size of 17 nm was formed (Table 4.7).

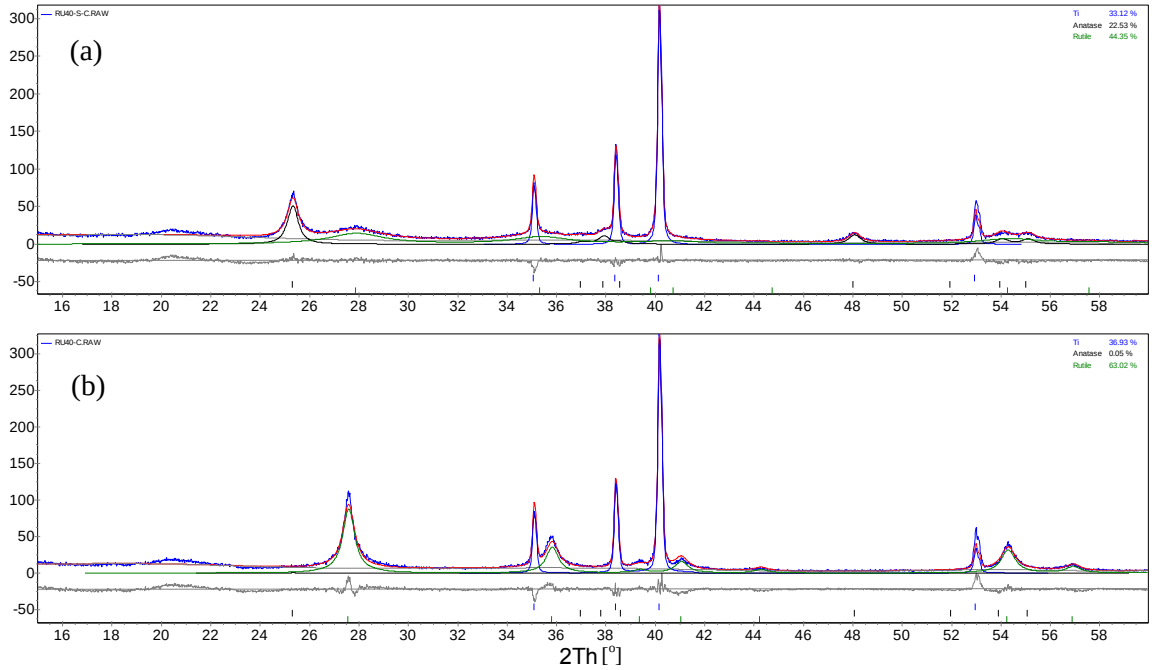

Figure 4.47. (a, b) Rietveld structure refinement of X-ray diffraction patterns corresponding to the diffraction profiles in Figure 4.46c, d respectively. Red curve is the fitting result. Phase composition (Ti substrate, anatase TiO_2, rutile $Ru_xTi_{1-x}O_2$) and its weight percent, lattice parameters were obtained and summarized in Table 4.7. Commercial TiO_2 P25 was used for the diffractometer instrument calibration.

In contrast, starting from the amorphous Ru-O-Ti xerogel coating, the crystallization induced by solvothermal processing (150 ^oC for 24 h) results in the formation of a single anatase phase (Figure 4.46b). Consistent with the XRD results, a new sharp Raman band (Figure 4.48b) at 153 cm^{-1} along with weak bands at 204, 399 cm^{-1} can be assigned to the anatase characteristic bands of $E_{g(1)}$, $E_{g(2)}$, B_{1g}, respectively [144,147]. A rutile phase with a weak and broad (110) peak appears after the post-sintering treatment (Figure 4.46c). The crystal growth of the rutile structure in the coating is retarded significantly based on the Rietveld refinement analysis results (ca. 3 nm) (Table 4.7). Recalling that the rutile nanoparticles have been detected by Raman spectroscopy within the xerogel coating, thus it can be deduced that the nanocrystals with the size of 3 nm originate from the growth of these initial rutile nanoparticles on the local scale surrounding the anatase phase (ca. 20nm) (Table 4.7).

For the coating prepared by the a) → b) → c) route (Figure 4.45), the lattice parameters obtained by Rietveld structure refinement (Table 4.7) confirmed the formation of rutile-type $Ru_xTi_{1-x}O_2$ solid solution, where $x = 0.72$ was calculated using the Vegard's law [148]:

$$c/a_{Ru_xTi_{1-x}O_2} = c/a_{TiO_2} \cdot (1-x) + c/a_{RuO_2} \cdot x \quad (4.8)$$

i.e. $0.6775 = 0.6442 \times (1-x) + 0.6906\ x$.

Table 4.7. Results of Rietveld refinement of XRD data corresponding to Figure 4.45 c, d.

Coating	Phase	Phase wt%	*a* / Å	*c* / Å	Crystallite size / nm
Figure 4.45c	rutile	66.3	4.526(4)	3.066(5)	3.4(2)
	anatase	33.7	3.788(1)	9.497(4)	20.3(7)
Figure 4.45d	rutile	100	4.575(1)	2.997(1)	17.2(4)

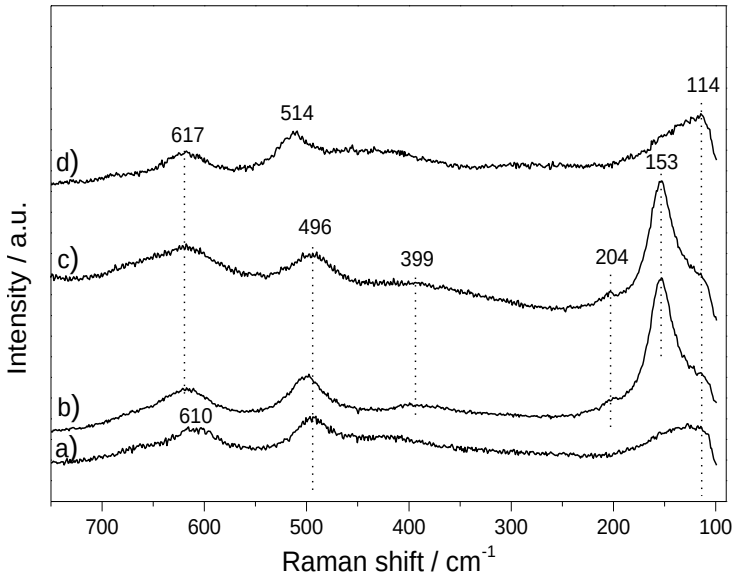

Figure 4.48. Raman spectra of coatings (a), (b), (c) and (d) corresponding to (a), (b), (c) and (d) in Figure 4.45. A HORIBA-Jobin-Yvon LabRAM ARAMIS Raman spectrometer using a 632.8 nm excitation (He-Ne laser, 10 mW) was employed to record the Raman spectra and a silicon single-crystal was used to instrument calibration. The laser light was focused onto the sample using a 100× objective lens.

The Raman bands at 496 cm^{-1} (Figure 4.48c) show the evident shift from the E_g mode positions of rutile TiO_2 nanocrystals (447 cm^{-1}) [149] and rutile RuO_2 nanocrystals (511 cm^{-1}) [150], which is caused by the lattice distortion arising from the incorporation of Ti into the RuO_2. There is no evidence for Ru incorporation into the anatase TiO_2 lattice. These results reveal that the coating consists of rutile-type $Ru_{0.72}Ti_{0.28}O_2$ solid solution and undoped anatase TiO_2. Along with the quantitative Rietveld phase analysis (Table 4.7), the calculated Ru:Ti molar ratio in the coating is 41:59, which agrees well with the nominal composition (40:60).

For the coating prepared by the a) → d) route (Figure 4.45), the existence of a ruthenium-containing amorphous structure in the oxide matrix was confirmed by the Raman band at 514 cm^{-1} (Figure 4.48) attributed to RuO_2 E_g mode [150], since no separated RuO_2 phase has been detected in the XRD. Prior studies showed the complete crystallization of the Ru-O-Ti xerogel at higher temperatures (> 500 ^oC) [151]. It can be concluded that the solvothermal processing effectively assists the crystallization of oxide coating.

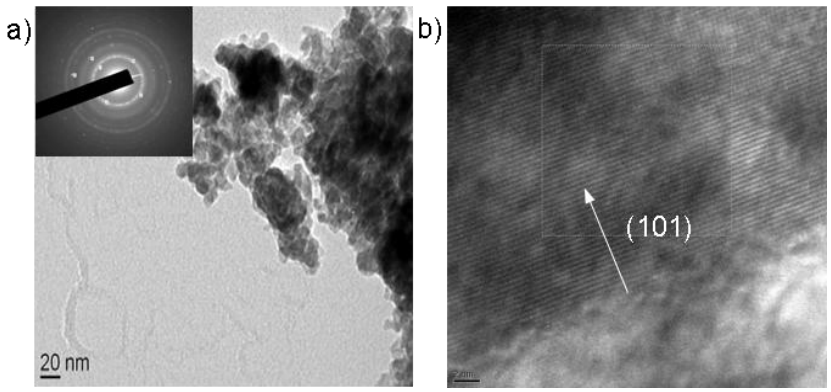

Figure 4.49. (a) The bright-field and (b) high-resolution TEM images (scale bar: 2 nm) of powder samples scratched from the coating prepared by a) → b) → c) route (Figure 4.45). The inset of electron diffraction pattern in (a) showing the diffraction rings of anatase TiO_2 phase. Powders were obtained by a mechanical scratching of the Ti-substrate supported coating and subsequently dispersed ultrasonically into ethanol. A drop of the particles dispersion was deposited on the TEM copper grid and allowed to evaporate under ambient conditions.

Unlike the O_2-rich thermal sintering, the solvothermal processing creates a particular crystallization environment, wherein atomic short-range diffusion, organics removal and restricted grains growth occur within the xerogel networks at mild temperature under elevated pressure conditions [152]. The undoped spherical anatase TiO_2 was formed by the local enrichment of titanium species oriented along the (101) direction, as visualized from the transmission electron microscopy images (Figure 4.49). Nanoclusters of a few nanometers in size were observed on the surface of anatase TiO_2, which are supposed to be rutile $Ru_{0.72}Ti_{0.28}O_2$ nanocrystals. The phase stabilization of the nanostructural TiO_2 exhibits a strong dependence on particle size and surface chemistry [153]. The as-obtained anatase TiO_2 particles are thermally stable during the post-sintering treatment and thus act as an ideal support for the subsequent dispersion of the active rutile phase [154]. Owing to the steric barrier effects of support and the restrained thermal motion of rutile particles, the detrimental rutile particle growth during the post-sintering is inhibited, which is beneficial for the practical applications. Although the undoped anatase TiO_2 is insulating, the electronic conduction path could be assured by interconnected particles of rutile $Ru_{0.72}Ti_{0.28}O_2$ or rutile particles separated with very small gaps (tunneling effect) [41].

The capacitive behaviour was examined by monitoring current densities of the oxide coatings in the acidified NaCl electrolyte (Figure 4.50). The number of electrochemically active sites of the coatings, estimated in terms of the integrated area of the anodic branches in the cyclovoltammograms, shows a 4-fold increase in the solvothermal/post-sintering prepared coating (Figure 4.50a) to that in the direct thermal sintering prepared coating (Figure 4.50b). This is roughly close to the increase in geometric surface area calculated by decreasing the crystal size from 17 nm to 3 nm, assuming spherical particle morphology. This suggests that active rutile nanocrystals in the solvothermal/post-sintering prepared coating are highly dispersed and electrochemically accessible. More importantly, the onset of the chlorine evolution reactions at much lower positive potential (ca. 0.85 V vs. Ag/AgCl) was observed for the electrode with the solvothermal/post-sintering prepared coating (Figure 4.50a), indicating a significant activity enhancement. Considering that only surface exposed species are responsible for the surface redox process, the significant increase in the coordinatively unsaturated surface sites due to the nanoscale effect can account for the enhancement in electrocatalytic activity of the in-situ supported rutile nanocrystals [110].

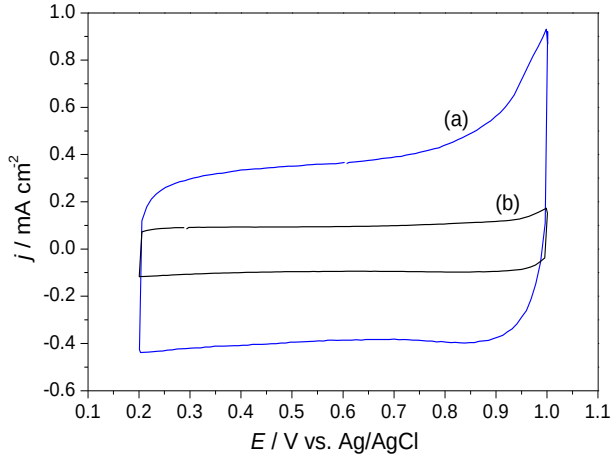

Figure 4.50. Cyclovoltammograms recorded for the electrodes with coatings (a) prepared by a) → b) → c) route and (b) prepared by a) → d) route (Figure 4.45) with a scan rate of 20 mV s^{-1} in 3.5 M NaCl aqueous solution, pH 3 controlled by HCl additions at room temperature, using RuO_2 coated titanium wire as counter electrode and Ag/AgCl as reference electrode. The reference electrode was carefully positioned close to the working electrode by using a Luggin capillary to minimize the uncompensated electrolyte resistance. The working electrodes were used with an exposed area of 1 cm^2.

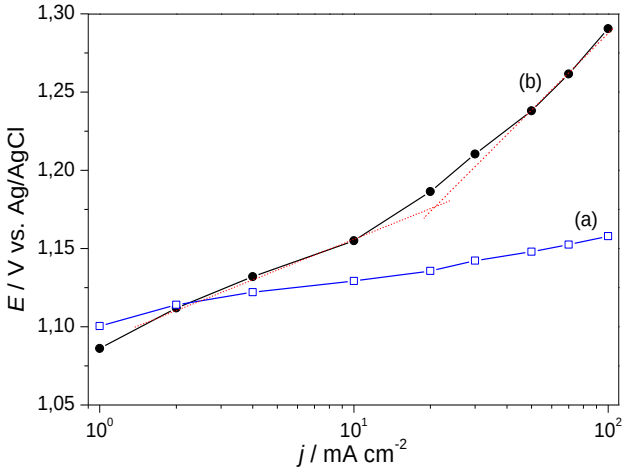

Figure 4.51. Galvanostatic polarization curves for the electrodes with coatings (a) prepared by a) → b) → c) route and (b) prepared by a) → d) route (Figure 4.45) recorded in 3.5 M NaCl, pH 3 at 50 °C.

The polarization behaviour of the electrodes between the solvothermal/post-sintering prepared coating (Figure 4.51a) and the direct thermal sintering prepared coating (Figure

4.51b) is compared. The former is clearly more active than the later, only a slight overpotential is necessary to keep an intensive chlorine evolution reaction for the solvothermal/post-sintering prepared coating. The difference in Tafel slope implies that a different reaction mechanism is involved. Two basic reaction paths of the chlorine evolution reactions on electrode surfaces have been proposed: Cl^- discharge (in which the adsorption species of Cl_{ad} on the active sites are formed) followed by either chemical desorption (CD) or electrochemical desorption (ED) [35]. Two Tafel slopes of 61 mV dec^{-1} (ED determining) and 148 mV dec^{-1} (mass transfer determining) were observed for the direct thermal sintering prepared coating at the lower and higher current density regions respectively. In contrast, one Tafel slope of 25 mV dec^{-1} (CD determining) was observed for the solvothermal/post-sintering prepared coating. The ED occurs on the active sites with the participation of electron transfer, but the CD may proceed on the inert anatase TiO_2 support. Anatase TiO_2 may play a role analogously to boron-doped diamond (BDD) support in RuO_2/BDD [40], the desorption rate of the intermediate species could be accelerated by their surface diffusion from the active sites to the neighbouring inert support due to the weakened binding interaction.

Based on the elaborate investigation of the structure-property correlations of solvothermal-assisted preparation of $Ru_{0.4}Ti_{0.6}O_2$ coatings, it can be concluded that the solvothermal curing of amorphous Ru-O-Ti xerogel coatings helps the formation of anatase TiO_2 nano-particles within the oxide coating matrix, which act subsequently as support particles for the growth of active rutile $Ru_xTi_{1-x}O_2$ solid solution phase. Due to the steric isolation effects of anatase TiO_2 particles, the crystal growth of active rutile structure is inhibited, which has been observed for the coatings with various ruthenium content and solvothermal processing conditions from the broad rutile (110) X-ray diffraction peaks by comparing with those prepared by direct thermal sintering. The novel structure of electrocatalytic coating with in-situ supported nanocrystals $Ru_xTi_{1-x}O_2/TiO_2$ exhibits a significant enhancement in electrocatalytic activity for chlorine evolution reactions. This structural and crystal size controlled preparation strategy of mixed oxide catalyst coatings will assist the design of advanced heterocatalysts, the understanding of the electrocatalytic effects at nanoscale, and help to improve the energy efficiency of industrial electrolysis.

4.3.5 Conclusion

In this section the crystallization of the Ru-O-Ti xerogel coatings has been tailored by using the solvothermal processing route under elevated pressure conditions in order to modify the phase structure of mixed oxide and to study the phase structure-property correlation of the binary $Ru_xTi_{1-x}O_2$ oxide coatings.

A single rutile solid solution structure of the $Ru_xTi_{1-x}O_2$ coatings is the usual phase structure obtained by the sol-gel route. Thermal sintering treatment of the xerogel coatings assists the combustion of organic residues and the amorphous-to-crystalline transformation. In contrast, solvothermal curing (150 ^oC, 2 MPa, 3~24 h) of the thermally stabilized (at 100~250^oC) xerogel coatings with the subsequent post-sintering (450 ^oC, 1h) promotes the formation of mixed anatase-rutile phase with improved electrocatalytic activity for the chlorine evolution reactions.

The phase and structure transition of the Ru-O-Ti xerogel coatings (nominal composition $Ru_{0.4}Ti_{0.6}O_2$) with and without solvothermal processing has been traced by using XRD, Raman spectroscopy. Phase identified in the final oxide coatings consists of a single anatase TiO_2 and rutile type $Ru_xTi_{1-x}O_2$ solid solution. Nanoscaled $Ru_xTi_{1-x}O_2$ solid solution particles (3 nm) were supported surrounding the larger anatase TiO_2 particles (20 nm). Attributed to the high dispersion of the active components (rutile solid solution particle) and the increase in the coordinatively unsaturated surface sites, a significant enhancement in the electrocatalytic activity has been achieved.

This work demonstrates a novel way to obtain the highly active oxide electrocatalyst coatings. The preparation of the alternative binary oxide system such as $RuSnO_2$, $RuVO_x$ using the proposed route could possibly exhibit the combined advantages such as the high activity and low ruthenium content based on the results obtained in Section 4.1.

4.4 Electrochemical noise analysis of gas-evolving electrodes

The electrochemical generation of gas molecules of chlorine at the electrode surface is a discharging process. The discharge current densities, which determine the production rate of chlorine, are related to the electrode overpotential, exchange current density of the electrode reactions, supersaturation of the electrolyte with gas molecules and the charge transfer coefficients, etc. [155]. The generation and removal of gas bubbles at the electrode surface cause additional ohmic drop due to the coverage and shielding effect of bubbles on the surface and vicinity of the electrode. As shown in Figure 4.52, individual gas bubble evolution is present at very low applied current densities and the nucleation-growth-detachment is the whole life course of bubble evolution in this case. Coalescence of adjacent bubbles could occur more frequently for the electrodes with poor wettability with electrolyte. Intensive bubble evolution at higher applied current densities results in the formation of a froth layer adjacent to the electrode.

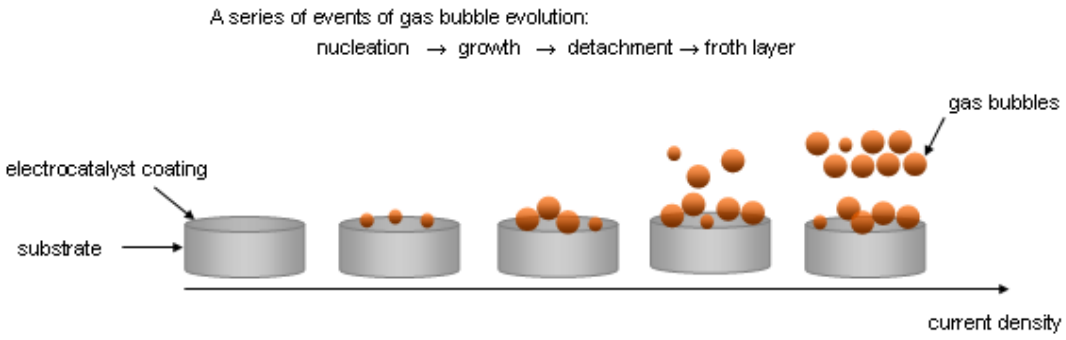

Figure 4.52. The sketch of gas bubble evolution events as a function of applied current densities. Theoretically, bubbles form starting at a low value of critical current density, below which the chlorine molecules diffuse into the bulk solution rather than form bubbles. The nucleation, growth and detachment events overlap at higher applied current densities

Bubble behaviour on the gas-evolving electrodes has attracted considerable interest in the electrolytic gas generation processes, such as H_2, O_2, Cl_2 [156,157,158,159]. Bubble-induced effects such as blocking the electrode active surface, adding extra ohmic drop, causing chaos in mass transfer and current distributions [59,160], are associated with energy losses in industrial electrolysis. Identifying the bubble behaviour is essential to get insight into the electrode materials and structure dependent properties in order to guide the optimization in electrode preparation. The quasi-periodic bubble events occurring at the electrode surface could result in periodic fluctuations of the electroanalytical signals, such as potential, current or resistance etc. This provides the possibility to identify the bubble evolution behaviour by analyzing the bubble-induced electrochemical noise.

4.4.1 Data acquisition of potential fluctuations

$Ru_{0.25}Ti_{0.65}V_{0.1}O_x$ ternary oxide coated titanium plates were used as working electrodes facing upwards with an exposed area of 1 cm^2. The electrode potential fluctuations $\Delta V(t)$ were recorded galvanostatically between 0.5 and 100 mA cm^{-2} in 3.5 M NaCl, pH 3 electrolytes at 50 ^oC (Figure 4.53). The time series of potential fluctuations data were acquired with a sampling interval (Δt) of 5 ms using EC-Lab software (Bio-Logic SAS). The reciprocal of the sampling interval is the sampling frequency ($f_s = 1/\Delta t$), which is 200 Hz in this case. According to the Nyquist sampling theorem, the highest frequency (f_{max}) in the original signal should be below 100 Hz ($f_{max} \leq \frac{1}{2\Delta t} = \frac{f_s}{2}$) as prerequisite for perfect signal reconstruction. The time series segments chosen out of the chronopotentiograms with a recording duration of T = 300 s were used for further signal analysis.

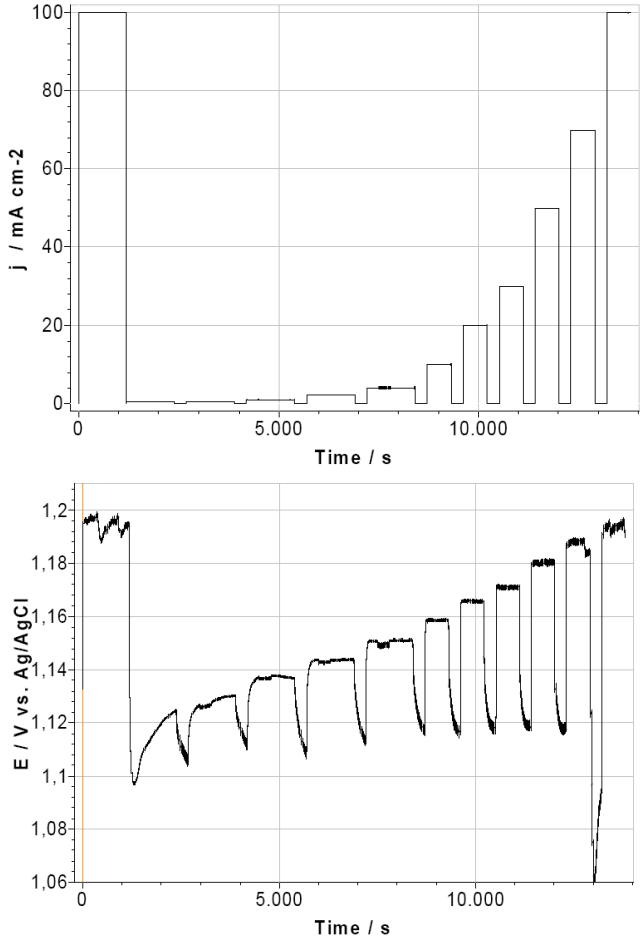

Figure 4.53. Top: Protocol for the measurement of electrode potential under galvanostatic polarization mode with an initial activation of the electrode at a current density of 100 mA cm^{-2} for 20 min, followed by the applied current density steps of j = 0.5, 1, 2, 4, 10, 20, 30, 50, 70, 100 mA cm^{-2}. Bottom: A representation of the electrochemical potential fluctuation signals observed in the measurement of electrode potential under galvanostatic polarization in 3.5 M NaCl, pH 3 at 50 ^{o}C in a forced convection cell for the $Ru_{0.25}Ti_{0.65}V_{0.1}O_x$ coating. The time series of potential fluctuations data were acquired with a sampling interval of 5 ms (i.e. sampling frequency 200 Hz) using the EC-Lab software.

The current noise from instrument output was also monitored (top in Figure 4.53) and its conversion to potential response was quite small compared to bubble induced potential fluctuations. However, the distortion in instrument current output could cause sharp jumps in the potential response. Therefore, the analytical segments must be chosen carefully to exclude an abnormal noise record.

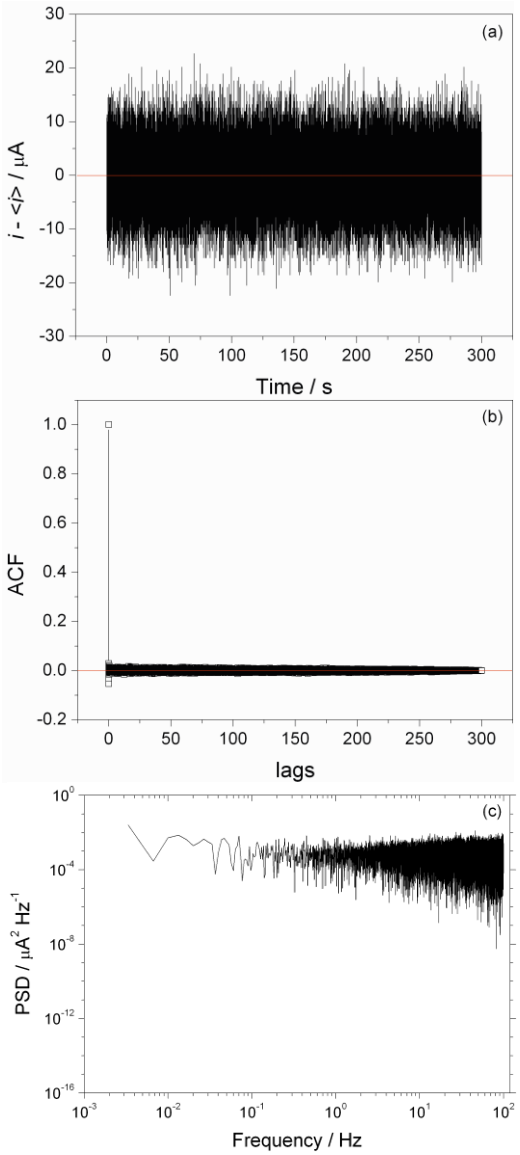

Figure 4.54. (a) The zero-averaged time series of current noise from the computer-controlled galvanostat with the set output of 100 mA, the current segment was chosen out of Figure 4.53, (b) the corresponding sample autocorrelation function (ACF) of the current noise, and (c) the corresponding Fourier power spectral density (PSD) of the current noise.

The time series segment of current noise from the instrument output and its autocorrelation function (ACF), Fourier power spectral density (PSD) were shown in Figure 4.54. The applied current was 100 mA with a variance of around 15 µA during the experiment (Figure 4.54a). The autocorrelation function of the random current noise shows a maximum value of one (ACF_{max} = 1) at zero time lag and approaches to zero elsewhere (Figure 4.54b). The Fourier PSD shows the flat profile at all frequencies and larger

fluctuations in the high frequency region (Figure 4.54c). These results indicate that the current noise from the galvanostat output is a random discrete white noise. We must keep in mind that the chaotic potential fluctuations $\Delta E(t)$, as a consequence of the accumulated events occurring between the working electrode and reference electrode [160], consist of periodic potential response induced by quasi-periodic bubble formation and their detachment along with superimposed random background noise, which is partially from the instrument current output noise.

4.4.2 Statistical analysis of potential fluctuations

One of the most common phenomena observed on the gas evolving electrodes is the electrochemical fluctuations of potential or current signals, as shown in Figure 4.53. Violent fluctuations in the measured potential value were observed at higher applied current densities, which are correlated to the intensive bubble evolution at the higher applied current density regions. A representative time series segment of potential fluctuations with a time length of 300 s chosen out of the chronopotentiometric curves recorded in Figure 4.53 was shown in Figure 4.55.

The sample standard deviation (σ) of a statistical data set is used commonly as a measure of the variability or dispersion. Larger standard deviation indicates that the data points are dispersed over a larger range of values. The large fluctuations in potential value are associated with the intensive bubble evolution process, whereas the slight fluctuations indicate a slow and mild bubble evolution process. As shown in Figure 4.56, a linear relationship exists between the standard deviation of potential fluctuations and the applied current density at the range of 0.5~70 mA cm^{-2}. However, for the standard deviation value calculated from the potential value measured at the current density of 100 mA cm^{-2}, the deviation of the data points away from the linear part is due to the drift of the measured potential signal. The uncertainty in the drift term of the electroanalytical signal makes it difficult to analyze and explain the experimental data. By extrapolating the linear part (blue line in Figure 4.56) to zero current density, the obtained intercept in y-axis is around 0.13 mV, indicating the existence of background noise even without chlorine bubbles present at the electrode surface.

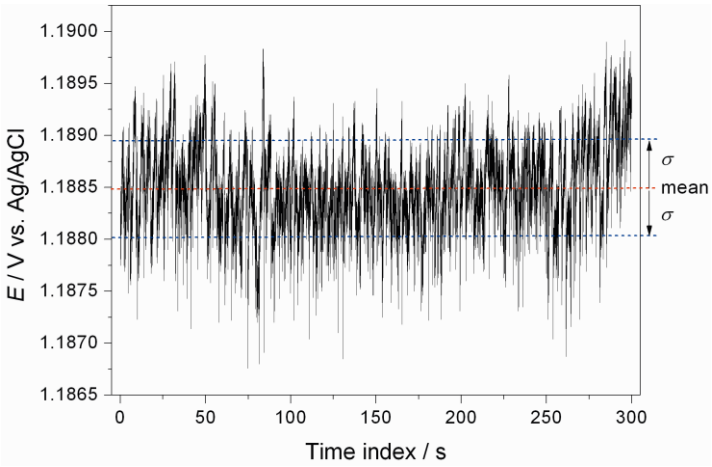

Figure 4.55. Potential fluctuation segment with a record length of 300 s chosen out of the chronopotentiometric curves recorded in Figure 4.53 at the current density of 70 mA cm^{-2}. The mean of the discrete time series is $<E>$ = 1.18849 V (red dashed line), and the standard deviation (σ) of potential noise data is 0.39941 mV (blue dashed lines).

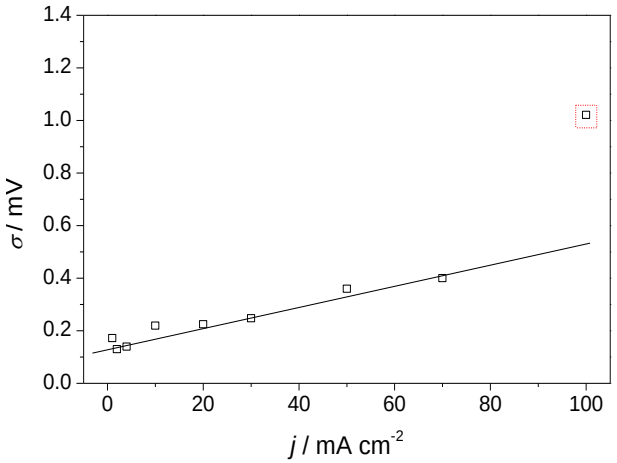

Figure 4.56. Plot of the standard deviation (σ) of potential fluctuation segments as a function of applied current density (j) in Figure 4.53. The data point (marked with red square) of standard deviation corresponding to the current density of 100 mA cm^{-2} deviates away from the linear part (solid line) due to the signal drift of recorded potential during the experiment.

For better clarity, the potential fluctuations $\Delta E(t)$ as a response to the applied current density (j) were normalized by $(E(t)-\mu)/\sigma$, where μ is mean value and σ is standard deviation. This allows us to observe clearly the local patterns and temporal structures (such

as time dependence, trend and periodicity) of the time series, as shown in Figure 4.57 in the time domain. The normalized time series with the amplitudes in the same range (-5~5) indicates that a linear correlation exists between *j* and σ of the potential fluctuations [161]. The drift in potential record (Figure 4.57d) reduces its amplitude due to the increase in σ. The variability of potential signal is strongly dependent on *j*. Long lasting random noise is the main feature at low *j* implying the slow bubble evolution, whereas transient impulse variance prevails at high *j* as the consequences of the intensive chlorine evolution events.

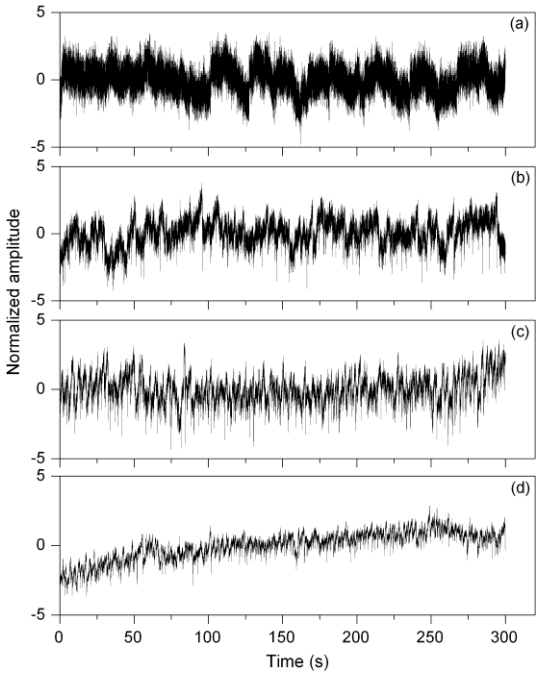

Figure 4.57. The normalized time series segments of potential noise with a record length of 300 s (the number of the discrete data points is 60 000) for chlorine evolution under galvanostatic polarization in 3.5 M NaCl, pH 3 at 50 ^{o}C at a current density of (a) 4 mA cm^{-2}, (b) 30 mA cm^{-2}, (c) 70 mA cm^{-2}, (d) 100 mA cm^{-2}.

Note that the above statistical analysis results could not provide any information about the periodicity of gas bubble evolution, although the periodic information is contained within the noise data. It is necessary to use more advanced and effective mathematical method and signal processing technique to extract the characteristic bubble evolution information.

The following sections demonstrate two widely used signal analysis methods: Fourier transform and wavelet transform.

4.4.3 Fourier analysis of potential fluctuations

Fourier transform (FT) is an operation that transforms the signal from the time domain into the frequency domain. The time series of potential signal can be represented in the frequency domain by a Fourier power spectral density function (PSD). The PSD describes how the power per unit of frequency (spectral) of a time series is distributed with the frequency. The typical PSD units for the potential noise signals are $mV^2\ Hz^{-1}$. The value [Hz^{-1}] refers to a bandwidth rather than to the frequency in Hz along the *x*-axis. The integral of the PSD over a given frequency band calculates the average power in the signal over that frequency band. Note that the peaks in the Fourier PSD spectra do not reflect the power at a given frequency. The popular way to estimate the PSD is based on the computation of the squared modulus of the Fourier transform of the time series through fast Fourier transform (FFT), which requires the zero-padding of the time series to a length of an integer power of 2.

The characteristic parameters of bubble evolution, such as the detachment diameter, frequency and population density, have been derived from the theoretical models based on the Fourier power spectra of the electrochemical noise data [157,162,163]. The plateau-$f^{-\alpha}$ roll-off profiles of PSD, where α is power-law slope, can be used to separate various factors associated with the fluctuation in electrochemical signals, and to estimate quantitatively the characteristic parameters of bubble evolution by fitting the profiles to theoretical equations. However, in the cases of overlapped PSD curves or the absence of frequency-localized plateau and peaks in PSD curves [164,165], the Fourier PSD is incapable of providing further information.

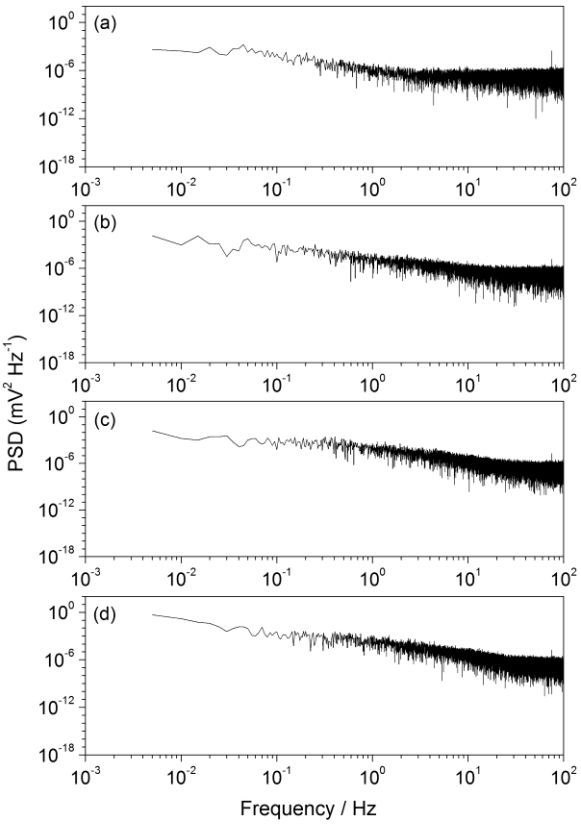

Figure 4.58. Fourier power spectral densities (PSD) of potential noise data corresponding to Figure 4.57 at the current density of (a) 4 mA cm^{-2}, (b) 30 mA cm^{-2}, (c) 70 mA cm^{-2}, (d) 100 mA cm^{-2}.

Fourier PSD plots of potential noise recorded at different current densities are shown in Figure 4.58. Although there are obvious differences in noise time series profiles (Figure 4.57), it is impossible to distinguish the noise series by the PSD curves due to the extreme similarity of Figure 4.58 a-d, since the PSD analysis is based on the perfectly distinguishable PSD profiles among different noise data. The PSD analysis obscures the important underlying information of bubble evolution in this case. In addition, some restrictions of PSD in the analysis of noise data have also been emphasized in cases of impulse or drift signals [65]. As a matter of fact, non-stationary signals, which dissatisfy the fundamental assumptions of Fourier analysis [166], could appear in bubble evolution process for practical electrolysis.

4.4.4 Wavelet analysis of potential fluctuations

Accurate feature extraction of the periodicity from the chaotic time series can provide characteristic correspondence of bubble behaviour. As a powerful alternative to Fourier transform, wavelet transform (WT) has been utilized widely in the field of analytical chemistry such as spectroscopy, chromatography and electroanalytical signals [167]. By the convolution operation of the input data sequence with a scaled wavelet function, WT possesses the capability to visualize the frequency contents localized in time of a signal. In this section, a straightforward analysis strategy based on wavelet analysis of potential noise data has been presented to identify the characteristic Cl_2 bubble evolution behaviour when Fourier analysis is proven to be helpless.

The normalized complex Morlet wavelet function (a product of a complex exponential wave and a Gaussian envelope, $\pi^{-1/4}$ is a normalization factor) [168] is given by:

$$\psi_0(t) = \pi^{-1/4} \exp(i\omega_0 t) \exp(-t^2/2) \tag{4.9}$$

where ψ_0 is the wavelet value at the non-dimensional time t (Figure 4.59), and $\omega_0 = 6$ is a non-dimensional parameter, was used to calculate the local wavelet power spectra using algorithm proposed by Torrence and Compo [169].

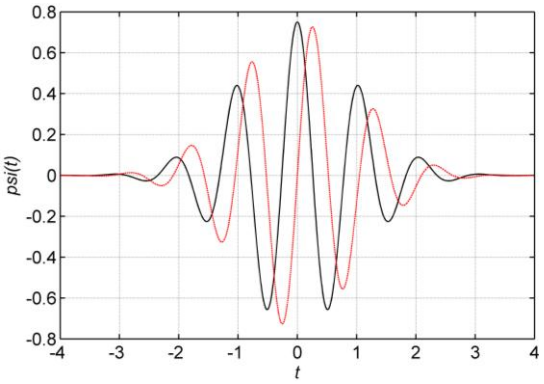

Figure 4.59. Complex Morlet wavelet base function (Eq. (4.9)) in the time domain with the wave-like oscillation. Real part (black curve) and imaginary part (red curve).

The relation between the equivalent Fourier periods (p) and wavelet scales (s) for Morlet wavelet is given by:

$$p = \frac{4\pi s}{\omega_0 + \sqrt{2 + \omega_0^2}} = 1.033s\,. \tag{4.10}$$

Significance test against red noise background spectra under null hypothesis for the wavelet power spectra was conducted to identify the physically meaningful components of the potential fluctuations [169]. The global wavelet power spectra were calculated by the statistical average of the wavelet power spectrum over time [170], excluding the data points within the cone-of-influence due to the edge-effects for a time series with truncated boundaries. It should be stressed that the global wavelet spectrum is the biased estimator of the true signal power $P(f)$, rather than the original signal amplitude $|\Delta V(t)|$. To correlate approximately the potential amplitude with the dominant periodic events, the power peaks in the global wavelet power spectra were modulated by $\sqrt{P(f)\Delta f}$, where $\Delta f = 1/s\sqrt{2}$ is the frequency bandwidth [168,171,172].

The one-dimensional time series were depicted into two-dimensional time-period local wavelet power spectra (left column in Figure 4.60) by performing WT, which visualizes the periodic contents of bubble evolution and simultaneously how the periodic contents evolve over time. The extracted features were highlighted from wavelet power contours by computing the local maxima of squared modulus of the wavelet coefficients. The cross-hatched regions mark out the cone-of-influence caused by edge effects. The right column in Figure 4.60 shows the global wavelet power spectrum (black curves), along with the 5% significance levels (red dashed curves).

Note that for the present time series and the type of wavelet used, the maximal reliable period ($p_{\max}$) to satisfy the wavelet detection criterion is 73 s, given by [173]:

$$p_{\max} = \frac{1.033T}{3\sqrt{2}}\,, \tag{4.11}$$

where $T = N \cdot \Delta t = 300$ s is the total sampling time of the time series segment, $N = 60\,000$ is the number of the sampled data points in the time series segment, $\Delta t = 5$ ms is sampling interval. Therefore, some peaks exceeding the 73 s limit have to be rejected before

considering the bubble behaviour. Experimentally, the artefacts of long-period contents could be attributed to the assembly and detachment of bubbles at the electrode border [157].

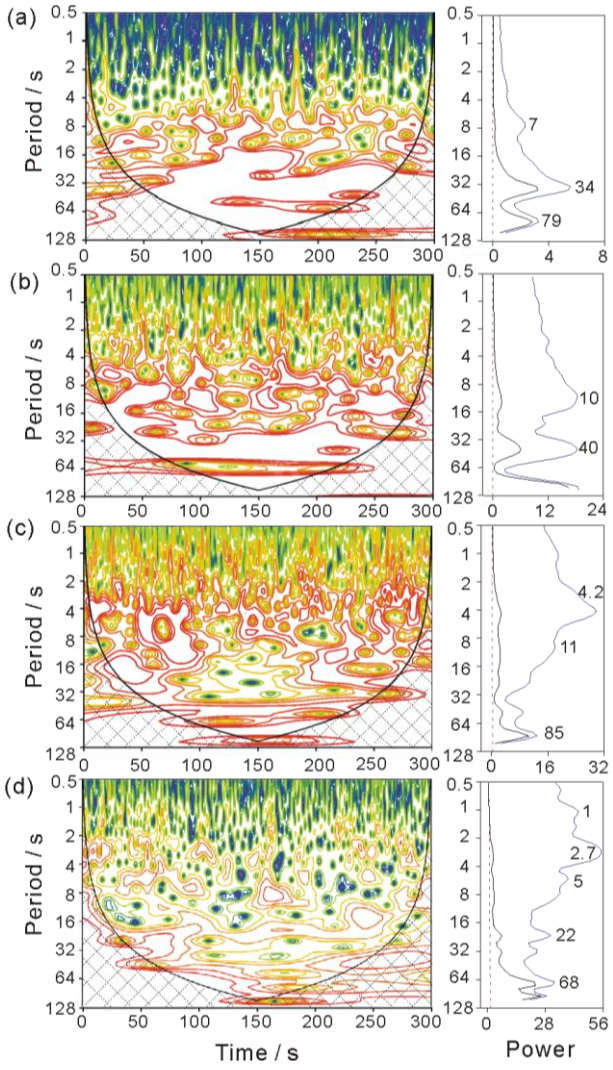

Figure 4.60. (left column) Local wavelet power spectra (the noise power increases from dark blue contours to red contours) corresponding to time series in Figure 4.57 at the current density of (a) 4 mA cm^{-2}, (b) 30 mA cm^{-2}, (c) 70 mA cm^{-2}, (d) 100 mA cm^{-2}. Cross-hatched regions define the cone-of-influence. (right column) The corresponding global wavelet power spectra (black solid curves) along with 5% significance levels (red dashed curves), and modulated global wavelet power amplitude spectra (blue solid curves, shown on relative scales).

As observed from the peaks in the global wavelet power spectra (black curves, right column in Figure 4.60), several time patterns were well resolved corresponding to each applied current density, indicating that bubble evolution is characterized by multi-period events. This reflects the electrocatalytical and morphological heterogeneities of the discrete nucleation sites and electrode surface. In contrast, simulations from the PSD profiles usually return a single value of bubble release frequency for a given current density [174], which should be applied restrictively to the cases of perfectly uniform electrodes. WT is superior to Fourier analysis to reflect the reality in this respect. At smaller wavelet scales the events with periods less than 1 s were captured from the potential fluctuations and the resulting wavelet power peaks were below the 5% significance level. At higher *j*, the peaks attributed to short-period events of 2~4 s become distinct implying the increased release frequency of bubbles.

The WT yields a wide frequency bandwidth ($\Delta f = 1/s\sqrt{2} = 1.033/p\sqrt{2}$) in the higher frequency regions and accordingly the wavelet power peaks get smoothed out. By modulating the true potential fluctuations power by $\sqrt{P(f)\Delta f}$, the relative amplitudes of the high-frequency (short-period) components of bubble evolution were amplified (blue curves, right column in Figure 4.60). Approximately, the modulated peak amplitudes represent the contribution of different periodic events to the total σ of potential fluctuations [172]. Thus the dominant characteristic periodic components causing the actual potential fluctuations $|\Delta V(t)|$ at gas-evolving electrodes can be well resolved. A linear relationship of dominant bubble characteristic frequency $f_c = 1/p$ with applied *j* was obtained (Figure 4.61). Considering the frequency localization is more precise at large scale of wavelet analysis, the value of data points at low *j* is more accurate in Figure 4.61.

Theoretically, a limiting current density (j_{lim}) corresponding to the initial bubble nucleation can be obtained from the intercept on horizontal axis (Figure 4.61), which is related to the electrode properties controlling the gas-evolving behaviour. A value of $j_{lim} = 1.04$ mA cm^{-2} for the present electrode was obtained roughly using wavelet analysis of the noise data mathematically. Similar values were found for H_2 and O_2 evolution [175,176]. Below this threshold, the removal of product molecules proceeds through diffusion into bulk solution rather than through gas evolution. Wavelet analysis of potential fluctuations time series for $j = 1$ mA cm^{-2} proves that periodic events are absent and wavelet power peaks are below

the 5% significance level, indicating a purely random process and confirming the bubble-free presumption when $j < j_{lim}$. The j_{lim} is an important identifier of gas-evolving electrodes and often difficult to be determined by traditional analysis [175].

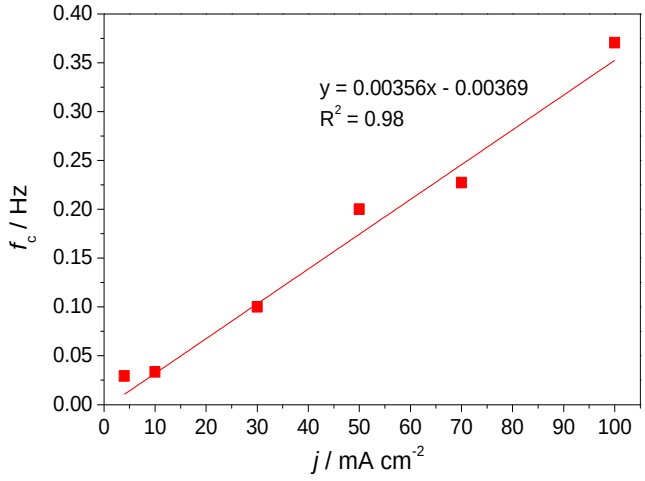

Figure 4.61. Dominant characteristic frequency (f_c) of bubble evolution resolved from the modulated global wavelet power amplitude spectra as a function of applied current density.

Fourier transform contains no information about the time evolution of the spectra. In contrast, local wavelet power spectra reveal not only the frequency contents but also their time localization. The transitions of bubble evolution events can be observed from the time history of wavelet power. The discontinuity of certain frequency contents over the whole time record implies that the time series of potential fluctuations are not strictly wide-sense stationary signals [166]. The time spans of the dominant events along time axis (local wavelet power spectra in Figure 4.60) shortened with the increase of j. At low j the broad time spans were observed as evidence of anchored bubble growth and coalescence events for a longer time until substantial buoyancy force raises the bubbles up. Compared to bubble departure, although bubble coalescence imposes weaker influence on the electrode surface shadowing [162], it exerts a pronounced effect on micro-convection and current distribution. For an electrode easily wetted by electrolyte, the formed bubbles are prone to detach rather than coalescence. This provides a feasible way for in-situ evaluation of the wettability of different electrodes by comparing the bubble coalescence behaviour. Much

finer separation of contours in the local wavelet power spectra at j = 100 mA cm^{-2} implies that short-time and numerous bubbles release is the dominant characters and the bubble coalescence effects fade away.

This section demonstrates and validates the methodology for the identification of bubble evolution behaviour using wavelet analysis of potential fluctuations data. The obtained results confirm that the abundant and valuable information hidden in the noise data can be easily extracted using wavelet transform, which is independent of theoretical models or visual observations. The local detailed behaviour and global behaviour of bubble evolution can be visualized from the time-frequency localization. A more realistic evaluation of bubble behaviour on any arbitrary electrode geometry can be actualized using the proposed analytical method. The analytical resolution and sensitivity of potential signals can be further improved by optimal selection of wavelet basis function and algorithm. Further investigation to compare the electrode morphology and structure dependent gas bubble evolution behaviour is necessary to guide the controlled coating preparation technique.

4.4.5 Influence of electrolysis temperature on the bubble evolution behaviour

Electrolysis temperature is one of the most critical parameters to maximize the electrolysis efficiency for the electrolytic chlorine production processes. For the anodic reaction: $2Cl^- \rightarrow Cl_2 + 2e^-$, the theoretical electrochemical equilibrium potential, E_e, ($E_e = E^0_{cl^-/Cl_2} + \frac{RT}{2F}\ln\frac{p_{Cl_2}}{\left(\alpha_{Cl^-}\right)^2}$) decreases with the increase of electrolysis temperature, T. (The argument of the logarithm is negative in the equation.) Meanwhile, the electrolysis temperature imposes an influence on the bubble-induced potential fluctuations, as shown in Figure 4.62. Lower amplitudes of potential noise were observed at higher electrolysis temperatures. Above 50 ^{o}C, the influence of electrolysis temperature on the amplitude of the potential fluctuations was negligible (Figure 4.62). The influence of electrolysis

temperature on the potential fluctuations is evident at higher applied current densities, in which region the bubble evolution is intensive.

H. Vogt qualitatively summarized the influence of electrolysis temperature on the anode effects [163]: Increasing electrolysis temperature can increase the diffusion coefficient of dissolved gas, enhance the mass transfer, lower the bubble population density, and change the wettability of electrode coatings. Bubbles easily detach away from the electrode surface and with larger bubble diameter at higher electrolysis temperatures. The rate of heterogeneous bubble nucleation is a function of electrolysis temperature and contact angle [177]. Note that the dependence of bubble behaviour on the electrolytic conditions for H_2, O_2, Cl_2 is different. A direct comparison of bubble behaviour with reported results for different gases in the electrolytic system does not make sense.

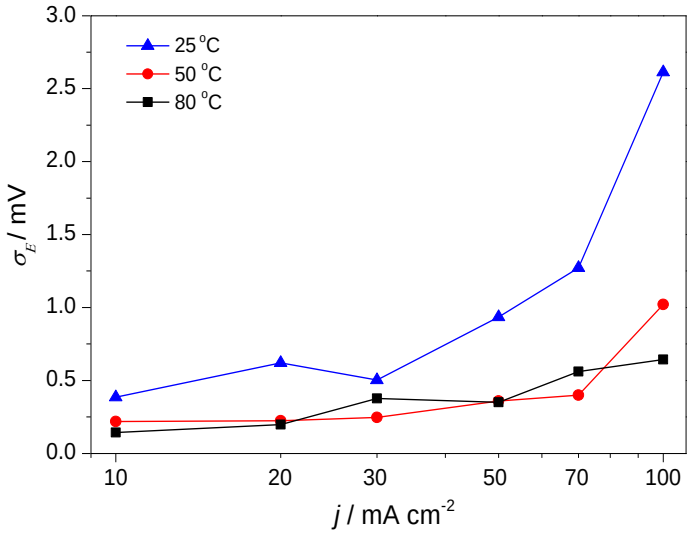

Figure 4.62. Standard deviation of potential fluctuations (σ_E) as a function of the applied current density on a logarithmic scale, and as a function of the electrolysis temperature: (▲) 25 °C, (●) 50 °C, (■) 80 °C. Steady-state current-potential curves for chlorine evolution reactions measured galvanostatically in 3.5 M NaCl, pH 3, with forced convection of electrolyte (volumetric flow rate of electrolyte: 100 mL min^{-1}) for the electrode coating $Ru_{0.25}Ti_{0.65}V_{0.1}O_x$ (see: Section 4.4.1).

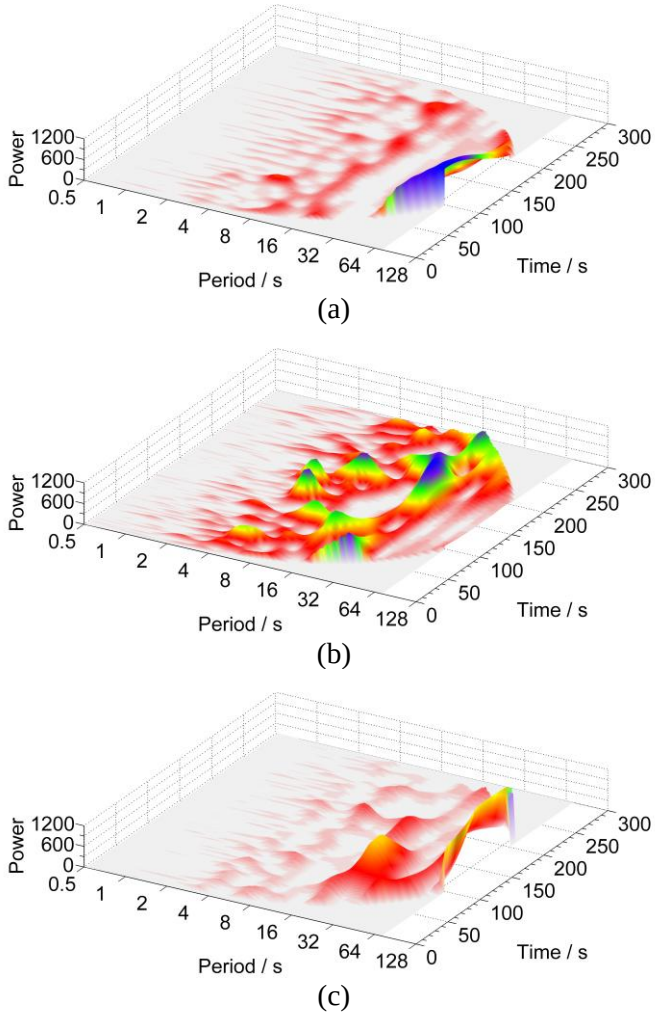

Figure 4.63. Local wavelet power spectra show the influence of electrolysis temperature on the bubble detachment period for the electrode coating $Ru_{0.25}Ti_{0.65}V_{0.1}O_x$ (see: Section 4.4.1). The potential noise data points were recorded in 3.5 M NaCl, pH 3, at a current density of 0.5 kA m^{-2}, at the electrolysis temperature of (a) 25 ^{o}C, (b) 50 ^{o}C and (c) 80 ^{o}C.

The dependence of bubble evolution behaviour on the electrolysis temperature was investigated by performing wavelet transform of the recorded potential fluctuation signals. The local wavelet power spectra (i.e., the three-dimensional time-period-wavelet power plots) and the modulated global wavelet power spectra (which reflects the real contribution of the frequency components to the total fluctuations of the potential noise signal) for the potential noise were shown in Figure 4.63 and Figure 4.64, respectively.

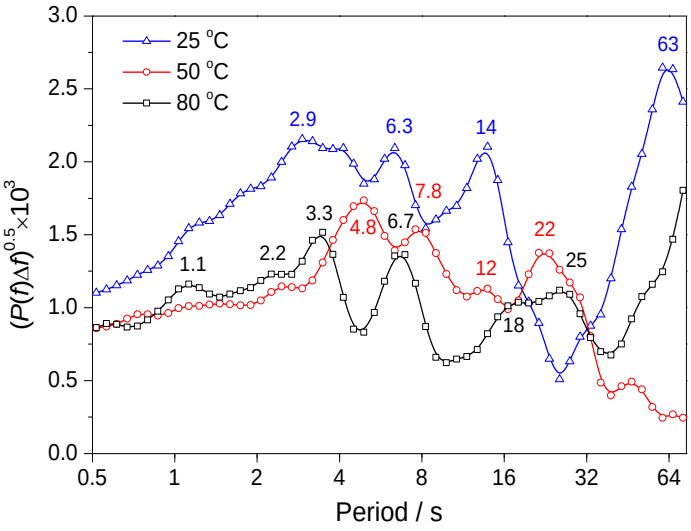

Figure 4.64. Modulated global wavelet power spectra corresponding to the local wavelet power spectra in Figure 4.63. The potential noise data points were recorded in 3.5 M NaCl, pH 3, at a current density of 0.5 kA m^{-2}, at the electrolysis temperature of (Δ) 25 °C, (○) 50 °C and (□) 80 °C.

The time-period localized wavelet power ridges (i.e., the local maximum of the wavelet power) observed in the local wavelet power spectra (Figure 4.63) show the frequency components (i.e., frequency- or period-localized characteristic of wavelet transform) of bubble evolution events and meanwhile when they occur (i.e., time-localized characteristic of wavelet transform). Short-period bubble evolution events become dominant at higher electrolysis temperatures (Figure 4.63, Figure 4.64). The 3.3- and 6.7-second periodic events observed at the electrolysis temperature of 80 °C (Figure 4.63c) frequently occur at certain intervals over the 300-second time-record. The 25-second periodic events happen only once during the 300-second time-record (Figure 4.63c). The analysis of the amplitude of the peaks in the modulated global wavelet power spectra (Figure 4.64) must be done carefully in the presence of the fortuitous events (such as the 25-second periodic events in Figure 4.63c). The relative amplitude of the period-peaks in the modulated global wavelet power spectra (Figure 4.64) approximately represents the relative contribution of the period-components to the total amplitude of the potential fluctuations. Thus the highest period-peak in the modulated global wavelet power spectra corresponds to dominant bubble evolution events causing the potential fluctuations.

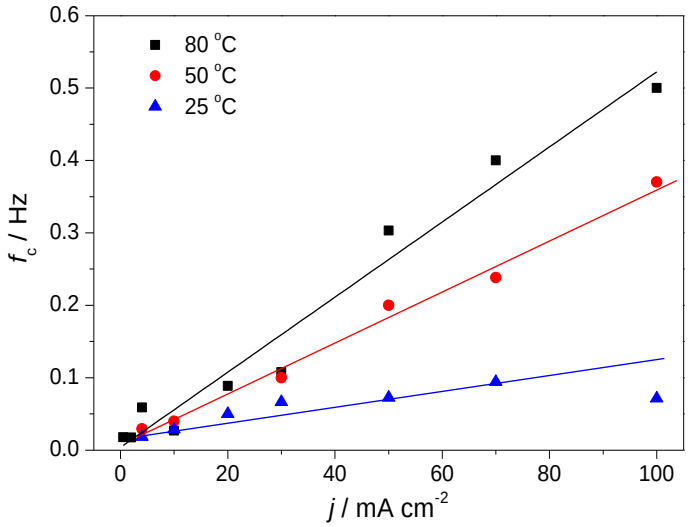

Figure 4.65. Dominant characteristic frequency (f_c) of bubble evolution resolved from the modulated global wavelet power amplitude spectra as a function of applied current density and electrolysis temperature: (▲) 25 °C, (●) 50 °C and (■) 80 °C.

The resolved dominant characteristic bubble evolution frequency (f_c) as a function of current density and electrolysis temperature was shown in Figure 4.65. A linear dependence of the f_c on the current density was observed at each electrolysis temperature. The difference in the slope of the fitting lines implies the different bubble detachment rates under various electrolysis temperature conditions. High temperature electrolysis accelerates the detachment of the chlorine bubble. The limiting current densities (j_{lim}) corresponding to the initial bubble nucleation at different electrolysis temperatures, obtained from the intercept of the fitting line on horizontal axis in Figure 4.65, are roughly equal.

4.4.6 Case analysis: Bubble evolution behaviour for the commercial electrode and sol-gel $Ru_{0.3}Sn_{0.7}O_2$ electrode coatings

In this section, the bubble evolution behaviour for a very active $Ru_{0.3}Sn_{0.7}O_2$ electrocatalyst coating prepared by the sol-gel route (see Section 3.1.4, ruthenium metal loading amount was 7.7 g m^{-2}) was analyzed based on the potential noise data. A commercial $Ru_{0.3}Ti_{0.7}O_2$/Ti electrode, with a ruthenium metal loading amount of 12.1 g m^{-2} prepared by thermal decomposition technique, was used for a comparative investigation. The titanium supported $Ru_{0.3}Ti_{0.7}O_2$ and sol-gel derived $Ru_{0.3}Sn_{0.7}O_2$ electrocatalyst coatings were prepared by using the similar procedure of coating/drying/sintering cycles. Accordingly, the typical mud-crack surface structures were observed for both electrode coatings and the crack gaps in the commercial coating were broader than that in the sol-gel $Ru_{0.3}Sn_{0.7}O_2$ coating (Figure 4.66).

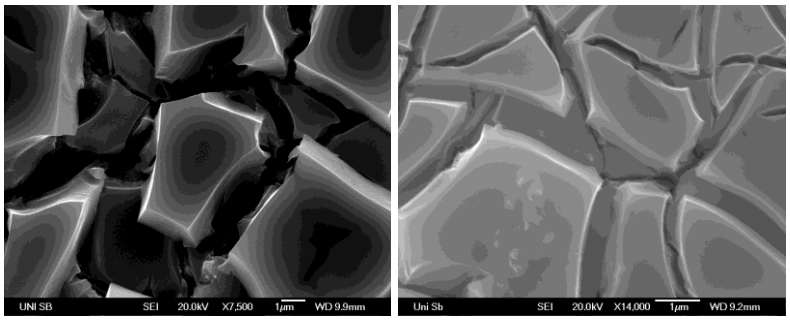

Figure 4.66. SEM images of commercial $Ru_{0.3}Ti_{0.7}O_2$ and sol-gel $Ru_{0.3}Sn_{0.7}O_2$ coatings show the typical mud-crack surface morphologies.

The electrocatalytic activity toward the chlorine evolution reactions of the as-obtained sol-gel $Ru_{0.3}Sn_{0.7}O_2$ coating and the commercial $Ru_{0.3}Ti_{0.7}O_2$ electrode coating were evaluated by steady state chronopotentiometric measurements in 3.5 M NaCl, pH 3 at 80 ^{o}C with the applied current density stepping from 0.04 to 4 kA m^{-2}. The potential fluctuation data

points were recorded using the same way as described in Section 4.4.1. The electrocatalytic activity of the commercial $Ru_{0.3}Ti_{0.7}O_2$ electrode coating and sol-gel $Ru_{0.3}Sn_{0.7}O_2$ coating for chlorine evolution reactions was compared in Figure 4.67. At the applied current density of 4 kA m^{-2}, the sol-gel $Ru_{0.3}Sn_{0.7}O_2$ coating shifts down the electrode potential around 60 mV compared to the commercial $Ru_{0.3}Ti_{0.7}O_2$ electrode coating, although the sol-gel $Ru_{0.3}Sn_{0.7}O_2$ coating contains less ruthenium loading amount (7.7 g Ru m^{-2}) than the commercial coating (12.1 g Ru m^{-2}). As shown in the inset in Figure 4.67, the standard deviation of the potential noise (σ_E) linearly increases with log$j$ for the sol-gel $Ru_{0.3}Sn_{0.7}O_2$ coating, whereas for the commercial electrode the σ_E increases slowly form 0.04 to 1 kA m^{-2}, and then increases sharply from 1 to 4 kA m^{-2}.

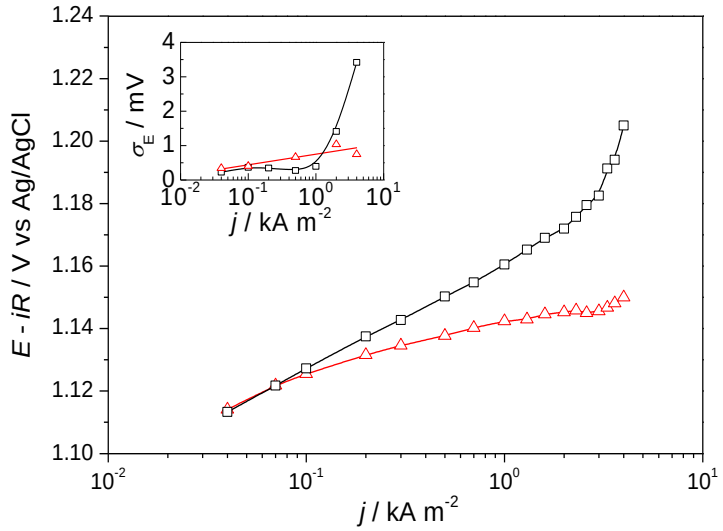

Figure 4.67. Steady-state current-potential curves for chlorine evolution reactions measured galvanostatically in 3.5 M NaCl, pH 3, at 80 °C, with forced convection of electrolyte for (□) commercial $Ru_{0.3}Ti_{0.7}O_2$ electrode coating, (Δ) sol-gel $Ru_{0.3}Sn_{0.7}O_2$ electrode coating. Mean potential values were corrected for the electrolyte ohmic resistance (*E*-*iR*). Inset shows the standard deviation of potential fluctuations (σ_E) as a function of current density.

Oscillating gas bubbles impose significant influence on the mixing hydrodynamics and mass transfer in the electrolysis system. Except for the factor of bubble detachment rate,

increase either in bubble size or in bubble population density can result in large fluctuations in the electrode potential signals. Quantitative study of various factors contributed to the chaos of electrolysis system is necessary to improve design of electrode coatings.

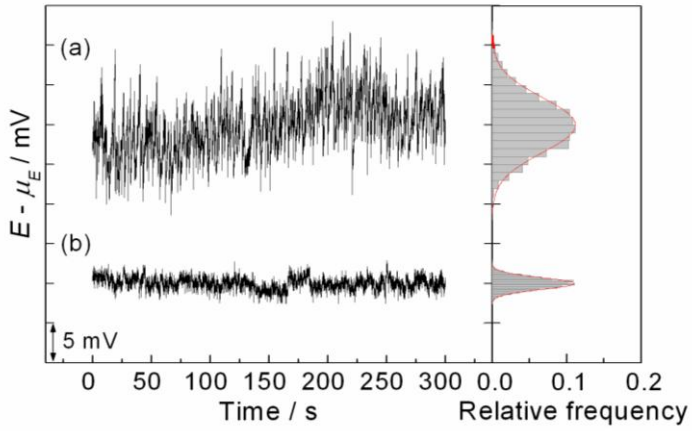

Figure 4.68. Chronopotentiometric response of electrodes (the mean values μ_E were removed) (a) commercial electrode, (b) sol-gel $Ru_{0.3}Sn_{0.7}O_2$ electrode coating in 3.5 M NaCl (pH 3) at 80 ^oC and polarized at 4 kA m^{-2}. A time series segment of 300 s was chosen from the chronopotentiometry measurements (sampling frequency: 200 Hz) for the statistical analysis. Right column shows the corresponding histograms of potential noise data fitted with a normal distribution (red curves).

The representative potential fluctuation noise recorded galvanostatically at 4 kA m^{-2} for the commercial coating and sol-gel derived coating was shown in Figure 4.68. The noise amplitude is about four times larger for the commercial coating than that for the sol-gel coating, suggesting a more chaotic bubble evolution process at the electrode/electrolyte interface for the former. The potential noise obeys a normal distribution law for both coatings. It has been proposed that the amplitude of the potential noise is associated with the bubble diameter [162]. Thus larger bubbles could be generated at the commercial coating than that at the sol-gel coating. The bubble evolution behaviour could be governed by the local activity, the distribution and spacing of the active sites at the electrode surface. The characteristics of bubble evolution events at the electrode surface were identified by the electrochemical noise analysis technique, as shown in Figure 4.69 and Figure 4.70.

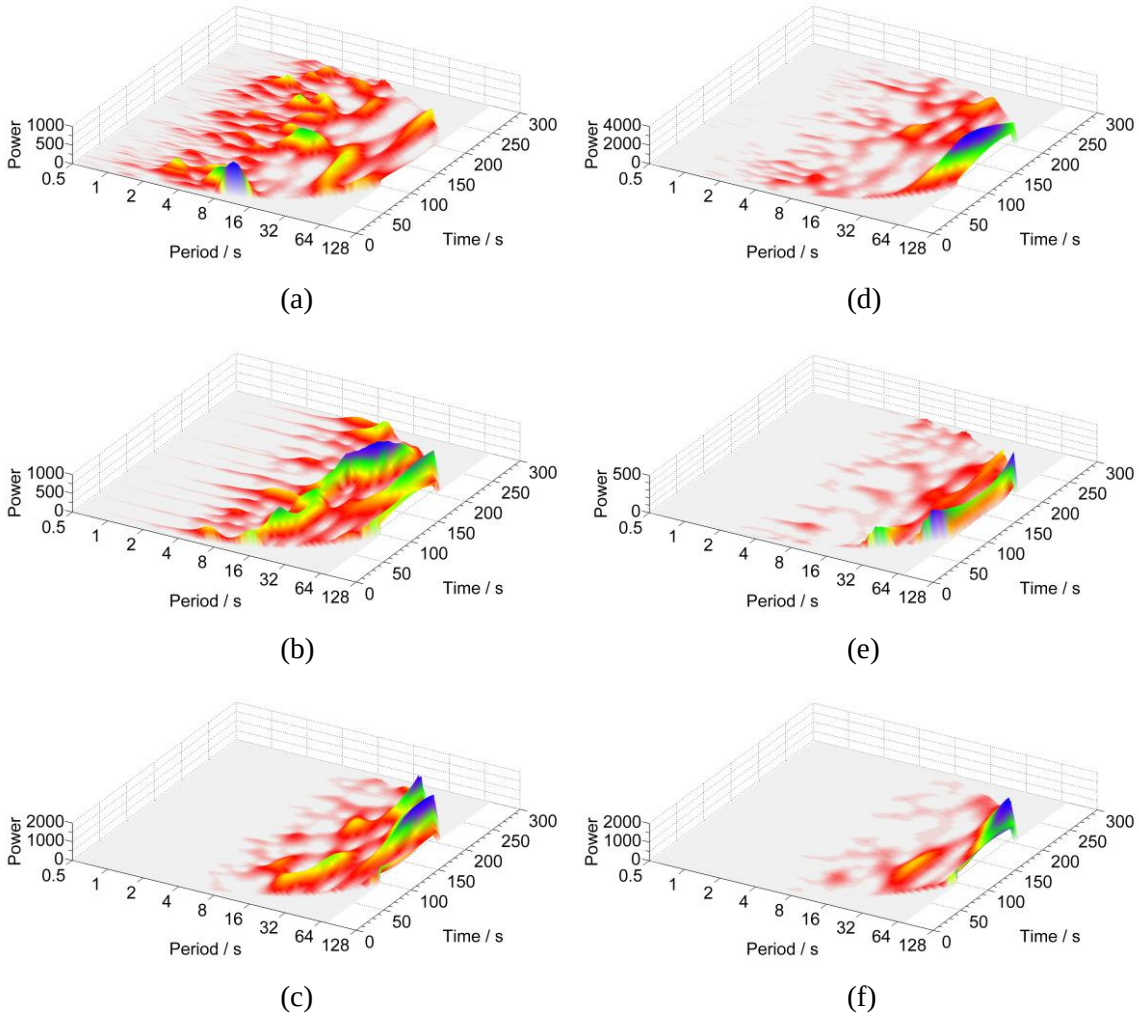

Figure 4.69. Local wavelet power spectra (three-dimensional time-period-wavelet power plots) of potential noise for the (a,b,c) commercial electrode, and (d,e,f) sol-gel $Ru_{0.3}Sn_{0.7}O_2$ electrode coating. The potential noise data were recorded in 3.5 M NaCl, pH 3, at 80 ^{o}C at a current density of (a,d) 4, (b,e) 0.5, (c,f) 0.04 kA m^{-2}.

The short-periodic bubble evolution events become evident at higher applied current densities. For the commercial electrode galvanostatically polarized at 4 kA m^{-2}, the bubble evolution induced larger potential fluctuations (Figure 4.68a). The potential fluctuations in Figure 4.68a were caused by four resolved periodic-components (or frequency-components): 2.6, 7, 14 and 31 s (Figure 4.70). The amplitudes of the wavelet power ridges for the short-periodic events (2~16 s) were comparable to those for the long-periodic events (16~64 s), as observed from Figure 4.69a. This indicates that the short-periodic events contribute more to the total amplitude of the potential fluctuations than the long-

periodic events. The quantitative analysis was shown in the modulated wavelet power spectra (i.e., the $(P(f)\cdot\Delta f)^{0.5}$ vs. period plots, top in Figure 4.70), since the standard deviations of the potential fluctuations (σ_E) were approximately proportional to the $P(f)\cdot\Delta f)^{0.5}$ [172]. Therefore, the 2.6- and 7-s periodic events contribute around two times larger to the amplitudes of the potential fluctuations (Figure 4.68a) than the 14- and 31-s periodic events. In comparison with the sol-gel $Ru_{0.3}Sn_{0.7}O_2$ coating, the 4, 8, 16, and 26 s periodic events (red lines, top in Figure 4.70) contribute equally to the amplitudes of the potential fluctuations (Figure 4.68b).

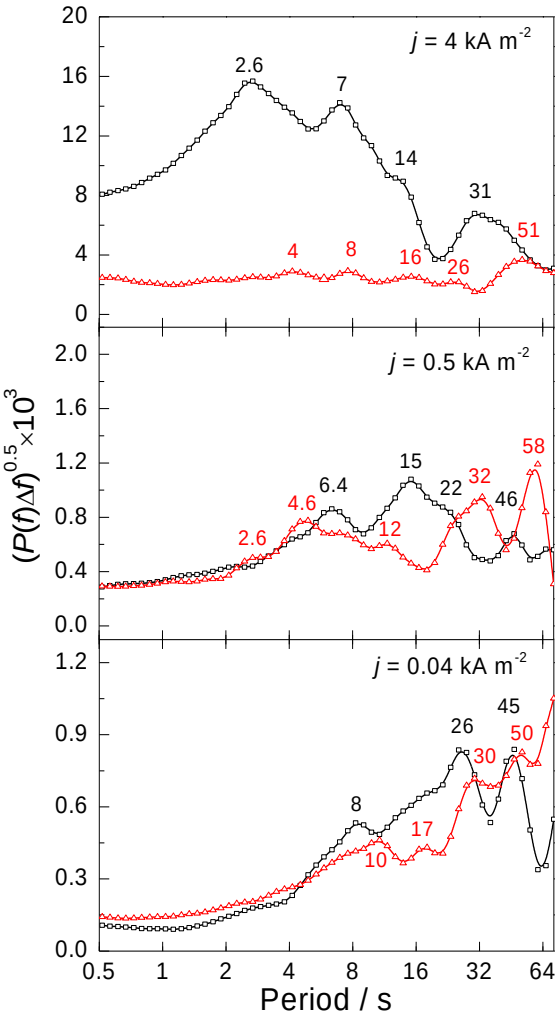

Figure 4.70. Modulated global wavelet power spectra for the (□) commercial electrode and (Δ) sol-gel $Ru_{0.3}Sn_{0.7}O_2$ electrode coating.

Interestingly, the relative contribution of the periodic events to the amplitudes of potential fluctuations changes with the applied current density, as shown in Figure 4.70. For the commercial electrode, the dominant periodic events causing the potential fluctuations change from 45-s at 0.04 kA m^{-2} to 15-s at 0.5 kA m^{-2}, and then to 2.6-s at 4 kA m^{-2} (black curves in Figure 4.70). For the sol-gel $Ru_{0.3}Sn_{0.7}O_2$ coating, the similar phenomena were only observed at current density from 0.04 to 0.5 kA m^{-2}. The wettability of the oxide coatings could change with the electrolysis conditions (such as temperature and current density), which depends on the coating materials. This could be a reason for the different bubble evolution behaviour observed for the commercial and sol-gel coatings.

For the gas-evolving electrode, molecular chlorine is partially dissolved and diffuses into the bulk electrolyte, the rest exists as adhering bubbles at the electrode/electrolyte interface. The efficiency of gas evolution is defined as the ratio of gas bubble evolved at the electrode to the total amount of molecular chlorine generated. According to the Faraday's law, equivalent amount of chlorine was produced per unit time at both electrodes polarized at the same current density. Assuming that all of the chlorine produced exists as bubbles close to the electrode surface at the extraordinary high current density of j = 4 kA m^{-2} (i.e., the gas evolution efficiency is 100%), the total volume flux density of chlorine produced is

$$\frac{V_g}{At} = \frac{jRT}{zFp} = \frac{1}{At}\sum n_j v_{g,j} \,, \tag{4.12}$$

where A is the electrode surface area; t is the sampling duration of bubble events; R is gas constant; T is absolute electrolysis temperature; z = 2 is the number of electrons transferred for the electrode reaction; F is Faraday's constant; p is the gas pressure in the bubbles; n_j is the number of adhering bubbles with the volume of $v_{g,j}$. The total volume flux density of chlorine produced is 0.06 $cm^3cm^{-2}s^{-1}$ at j = 4 kA m^{-2}, 80 ^oC, $p \approx 1$ bar and assuming the gas evolution efficiency and the current efficiency are 100%. The bubble population density, buble volume, bubble coverage fraction etc. are important parameters for the systematic evaluation of the gas-evolving electrodes. The development of a mathematical model and the experimental observation of bubble evolution processes using video camera could be helpful to deduce the various parameters.

4.4.7 Conclusion

In this section chlorine bubble evolution behaviour at the electrode surface was identified by analyzing the bubble-induced electrochemical noise (electrode potential noise) using the mathematic analysis methods such as standard deviation, autocorrelation function, Fourier power spectral density and wavelet transform.

Bubble effects at the gas-evolving electrode cause additional ohmic drop due to the blocking and shielding effect of the electrode surface by the formed or anchored bubbles, which could depend on the surface morphology of the electrode coatings and the electrode materials. Identification of the bubble behaviour is necessary to assist the design of electrode structure and the selection of suitable electrode materials.

A statistical quantity such as the standard deviation of the electrochemical noise is able to establish the correlation between the noise intensity and the cell operation parameters, electrode materials, etc. However, for the electroanalytical signals with undesirable drift, the statistical analysis encounters the difficulty to provide reliable results.

The transformation of the signals from the time domain to the frequency domain using Fourier transform methods is expected to provide the frequency information of bubble evolution contained within the noisy signals. However, the Fourier transform is not able to distinguish the signals with similar features. As an alternative, the wavelet transform is capable of providing accurate time-frequency localization, which is used in this work to extract the characteristic frequency information of bubble evolution.

The dependence of the bubble evolution behaviour on the applied current density, and electrolysis temperature was investigated. A linear relationship between the dominant characteristic frequency of bubble evolution and the current density was observed. High temperature electrolysis accelerates the detachment of the chlorine bubble. A systematic and comparative analysis of the electrode activity, bubble induced noise, and bubble evolution behaviour for the commercial $Ru_{0.3}Ti_{0.7}O_2$ coating and sol-gel derived

$Ru_{0.3}Sn_{0.7}O_2$ coating was carried out. The periodic bubble evolution events causing the potential fluctuations were resolved from the wavelet analysis of potential noise data. The dominant periodic events contributing to the total amplitude of the potential noise (or the total standard deviation of the potential noise) have been analyzed by the modulated wavelet power spectra. Future work to develop a mathematical model is essential to deduce more valuable bubble parameters, such as the bubble population density, bubble size, bubble coverage fraction and gas evolution efficiency, etc.

5 Summary and conclusions

A multi-perspective investigation, including (i) the selection of electrocatalyst materials, (ii) the design of coating morphology, (iii) the modification of the phase structure and (iv) the identification of the bubble evolution behaviour, has been carried out in this work. The electrocatalytic performance of sol-gel derived oxide coatings has been optimized by choosing the chemical composition and by controlling the surface morphology. In order to avoid the underlying substrate passivation, a crack-free inner protective layer was fabricated purposely. A wavelet-based analytical strategy has been developed to identify the bubble effects for the electrochemical chlorine evolution reactions. The structural and electrochemical characterization was performed to disclose the material-structure-property correlations.

Based on the typical binary $Ru_xTi_{1-x}O_2$ oxide system, the multi-component system $RuTiMO_x$ have been prepared by using acetic acid and propionic acid catalyzed sol-gel routes to optimize the chemical composition-dependent electrocatalytic activity and to reduce the ruthenium content. It has been proven that the doping of vanadium and/or tin element(s) into the $RuTiO_2$ system is able to enhance significantly the electrocatalytic activity of oxide coatings compared to the binary $RuTiO_2$ system. Compared to the commercial electrode coating $Ru_{0.3}Ti_{0.7}O_2$, a reduction in the electrode potential (measured in 3.5 M NaCl, pH 3, with an applied current density of 100 mA cm^{-2}, i.e., 1 kA m^{-2}) by about 80 mV has been achieved for the sol-gel-derived oxide coatings with 15~30 mol% ruthenium. This indicates the possibility of a considerable reduction of the total electric energy consumption for the present industrial membrane process (cell voltage 3.1 V) of the electrolysis of NaCl aqueous solution or for the membrane process using an oxygen depolarized cathode.

It has been confirmed by other researchers that the electrode deactivation occurs before the complete dissolution of the active ruthenium components due to the formation of TiO_x interlayers between the substrate and the electrocatalyst layer by the penetration of

electrolyte through the cracky gaps of the oxide coatings. The crack-free oxide coatings (no visible cracks, gaps can be seen from SEM images) were prepared purposely by reduplicate dipping-withdrawing-drying-sintering steps with the intention to protect the underlying titanium substrates against passivation. The electrochemical cyclic voltammetry analysis shows that the obtained crack-free coatings have the impermeable characters for electrolyte. Thus the attack of the electrolyte on the titanium substrates can be avoided.

Nanopore-containing oxide coatings were prepared by using the lanthanum leaching technique in order to increase the active surface area of the oxide coatings. The utilization of the nanopores was investigated by electrochemical cyclic voltammetry and impedance spectroscopy. The charging behaviour of the nanopore-containing oxide coatings was studied by analyzing the charging curves recorded galvanostatically under slight polarization conditions. Further work to evaluate the dependence of the performance on the pore size, geometry and its gradient distribution is recommended.

Solvothermal processing of the xerogel oxide coatings has been demonstrated with the purpose to modify the phase structure of mixed $RuTiO_2$ oxide coatings. The solvothermal processing of the amorphous Ru-O-Ti xerogel coatings with subsequent thermal sintering treatment results in the formation of a mixed anatase/rutile structure with improved electrocatalytic activity for the chlorine evolution reactions. The structural and phase development of the xerogel coatings processed solvothermally were traced by using X-ray diffraction and Raman spectroscopy. It has been deduced that the unique structure, nanoparticles of rutile structure $Ru_xTi_{1-x}O_2$ (3 nm) decorating larger anatase TiO_2 particles (20 nm), is responsible for the enhanced electrocatalytic activity.

Bubble effects at the gas-evolving electrodes have been analyzed preliminaryly by performing wavelet transforms of the bubble-induced potential fluctuation signals. The Cl_2 gas bubble evolution at the electrode surface is characterized by multi-period events. The dominant characteristic frequency of bubble evolution as a function of the applied current density has been extracted out of the noisy signals. Further work is necessary to understand the interrelationship between materials, structure and morphology on the one hand and the bubble evolution behaviour on the other hand.

Appendix

A1. Chemicals

Description	**CAS No.**	**Molecular Formula**	**Molecular Weight / g mol^{-1}**	**Density / g mL^{-1}**	**Supplier**
4-Hydroxy-4-methyl-2-pentanone, 99%	123-42-2	$(CH_3)_2C(OH)CH_2COCH_3$	116.16	0.931	Sigma-Aldrich
Acetic acid	64-19-7	$C_2H_4O_2$	60.05	1.04	UdS*
Hydrochloric acid, 37%	7647-01-0	HCl	36.46	1.19	ABCR
Iridium (III) 2,4-pentanedionate, 99.9%	15635-87-7	$C_{15}H_{21}IrO_6$	489.5	-	ABCR
Isopropanol	67-63-0	C_3H_8O	60.10	0.785	UdS*
Lanthanum(III) nitrate hexahydrate; 99%[#]	10277-43-7	$La(NO_3)_3{\cdot}6H_2O$	433.01	-	ABCR
Oxalic acid dihydrate; 98%	6153-56-6	$C_2H_2O_4$	126.07	1.65	ABCR
Polyvinylpyrrolidone, average M.W. 58,000	9003-39-8	$(C_6H_9NO)_n$	-	-	Alfa Aesar
Propionic acid, 99+%	79-09-4	$CH_3CH_2CO_2H$	74.08	0.992	Alfa Aesar
Ruthenium (III) 2,4-pentanedionate	14284-93-6	$Ru(C_5H_7O_2)_3$	398.40	-	Alfa Aesar
Ruthenium (III) chloride hydrate (36%Ru), 99.9%[#]	14898-67-0	$RuCl_3$	207.43	-	ABCR
Tin(IV) isopropoxide isopropanol adduct, 98% (metals basis)[#]	132951-93-0	$Sn[OCH(CH_3)_2]_4.C_3H_7OH$	415.15	-	Alfa Aesar
Titanium (IV) isoproxide, 97%[#]	546-68-9	$Ti[OCH(CH_3)_2]_4$	284.22	0.96	Sigma-Aldrich
Vanadium (IV) oxide bis (2,4-pentanedionate)	3153-26-2	$C_{10}H_{14}O_5V$	265.16	-	ABCR
Zirconium (IV) n-propoxide, 70%w/w in n-propanol[#]	23519-77-9	$Zr[O(CH_2)_2CH_3]_4$	327.56	1.044	Alfa Aesar

[#] Moisture sensitive; * Zentrales Chemikalienlager der UdS.

A2. Software

Programme, Version	**Manufacturer**
CorelDRAW 10	Corel Corporation (Ottawa, Canada)
EC-Lab V9.95	Bio-Logic SAS (Claix, France)
MATLAB 7.0	The MathWorks, Inc. (Massachusetts, USA)
OriginPro 8.1	OriginLab Corporation (Northampton, USA)
ZSimpWin 3.10	EChem Software (Michigan, USA)

A3. List of abbreviations, Nomenclature

Abbreviation	Description
ACF	Autocorrelation function
AFM	Atomic force microscopy
BDD	Boron-doped diamond
CD	Chemical desorption
CP	Chronopotentiometry
cus	Coordinatively unsaturated surface sites
CV	Cyclic voltammetry
DSA	Dimensionally stable anode
DSC	Differential scanning calorimetry
ED	Electrochemical desorption
EDS	Energy dispersive X-ray spectroscopy
EIS	Electrochemical impedance spectroscopy
FT	Fourier transform
FTIR	Fourier transform infrared spectroscopy
HEC	Hydrogen evolving cathode
HT-XRD	High temperature X-ray diffraction
IS	Impedance spectroscopy
ODC	Oxygen depolarized cathode
PSD	Power spectral density
PVP	Poly(vinylpyrrolidone)
SEM	Scanning electron microscope
StDev	Standard deviation
TEM	Transmission electron microscope
TG	Thermogravimetry
WT	Wavelet transform
XRD	X-ray diffraction

A4. The calculation of energy consumption for chlorine production

For the industrial electrolytic chlorine (Cl_2, 71 g mol^{-1}) production from NaCl aqueous solution, Cl^- is oxidized by the loss of electron to the anode: $Cl^- \rightarrow \frac{1}{2}Cl_2 \uparrow + e^-$. The driving force for the electrode reaction is provided by applying a cell voltage, for instance 3.1 V. Assume the chlorine current efficiency is 98%. Then for the production of 1 ton Cl_2, the energy consumption is calculated as follows.

The molar number of the electron transfer is:

$$\mathrm{M}_{e^-} = \frac{1000\ \text{kg}/0.98}{1\text{ton}} \times \frac{1000\ \text{g}}{1\text{kg}} \times \frac{1\ \text{mol e}^-}{35.45\ \text{g}} = \frac{28784.43\ \text{mol}\ e^-}{\text{ton of chlorine}}$$

The amount of charge transfer is calculated according to the Faraday's law:

$$\begin{aligned}
&\mathrm{M}_{e^-} \times \text{Avogadro number} \times \text{charge of an electron} \\
&= \frac{28784.43\ \text{mol}\ e^-}{\text{ton of chlorine}} \times 6.022137 \times 10^{23}\,\text{mol}^{-1} \times 1.602177 \times 10^{-19}\,\text{C} \\
&= \frac{28784.43\ \text{mol}\ e^-}{\text{ton of chlorine}} \times 96485.31\ \text{C mol}^{-1} \\
&= \frac{2.77727 \times 10^9\ \text{C}}{\text{ton of chlorine}}
\end{aligned}$$

The energy consumption (kWh) for the production of 1 ton Cl_2 is:

$$\frac{2.77727 \times 10^9\ \text{C}}{\text{ton of chlorine}} \times 3.1\ \text{V} = \frac{8.60954 \times 10^9\ \text{J}}{\text{ton of chlorine}} = \frac{2.392 \times 10^3\ \text{kWh}}{\text{ton of chlorine}}$$

(The energy per unit charge is the potential difference: 1V = 1J C^{-1}.
1 kWh = 1000A × 1V ×3600s = 1000 C s^{-1} × 1V ×3600s = 3.6×10^6 CV = 3.6×10^6 J.)

A5. Peng-Robinson and van der Waals equations of state

The equation of state is a thermodynamic equation describing the state of matter under a given set of physical conditions (such as temperature, pressure, volume). Cubic equations of state are widely used in chemical engineering practice for the calculation and prediction of the properties of fluids or their mixtures. The van der Waals equation of state ($p = \frac{RT}{V_m - b} - \frac{a}{V_m^{\,2}}$, $a = \frac{27\left(RT_c\right)^2}{64 p_c}$ and $b = \frac{RT_c}{8 p_c}$, 1873) is developed based on the modification of the ideal gas law ($PV_m = RT$). However, it has limited accuracy for the prediction of properties of compressed fluids. Other equations of state have been developed on the basis of the van der Waals equation of state, such as Redlich-Kwong equation of state ($p = \frac{RT}{V_m - b} - \frac{a}{T^{1/2} V_m \left(V_m + b\right)}$, $a = \frac{0.42748 R^2 T_c^{\,2.5}}{p_c}$ and $b = \frac{0.08662 RT_c}{p_c}$, 1949) and Peng-Robinson equation of state ($p = \frac{RT}{V_m - b} - \frac{a}{V_m^{\,2} + 2bV_m - b^2}$, 1976).

(Ref: T.Y. Kwak, G.A. Mansoori. *Chem. Eng. Sci.* **1986**, *41*, 1303.).

The Peng-Robinson equation of state is applicable to the prediction of the properties of subcritical and supercritical fluids.

A6. JCPDS standard data of RuO_2, TiO_2

	Pattern	Lattice	2θ / °	d / Å	hkl	I/I_{max}
RuO_2	40-1290	tetragonal	28.010	3.18300	110	100
			35.051	2.55800	101	77
		$P4_2/mnm$ (136)	40.022	2.25100	200	12
			40.548	2.22300	111	6
		a = 4.49940	44.997	2.01300	210	1
		c = 3.10710	54.247	1.68960	211	39
			57.931	1.59060	220	9
		V_{cell} = 62.90	59.439	1.55380	002	6
			65.542	1.42310	310	5
			65.912	1.41600	221	3
			66.991	1.39580	112	8
			69.542	1.35070	301	7
			74.126	1.27810	202	4
			77.572	1.22970	212	1
			83.395	1.15800	321	5
			86.435	1.12490	400	1
			87.750	1.11140	222	4
			93.163	1.06050	330	2
			94.487	1.04910	312	4
			96.886	1.02940	411	3
			99.494	1.00930	103	3
			99.926	1.00610	420	2
			113.537	0.92090	213	4
			115.443	0.91110	402	1
	Pattern	Lattice	2θ / °	d / Å	hkl	I/I_{max}
TiO_2	21-1276	rutile	27.447	3.24700	110	100
			36.086	2.48700	101	50
		tetragonal	39.188	2.29700	200	8
			41.226	2.18800	111	25
		$P4_2/mnm$ (136)	44.052	2.05400	210	10
			54.323	1.68740	211	60
		a = 4.59330	56.642	1.62370	220	20
		c = 2.95920	62.742	1.47970	002	10
			64.040	1.45280	310	10
		V_{cell} = 62.43	65.480	1.42430	221	2
			69.010	1.35980	301	20
			69.790	1.34650	112	12
			72.410	1.30410	311	2
			74.411	1.27390	320	1
			76.510	1.24410	202	4
			79.822	1.20060	212	2
			82.335	1.17020	321	6
			84.260	1.14830	400	4
			87.464	1.11430	410	2
			89.557	1.09360	222	8
			90.708	1.08270	330	4
			95.275	1.04250	411	6
			96.017	1.03640	312	6

			97.176	1.02710	420	4
			98.514	1.01670	331	1
			105.099	0.97030	421	2
			106.019	0.96440	103	2
			109.406	0.94380	113	2
			116.227	0.90720	402	4
			117.527	0.90090	510	4
			120.059	0.88920	213	8
			122.788	0.87740	431	8
			123.660	0.87380	332	8
			131.847	0.84370	422	6
			136.549	0.82920	303	8
			140.052	0.81960	521	12
			143.116	0.81200	440	2
			155.869	0.78770	530	2
	Pattern	Lattice	2θ / ^{o}	d / Å	*hkl*	I/I_{max}
TiO_2	21-1272	anatase	25.281	3.52000	101	100
			36.947	2.43100	103	10
		body-centered	37.801	2.37800	004	20
		tegragonal	38.576	2.33200	112	10
			48.050	1.89200	200	35
		$I4_1/amd$ (141)	53.891	1.69990	105	20
			55.062	1.66650	211	20
		a = 3.78520	62.121	1.49300	213	4
		c = 9.51390	62.690	1.48080	204	14
			68.762	1.36410	116	6
		V_{cell} = 136.31	70.311	1.33780	220	6
			74.031	1.27950	107	2
			75.032	1.26490	215	10
			76.020	1.25090	301	4
			80.727	1.18940	008	2
			82.139	1.17250	303	2
			82.662	1.16640	224	6
			83.149	1.16080	312	4
			93.220	1.06000	217	2
			94.181	1.05170	305	4
			95.143	1.04360	321	4
			98.318	1.01820	109	2
			99.804	1.00700	208	2
			101.221	0.99670	323	2
			107.448	0.95550	316	4
			108.963	0.94640	400	4
			112.840	0.92460	307	2
			113.861	0.91920	325	2
			114.909	0.91380	411	2
			118.439	0.89660	219	4
			120.104	0.88900	228	2
			121.725	0.88190	413	2
			122.336	0.87930	404	2
			131.035	0.84640	420	2
			135.998	0.83080	327	2
			137.391	0.82680	415	4
			143.887	0.81020	309	2

			150.039	0.79740	424	4
			152.633	0.79280	0012	2
	Pattern	Lattice	2θ / ^{o}	d / Å	hkl	I/I_{max}
TiO_2	29-1360	brookite	25.340	3.51200	120	100
			25.689	3.46500	111	80
		orthorhombisch	30.808	2.90000	121	90
			32.791	2.72900	200	4
		Pcab (61)	36.252	2.47600	012	25
			37.297	2.40900	201	18
		a = 5.4558	37.934	2.37000	131	6
		b = 9.1819	38.371	2.34400	220	4
		c = 5.1429	38.576	2.33200	211	4
			39.205	2.29600	040	5
		V_{cell} = 257.63	39.967	2.25400	112	8
			40.153	2.24400	022	18
			42.340	2.13300	221	16
			46.072	1.96850	032	16
			48.012	1.89340	231	30
			49.173	1.85140	132	18
			49.694	1.83320	212	3
			52.012	1.75680	240	3
			54.205	1.69080	320	20
			55.234	1.66170	241	30
			55.711	1.64860	151	5
			57.176	1.60980	113	13
			57.685	1.59680	232	2
			59.991	1.54080	123	7
			62.065	1.49420	052	10
			63.065	1.47290	160	4
			63.416	1.46560	312	9
			63.643	1.46090	251	12
			64.104	1.45150	203	12
			64.603	1.44150	133	6
			65.003	1.43360	213	10
			65.876	1.41670	161	9
			68.768	1.36400	400	5
			70.432	1.33580	332	8
			71.490	1.31860	401	3
			71.931	1.31160	233	2
			73.648	1.28520	004	2
			76.949	1.23810	024	10
			79.025	1.21070	431	2
			79.283	1.20740	124	1
			83.643	1.15520	333	4
			84.288	1.14800	080	2
			84.724	1.14320	441	2
			86.743	1.12170	044	4
			95.590	1.03990	521	3
			95.993	1.03660	281	2
			97.609	1.02370	324	4
			102.559	0.98730	125	2
			103.201	0.98290	372	4

A7. Phase diagram of binary RuO_2-TiO_2 system

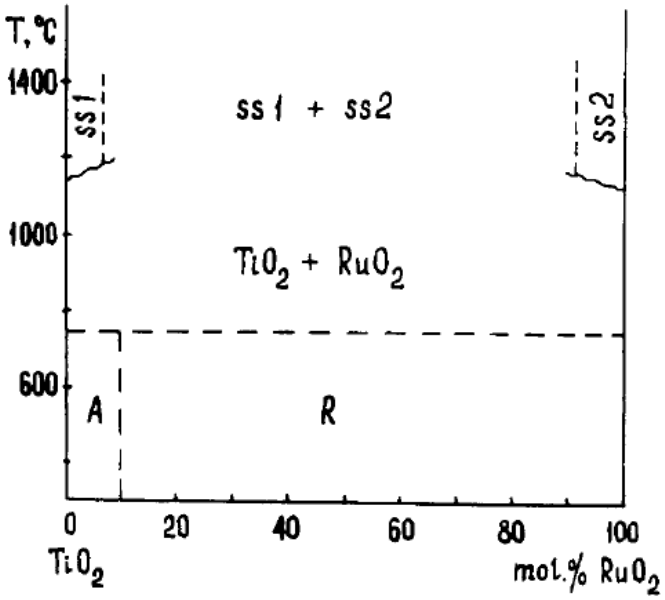

Figure A1. Phase diagram of RuO_2-TiO_2 system. Top: ss1: solid solution of RuO_2 in TiO_2; ss2: solid solution of TiO_2 in RuO_2. Below: phase composition of the TiO_2-RuO_2-Cl system, A: region with dominating anatase solid solution; R: region with dominating rutile solid solution. (Ref: Yu.E. Roginskaya, I.D. Belova, B.Sh. Galyamov, F.Kh. Chibirova, R.R. Shifrina. *Mater. Chem. Phys.* **1989**, *22*, 203.)

A8. Mathematic basics of noise analysis

A8.1 Standard deviation

For the statistical method, considering a discrete time-series, $x(t)$, measured by sampling the signal at constant intervals $\triangle t$, taking N points in the time record, the acquisition time of the record is $T = N \cdot \triangle t$. Accordingly, the sampling frequency is indicated as $1/\triangle t$ in Hz. The easier way to characterize a time series of random signal (x_0, x_1,…, x_{N-1}) is to calculate its arithmetic mean value (the mean intensity over all values of times), $\bar{x}$, and sample standard deviation, s, defined as:

$$\bar{x} = \frac{x_0 + x_1 + \ldots + x_{N-1}}{N} = \frac{1}{N}\sum_{i=0}^{N-1} x_i \tag{A.1}$$

$$s = \sqrt{\frac{1}{N-1}\sum_{i=0}^{N-1}\left(x_i - \bar{x}\right)^2} \tag{A.2}$$

The noise signal intensity and the fluctuation amplitude of current density (or potential) can be obtained from the above calculation, and the measurement results allow different electrocatalysts to be compared as a function of applied potential (or current density). For the electrode surface with larger anchored bubbles, larger amplitudes of signal fluctuation (i.e. larger standard deviation) are expected.

A8.2 Autocorrelation function

For the analysis of time domain signals, autocorrelation is often used to judge the presence of a periodic signal which has been buried in the noise. The autocorrelation function (ACF) of a periodic signal is also periodic, and more important with the same signal period and frequency. The autocorrelation is defined as the expected value of the product of a random variable or signal, $x(t)$, with a time-shifted version of itself, $x(t+\tau)$, where τ is an integer multiple of the time interval $\triangle t$. This illustrates how the signal resembles a delayed version of itself. The estimation of the mean normalized (biased) autocorrelation of a discrete time series (x_0, x_1,…, x_{N-1}) is obtained by using:

$$R_{xx}(k) = \frac{\frac{1}{N}\sum_{i=0}^{N-1-k}\left[\left(x_i - \bar{x}\right)\left(x_{i+k} - \bar{x}\right)\right]}{\frac{1}{N}\sum_{i=0}^{N-1}\left(x_i - \bar{x}\right)^2} \tag{A.3}$$

where x_i (i = 0, 1, …, N-1) is the amplitude of the time series, k = 0, 1, …, N-1 is the time lags. Various formulas can be found from the literature for the estimation of autocorrelation functions. The autocorrelation attenuates from $R_{xx}(0) = 1$ to the zero base line of the correlation function in the present formula, which makes it easy to analyze the data.

The correlation is calculated using a fast algorithm based on the correlation theorem (the Fourier transform of an autocorrelation function is equal to the product of the Fourier transform of the function and the complex conjugate of the Fourier transform of the function):

$$\mathcal{F}\{R_{xx}(\tau)\} = \mathrm{X}(f)\,\mathrm{X}^*(f) = |\mathrm{X}(f)|^2 \tag{A.4}$$

where $x(t)$ is the input signal, $\mathrm{X}(f)$ is the Fourier transform of $x(t)$, and $\mathrm{X}^*(f)$ the complex conjugate of $\mathrm{X}(f)$, $\mathcal{F}$ is the Fourier transform, $R_{xx}(\tau)$ is the autocorrelation of $x(t)$, then we have:

$$R_{xx}(\tau) = \mathcal{F}^{-1}\{\mathrm{X}(f)\,\mathrm{X}^*(f)\} \tag{A.5}$$

where $\mathcal{F}^{-1}$ is the inverse Fourier transform. The Fourier transform, $x(t) \xrightarrow{\mathcal{F}} \mathrm{X}(f)$, is defined as: $\mathrm{X}(f) = \int_{-\infty}^{\infty} x(t)\, \mathrm{e}^{-2\pi \mathrm{j} t f}\, \mathrm{d}t$.

A8.3 Fourier transform

Regarding the spectral methods, the signals are studied in frequency domain. In the time domain, signals are represented as amplitude versus time, whereas in the frequency domain, signals are expressed as amplitude versus frequency. It is more intuitional to see the period and amplitude of individual event contained in the overlapped transients. The transform of

time-domain data to frequency-domain data is executed by Fourier transformation. For a discrete sequence x_i of length N, its discrete Fourier transform (DFT) is given by:

$$f_{DFT}(k) = \sum_{i=0}^{N-1} x_i e^{-j2\pi \frac{ik}{N}} \tag{A.6}$$

where $k = 0,1,\ldots N\text{-}1$; j is the imaginary unit. The difference of frequency responses of two random signals can be distinguished from the Fourier transform, even if they possess a common mean value and similar overall randomness.

Power spectral density (PSD) of a random signal is the distribution of the signal power over frequency domain, which is computed based on the fast Fourier transform (FFT) algorithm. To determine the PSD, the signal has to be stationary, which means there should be no signal drift as a function of time. By definition, the power spectral density of a random time series $x(t)$ is the average of the Fourier transform magnitude squared over a time interval. If the signal is a wide-sense stationary process (the signal's mean and variance do not change over time or position, de-trending is necessary for a non-stationary signal), then the PSD is the Fourier transform of the autocorrelation function.

$$S_x(f) = \int_{-\infty}^{\infty} R_{xx}(\tau) e^{-j2\pi f\tau} d\tau \tag{A.7}$$

The power of a random signal, $x(t)$, over a given band of frequencies (in the range f_1~f_2) can be calculated as follows:

$$P_{12} = \int_{f_1}^{f_2} S_x(f) df \tag{A.8}$$

The slope of the PSD plot on a log-log scale has been proposed as a characterization of bubble evolution mechanisms, such as diffusion-controlled bubble growth, bubble coalescence and gas oscillatory behaviour caused by the synchronized gas production and gas release. Besides, the PSD plots contain the information of magnitude and characteristic frequency, and frequency distribution of the signal.

In the Fourier analysis, the linear time-invariant signals are correlated with sine waves by linear time-invariant operators. For the non-stationary or transient signals, the Fourier

analysis becomes invalid. In addition, the Fourier transform gives frequency components presented in the signals, but loses the time localized information.

A8.4 Wavelet transform

Wavelet analysis represents a more accurate and efficient method of time-frequency localization in the analysis of electrochemical noise signals and has been used to overcome the limitations of the Fourier transform. The information of both the amplitude of any periodic signals within the series and how the amplitude varies with time can be resolved. Wavelet transform of a function $x(t)$ is defined as:

$$W(b,a) = \frac{1}{\sqrt{a}} \int_{-\infty}^{\infty} x(t) \psi^* \left[\frac{t-b}{a} \right] dt \qquad \text{(A.9)}$$

where b, a are time index and wavelet scale, respectively. Function $\psi(t)$ is called as the mother wavelet, the asterisk ($*$) denotes the complex conjugate. The mother wavelet $\psi(t)$ is scaled by a factor of a, and shifted by a factor of b to obtain the wavelet basis: $\frac{1}{\sqrt{a}} \psi \left(\frac{t-b}{a} \right)$.

The plots of wavelet power spectrum give the high time and frequency resolutions of dominant events of a time (or spatial) series. The wavelet analysis results are very sensitive to the selection of mother wavelet function and the related parameters, and even contradictory results could be yielded among different analysis [169]. This fact should be kept in mind in the practical applications.

Wavelet analysis has been widely used in signal and image processing and has been proved to be universal in various applications and fields. In chemistry, wavelet transform has been utilized for signal processing in the analytical chemistry, including infrared spectroscopy, UV-Vis spectroscopy, mass spectrometry, chromatography, X-ray diffraction and various electroanalytical signals. (Ref: X.-G. Shao, A. K.-M. Leung, F.-T. Chau. *Acc. Chem. Res.* **2003**, *36*, 276.)

A9. MATLAB source code

The present MATLAB code is written for the purpose of demonstration. The details of the wavelet algorithms are explained somewhere else. (See: C. Torrence, G. P. Compo, A practical guide to wavelet analysis, *Bull. Am. Meteor. Soc*. 1998, *79*, 61.) The following MATLAB code is adapted from the Torrence's code for the Morlet wavelet transform. The Torrence's subprograms "chisquare_solve.m" and "chisquare_inv.m" were directly called herein by the main program "wavelet_fourier(x,fs,dj,smin,fname)". A 30-day trial version of MATLAB R2009b was kindly offered by The MathWorks, Inc. (Massachusetts, USA). The further data analysis using a licensed MATLAB version 7.0 was carried out in the group of our project partner Prof. Dr. W.F. Maier, Technical Chemistry, Saarland University.

```
%------------------------------------------------------------------------
% Fourier transform & Wavelet transform (Modified TC98 source code)
% Edited on 29. Jan 2010 by Ruiyong Chen
% Reference:
% C.Torrence, G.Compo,"http://paos.colorado.edu/research/wavelets/"
%
% Global wavelet spectrum excludes points within the coi herein
% Note that for TC98's code: global_ws=variance*(sum(power')/length(x));
%
% INPUTS:
% x = raw time series of potential fluctuations acquired by EC-Lab software
% fs = sampling frequency, 200 Hz
% dj = wavelet scale resolution
% smin = determine the smallest scale
% fname = 'figure name';
%
% OUTPUTS:
% a) Potential fluctuations under galvanostatic polarization mode
% b) Frequency spectrum
```

```
% c) FFT periodogram
% d) Local wavelet power spectrum
% e) Global wavelet spectrum
% whos
%
% Command Window INPUTS
% load 'x20sc_seg11_100mA_51878.dat'
% x=x20sc_seg11_100mA_51878;
% fname='20sc_seg11_100mA_51878';
% wavelet_fourier(x,200,0.25,50,fname)
%------------------------------------------------------------------------

function wavelet_fourier(x,fs,dj,smin,fname)
x_zeromean=x-mean(x);
variance=std(x)^2; % the square of the standard deviation, delta^2
x=(x-mean(x))/sqrt(variance); % normalized by std, with variance = 1
% fs=200; sampling frequency
time=(0:length(x)-1)*(1/fs); % construct time array
% FFT
% p=nextpow2(x) returns the smallest power of two that
% satisfies 2^p >= abs(x).
n1=2^nextpow2(length(x));
f1=(0:length(x)-1)*(fs/n1); % frequency range
y=fft(x,n1); % DFT, zero padding
mag=abs(y); % Amplitude of the DFT, Frequency spectrum
power1= y.*conj(y)/n1; % power of the DFT
% wavelet transform, Morlet, omega_0=6
% mother='Morlet';
k0=6;
dt=1/fs;
% dj=0.25;
% smin=50;
s0= smin *dt;
j1=fix(log2(length(x)/smin));
```

```
j1=j1/dj;
scale=s0*2.^((0:j1)*dj); % construct scale array, 1-by-(j1+1)
fourier_factor=(4*pi)/(k0 + sqrt(2 + k0^2)); % fourier_factor=1.033044
period=scale.*fourier_factor; % compute Fourier period
% cone of influence
coi = fourier_factor/sqrt(2)*dt*...
[1E-5,1:((length(x)+1)/2-1),fliplr((1:(length(x)/2-1))),1E-5];
% zero padding, construct Fourier angular frequency array, omega_k
z(1:length(x))=x-mean(x); % x is the normalized time series, see above
base2=fix(log(length(x))/log(2)+0.4999);
z=[z,zeros(1,2^(base2+1)- length(x))] ; % new time series 'z'
n=length(z); % Attention!!! n is not equal to n1
k=[1:fix((n/2))];
k=k.*((2.*pi)/(n*dt));
omegak=[0.,k,-k(fix((n-1)/2):-1:1)]; % 1-by-n
% wavelet transform
f=fft(z); % 1-by-n, complex
wave=zeros(j1+1,n); %construct empty wave array,(j1+1)-by-n matrix of zeros
wave=wave+1i*wave; % make it complex
nomegak=length(omegak);
for a1 = 1:j1+1
expnt = -(scale(a1).*omegak - k0).^2/2.*(omegak > 0.);
norm = sqrt(scale(a1)* omegak (2))*(pi^(-0.25))*sqrt(nomegak);
% sqrt(scale* omegak (2)) * sqrt(nomegak) = sqrt(scale*2*pi/dt)
daughter = norm*exp(expnt);
daughter = daughter.*(omegak > 0.);
wave(a1,:) = ifft(f.*daughter);
end
% wavelet transform coefficients,(j1+1)-by-length(x)
coefs=wave(:,1:length(x));
power=(abs(coefs)).^2;
transpose=power'; % length(x)-by-(j1+1)
% global wavelet power spectrum includes points within coi
```

```
% break terminates the execution of a for or while loop.
% In nested loops, break exits only from the loop in which it occurs.
% returns the index of the maximal period (id_period) outside the coi
for id_period=1:j1+1
if (period(id_period)>=max(coi)),id_period=id_period-1; break, end
end
% global wavelet power spectrum excludes points within coi
for b1=id_period:-1: 1
if mod(length(x),2) == 0 %length(x) is even
valid=fix((max(coi)-period(b1))/(max(coi)-period(1))...
* fix((length(x)+1)/2-1));
middle= ceil((length(x)+1)/2-1);
low=middle-valid;
high=middle+1+valid;
global_ws_excoi(b1)=sum(transpose(low:high,b1))/(2*(valid+1));
else % length(x) is odd
valid=fix((max(coi)-period(b1))/(max(coi)-period(1))...
* fix((length(x)+1)/2-1));
middle= ceil((length(x)+1)/2-1)+1;
low=middle-valid;
high=middle+valid;
global_ws_excoi(b1)=sum(transpose(low:high,b1))/(2*valid+1);
end
global_ws_excoi(b1)=variance* global_ws_excoi(b1);
end
%significance test
lag1=0.72;
gamma_factor=2.32;
freq=dt./period;
pk = (1-lag1^2)./(1-2*lag1*cos(freq*2*pi)+lag1^2);
fft_theor = variance*pk; % include time-series variance
dof=length(x) -scale;
dof = 2*sqrt(1 + (dof*dt/gamma_factor./ scale).^2 );
```

```
% Default confidence level: 0.95
% chisquare_inv(0.95,2)=5.9915
signif = fft_theor*chisquare_inv(0.95,2)/2; % signif(1-by(j1+1))
% ones(1,length(x))returns a 1-by-length(x) matrix of ones
sig95 = (signif')*(ones(1,length(x)));
sig95 = power./sig95; % when ratio > 1, power is significant
% significance level for global wavelet spectrum
for a1 = 1:j1+1
chisquare = chisquare_inv(0.95,dof(a1))/dof(a1);
global_signif(a1)= fft_theor(a1)*chisquare; % 1-by-(j1+1)
end
% OUTPUTS
% a) Normalized potential fluctuations
% b) Frequency spectrum
% c) FFT Periodogram
% d) Local wavelet power spectrum
% e) Global wavelet spectrum
% whos
subplot('position',[0.1 0.80 0.55 0.10])
plot(time,x,'k') % plot normalized time series
hold on
plot([1 max(time)],[0 0],'w--') % magenta color
hold off
xlabel('Time / s')
ylabel('Amplitude')
set(gca,'FontSize',8)
set(gca,'XLim',[min(time), max(time)])
text(-0.15,1.3,'(a)','sc','FontSize',8)% marking on the figure,
% text(x,y,'text','sc') adds the text in the quotes 'text' to
% location (x,y)on the current axes,
% 'sc' assuming lower left corner is (0,0) and upper right corner is (1,1)
set(gcf,'color','white')
subplot('position',[0.1 0.60 0.55 0.10])
```

```
plot(f1(1:n1/2),mag(1:n1/2)*2/n1,'k') % plot FFT amplitude vs. frequency
% The first half of the frequency range (0~Nyquist frequency, fs/2) is
% sufficient to identify the component frequencies in the data
xlabel('Frequency / Hz')
ylabel('Amplitude')
set(gca,'FontSize',8)
set(gca,'XLim',[f1(1), 2])% set maximal x-axes 2 Hz
text(-0.15,1.3,'(b)','sc','FontSize',8)
set(gcf,'color','white')
% plot FFT periodogram (plot of power versus frequency)
% loglog(x,y), logarithmic scale
subplot('position',[0.1 0.35 0.55 0.15])
loglog(f1(1:n1/2),power1(1:n1/2),'k')
xlabel('Frequency / Hz')
ylabel('FFT PSD')
set(gca,'FontSize',8)
set(gca,'YLim',[1E-10, 1E5],...
'YTick',[1E-10 1E-5 1E0 1E5])
text(-0.15,1.2,'(c)','sc','FontSize',8)
set(gcf,'color','white')
grid on
% Contour plot wavelet power spectrum
subplot('position',[0.1 0.1 0.55 0.15])
levels = [0.0625,0.125,0.25,0.5,1,2,4,8,16]; % 1-by-9
Yticks = 2.^(fix(log2(min(period))):fix(log2(max(period))));
contour(time,log2(period),log2(power),log2(levels));
xlabel('Time / s')
ylabel('Period / s')
set(gca,'YLim',log2([min(period),max(period)]), ...
'YDir','reverse', ...
'YTick',log2(Yticks(:)), ...
'YTickLabel',Yticks)
set(gca,'FontSize',8)
```

```
text(-0.15,1.2,'(d)','sc','FontSize',8)
set(gcf,'color','white')
hold on
% level at -99 (fake) and 1(5% significance level)
contour(time,log2(period),sig95,[-99,1],'k');
hold on
plot(time,log2(coi),'k') % cone-of-influence
hold off
% plot global wavelet spectrum excludes points within the coi
% plot([min(global_ws) max(global_ws)],[log2(max(coi))...
% log2(max(coi))],'r--')
subplot('position',[0.72 0.1 0.15 0.15])
plot(global_ws_excoi,log2(period(1:id_period)),'k')
xlabel('Power')
set(gca,'YLim',log2([min(period),max(period)]), ...
'YDir','reverse', ...
'YTick',log2(Yticks(:)), ...
'YTickLabel',Yticks)
set(gca,'XLim',[-0.02*max(global_ws_excoi), 1.2*max(global_ws_excoi)])
set(gca,'Ygrid','on')
set(gca,'FontSize',8)
text(-0.3,1.2,'(e)','sc','FontSize',8)
set(gcf,'color','white')
hold on
% plot significance level
% plot(global_signif(1:id_period),log2(period(1:id_period)),'r--')
plot(global_signif,log2(period),'r--')
hold off
% save figure as *.fig, *.tif
saveas(gcf,fname,'fig');
saveas(gcf,fname,'tif');
whos
% end of code
```

A10. Publications

A10.1 Journal article

1. **R. Chen**, V. Trieu, H. Natter, K. Stöwe, W.F. Maier, R. Hempelmann, A. Bulan, J. Kintrup, R. Weber.
   In-situ supported nanoscale $Ru_xTi_{1-x}O_2$ on anatase TiO_2 with improved electroactivity, *Chem. Mater*. 2010, *22*, 6215-6217.

A10.2 Patents

2. **R. Chen**, V. Trieu, H. Natter, R. Hempelmann, A. Bulan, J. Kintrup, R. Weber. Verfahren zur Herstellung von Anodenbeschichtungen für die Elektrolytische Chlorherstellung,
   Deutsches Patent, Anmeldetag: 28.10.2010.

3. **R. Chen**, V. Trieu, H. Natter, R. Hempelmann, A. Bulan, J. Kintrup, R. Weber. Anoden mit erhöhtem Anatas-Gehalt für die elektrolytische Chlorgewinnung,
   Deutsches Patent, Aktenzeichen 10 2010 030 293.7, Anmeldetag: 21.06.2010.

A10.3 Conference proceedings

4. V. Trieu, **R. Chen**, H. Natter, R. Hempelmann.
   Ru-based Mixed Oxide Electrodes Prepared by Electrochemical Deposition,
   Poster: Electrochemistry 2010: From Microscopic Understanding to Global Impact. Bochum, 13-15.09.2010.

5. **R. Chen**, V. Trieu, H. Natter, R. Hempelmann, K. Stöwe, W. F. Maier.
   Oxide Catalysts for Electrochemical Chlorine Evolution Prepared by Sol-gel Route,
   Talk: Minisymposium: From molecules to Materials, Saarbrücken, 10-11.09.2009.

A11. Acknowledgements

The present work was carried out at the Institute of Physical Chemistry at Saarland University, in the period from Sep. 2006 to Sep. 2010 under the supervision of Prof. Dr. Rolf Hempelmann. I gratefully acknowledge and thank Prof. Hempelmann for providing me the great opportunity and for showing his enthusiastic support for my Ph. D. research work. Thanks to Dr. Harald Natter for many fruitful discussions. Thanks to Mrs. Sylvia Kuhn for showing endless patience for the SEM, TEM measurements. Thanks to Josef Wilhelm and Dieter Münch for the help in technical problems.

Special thanks to my partner Mr. Vinh Trieu, who measured electrochemically all of my Sol-Gel coatings with great passions and *burdened* me with several GB of the very precious raw data. I am very grateful for his help to screen out the well-pleasing coatings.

I would also like to acknowledge Prof. Dr. Wilhelm F. Maier, Prof. Dr. Klaus Stöwe and their research group at the Institute of Technical Chemistry at Saarland University for the practical help in the sol-gel preparation. Thanks to Prof. Dr. Wilhelm F. Maier for kindly providing the MATLAB software program. Thanks to Prof. Dr. Klaus Stöwe for XRD Rietveld refinement analysis.

The Bayer MaterialScience AG (Project: ‘‘Identifizierung und Charakterisierung von Elektrokatalysatoren für die Chlorherstellung.’’) and BMBF (Joint project: ‘‘Effizienzsteigerung bei der Chlor-Herstellung.’’, FKZ: 033R018G) are acknowledged for financial support for the research projects. I would like to acknowledge our industrial project partners Mr. Andreas Bulan, Dr. Jürgen Kintrup, Dr. Rainer Weber for organizing the projects and their valuable advice.

Finally, I would like to gratefully thank my family for their love and support, and especially my wife Shuhua for all her love and patience.

Ruiyong Chen

Saarbrücken, 2010

A12. References

[1] J. Fauvarque. The chlorine industry. *Pure & Appl. Chem.* **1996**, *68*, 1713.

[2] T.F. O'Brien**,** T.V. Bommaraju, F. Hine. *Handbook of Chlor-Alkali Technology*, Vol. 1: Fundamentals, Springer, New York, **2005**, p.17.

[3] H. Deacon. Improvements in manufacture of chlorine. *U.S. Patent 165 802*, **1875**.

[4] http://worldchlorine.com/products/index.html.

[5] I. Moussallem, J. Jörissen, U. Kunz, S. Pinnow, T. Turek. Chlor-alkali electrolysis with oxygen depolarized cathodes: history, present status and future prospects. *J. Appl. Electrochem.* **2008**, *38*, 1177.

[6] S. Trasatti. Electrolysis: understanding the success of DSA$^{@}$. *Electrochim. Acta* **2000**, *45*, 2377.

[7] J. Kintrup, R. Weber, A. Bulan, M. Weis. Energy-efficient chlorine production with gas diffusion electrodes (ODC). *Electrochemistry-Crossing boundaries*, Oct. **2008**, Gießen, Germany.

[8] H.B. Beer. Improvements in or relating to electrodes for electrolysis. *British Patent 1 147 442*, **1965**.

[9] H.B. Beer. The invention and industrial development of metal anodes. *J. Electrochem. Soc.* **1980**, *127*, 303C.

[10] O. De Nora. Anwendung maßbeständiger aktivierter Titan-Anoden bei der Chloralkali-Elektrolyse. (Use of dimensionally stable, activated titanium anodes in alkali-metal chloride electrolysis.) *Chemie Ingenieur Technik* (*Chem. Eng. Technol.*) **1970**, *42*, 222.

[11] G.R.P. Malpass, R.S. Neves, A.J. Motheo. A comparative study of commercial and laboratory-made Ti/$Ru_{0.3}Ti_{0.7}O_2$ DSA$^{@}$ electrodes: ‘‘In-situ’’ and ‘‘ex-situ’’ surface characterization and organic oxidation activity. *Electrochim. Acta* **2006**, *52*, 936.

[12] H.A. Hansen, I.C. Man, F. Studt, F. Abild-Pedersen, T. Bligaard, J. Rossmeisl. Electrochemical chlorine evolution at rutile oxide (110) surfaces. *Phys. Chem. Chem. Phys.* **2010**, *12*, 283.

[13] S. Trasatti, W.E.O'Grady. in *Advances in Electrochemistry and Electrochemical Engineering*, Vol. 12, H. Gerischer and C.W. Tobias, Editors, Wiley, New York, **1981**, p. 117.

[14] S. Trasatti, G. Lodi. *Electrodes of conductive metallic oxides*. Elsevier, **1980**, pp. 301-358.

[15] S. Trasatti. Progress in the understanding of the mechanism of chlorine evolution at oxide electrodes. *Electrochim. Acta* **1987**, *32*, 369.

[16] T.F. O'Brien**,** T.V. Bommaraju, F. Hine. *Handbook of Chlor-Alkali Technology*, Vol. 1: Chemistry and Electrochemistry of the Chlor-Alkali Process, Springer, New York, **2005**, p. 111.

[17] H. Over. Ruthenium dioxide, a fascinating material for atomic scale surface chemistry. *Appl. Phys. A* **2002**, *75*, 37.

[18] V. De Nora, T.T. Nguyen. Non-carbon anodes with active coatings. *WO 2005/090641 A2*. **2005**.

[19] H.B. Beer. Composite catalytic material particularly for electrolysis electrodes and method of manufacture. *U.S. Patent 4 585 540*, **1986**.

[20] D.F. Difranco, K.L. Hardee. Pd-containing coating for low chlorine overpotential. *WO 2006/028443 A1*, **2006**.

[21] P.C.S. Hayfield. Development of the noble metal/oxide coated titanium electrode. Part II: The move from platinum/iridium to ruthenium oxide electrocatalysts. *Platinum Metals Rev.* **1998**, *42*, 46.

[22] F. Herlitz. Titanium in the electrochemical industry: use and protection. *Stainless Steel World* **2004**, www.stain-steel-world.net

[23] T. Loučka. The reason for the loss of activity of titanium anodes coated with a layer of RuO_2 and TiO_2. *J. Appl. Electrochem.* **1977**, *7*, 211.

[24] H.B. Beer. Electrode and coating therefore. *U.S. Patent 3 632 498*, **1972**.

[25] J. Aromaa, O. Forsén. Evaluation of the electrochemical activity of a Ti-RuO_2-TiO_2 permanent anode. *Electrochim. Acta* **2006**, *51*, 6104.

[26] S. Trasatti. Electrocatalysis in the anodic evolution of oxygen and chlorine. *Electrochim. Acta* **1984**, *29*, 1503.

[27] C. Angelinetta, S. Trasatti, Lj.D. Atanasoska, Z.S. Minevski, R.T. Atanasoski. Effect of preparation on the surface and electrocatalytic properties of RuO_2+IrO_2 mixed oxide electrodes. *Mater. Chem. Phys.* **1989**, *22*, 231.

[28] S.V. Evdokimov. Electrochemical and corrosion behavior of electrode materials based on compositions of ruthenium dioxide and based-metal oxides. *Russ. J. Electrochem.* **2002**, *38*, 583.

[29] M. Aparicio, L.C. Klein. Thin and thick RuO_2-TiO_2 coatings on titanium substrates by the sol-gel process. *J. Sol-Gel Sci. Technol.* **2004**, *29*, 81.

[30] V. Panić, A. Dekanski, S. Milonjić, R. Atanasoki, B. Nikolić. Influence of the aging time of RuO_2 and TiO_2 sols on the electrochemical properties and behavior for the chlorine evolution reaction of activated titanium anodes obtained by the sol-gel procedure. *Electrochim. Acta* **2000**, *46*, 415.

[31] L.A. De Faria, J.F.C. Boodts, S. Trasatti. Physico-chemical and electrochemical characterization of Ru-based ternary oxides containing Ti and Ce. *Electrochim. Acta* **1992**, *37*, 2511.

[32] K.J. O'Leary. *U.S. Patent 3 776 834*, **1973**.

[33] Yu.E. Roginskaya, O.V. Morozova. The role of hydrated oxides in formation and structure of DSA-type oxide electrocatalysts. *Electrochim. Acta* **1995**, *40*, 817.

[34] M.H.P. Santana, L.M. Da Silva, L.A. De Faria. Investigation of surface properties of Ru-based oxide electrodes containing Ti, Ce and Nb. *Electrochim. Acta* **2003**, *48*, 1885.

[35] M.H.P. Santana, L.A. De Faria. Oxygen and chlorine evolution on RuO_2+TiO_2+CeO_2+Nb_2O_5 mixed oxide electrodes. *Electrochim. Acta* **2006**, *51*, 3578.

[36] T. Zhang, D. Tang, Y. Shao, X. Ke, S. You. Synthesis and characterization of nanoscale $Ce_{(x)}Ru_{(1-x)}O_2$ coatings with electrochemical activity. *J. Am. Ceram. Soc.* **2007**, *90*, 989.

[37] T.A.F. Lassali, J.f.C. Boodts, S. Trasatti. Electrocatalytic activity of the ternary oxide $Ru_{0.3}Pt_xTi_{(0.7-x)}O_2$ for chlorine evolution. *Electrochim. Acta* **1994**, *39*, 1545.

[38] C.R. Davidson, J.M. Sedlak. Halogen evolution with improved anode catalyst. *WO/1981/003186*, **1981**.

[39] A. De Battisti, S. Ferro, M. Dal Colle. Electrocatalysis at conductive diamond modified by noble-metal oxides. *J. Phys. Chem. B* **2001**, *105*, 1679.

[40] S. Ferro, A. De Battisti. Electrocatalysis and chlorine evolution reaction at ruthenium dioxide deposited on conductive diamond. *J. Phys. Chem. B* **2002**, *106*, 2249.

[41] J.V. Ryan, A.D. Berry, M.L. Anderson, J.W. Long, R.M. Stroud, V.M. Cepak, V.M. Browning, D.R. Rolison, C.I. Merzbacher. Electronic connection to the interior of a mesoporous insulator with nanowires of crystalline RuO_2. *Nature* **2000**, *406*, 169.

[42] T. Arikawa, Y. Takasu, Y. Murakami, K. Asakura, Y. Iwasawa. Characterization of the structure of RuO_2-IrO_2/Ti electrodes by EXAFS. *J. Phys. Chem. B* **1998**, *102*, 3736.

[43] L.M. Doubova, S. Daolio, A. De Battisti. Examination of RuO_2 single-crystal surfaces: charge storage mechanism in H_2SO_4 aqueous solution. *J. Electroanal. Chem.* **2002**, *532*, 25.

[44] W.E. O'Grady, A.K. Goel, F.H. Pollak, H.L. Park, Y.S. Huang. Cyclic voltammetry on RuO_2 (100), (101), (001) and (110) ''as-grown'' single-crystal surfaces. *J. Electroanal. Chem.* **1983**, *151*, 295.

[45] E. Guerrini, V. Consonni, S. Trasatti. Surface and electrocatalytic properties of well-defined and vicinal RuO_2 single crystal faces. *J. Solid State Electrochem.* **2005**, *9*, 320.

[46] Z. Yi, C. Kangning, W. Wei, J. Wang, S. Lee. Effect of IrO_2 loading on RuO_2-IrO_2-TiO_2 anodes: A study of microstructure and working life for the chlorine evolution reaction. *Ceram. Int.* **2007**, *33*, 1087.

[47] V. Panić, A. Dekanski, S. Milonjić, V.B. Mišković-Stanković, B. Nikolić. Activity and stability of RuO_2-coated titanium anodes prepared via the alkoxide route. *J. Serb. Chem. Soc.* **2006**, *71*, 1173.

[48] A.J. Terezo, E.C. Pereira. Preparation and characterization of Ti/RuO_2 anodes obtained by sol-gel and conventional routes. *Mater. Lett.* **2002**, *53*, 339.

[49] S. Trasatti. Physical electrochemistry of ceramic oxides. *Electrochim. Acta* **1991**, *36*, 225.

[50] S.M. Hoseinieh, F. Ashrafizadeh, M.H. Maddahi. A comparative investigation of the corrosion bahavior of RuO_2-IrO_2-TiO_2 coated titanium anodes in chloride solutions. *J. Electrochem. Soc.* **2010**, *157*, E50.

[51] L.M. Da Silva, K.C. Fernandes, L.A. De Faria, J.F.C. Boodts. Electrochemical impedance spectroscopy study during accelerated life test of conductive oxides: Ti/(Ru+Ti+Ce)O_2-system. *Electrochim. Acta* **2004**, *49*, 4893.

[52] V. Panić, A. Dekanski, V. Jovanović, V.D. Jović, M.W. Barsoum. Ruthenium oxide based coatings formed on Ti_3SiC_2 support. *57th Annual Meeting of the International Society of Electrochemistry*, Book of Abstracts II, Edinburgh, UK, **2006**, p. S4-P-19.

[53] F. Gestermann, H.-D. Pinter, G. Speer, P. Fabian, R. Scannel. Electrode for electrolysis in acid media. *U.S. Patent 7 211 177 B2*, **2007**.

[54] C. Gabrielli, F. Huet, R. P. Nogueira. Electrochemical noise measurements of coalescence and gas-oscillator phenomena on gas-evolving electrodes. *J. Electrochem. Soc.* **2002**, *149*, E71.

[55] F. Lugli, F. Zerbetto. An introduction to bubble dynamics. *Phys. Chem. Chem. Phys.* **2007**, *9*, 2447.

[56] G. Liger-Belair, M. Vignes-Adler, C. Voisin, B. Robillard, P. Jeandet, *Langmuir*, **2002**, *18*, 1294-1301.

[57] R. Ettelaie, E. Dickinson, Z. Du, B.S. Murray. Disproportionation of clustered protein-stabilized bubbles at planar air-water interfaces. *J. Colloid Interface Sci.* **2003**, *263*, 47.

[58] D. Kiuchi, H. Matsushima, Y. Fukunaka, K. Kuribayashi. Ohmic resistance measurement of bubble froth layer in water electrolysis under microgravity. *J. Electrochem. Soc.* **2006**, *153*, E138.

[59] J. Dukovic, C.W. Tobias. Influence of attached bubbles on potential drop and current distribution at gas-evolving electrodes. *J. Electrochem. Soc.* **1987**, *134*, 331.

[60] L. Cassayre, T.A. Utigard, S. Bouvet. Visualizing gas evolution on graphite and oxygen-evolving anodes. *JOM* **2002**, *54*, 41.

[61] P. Boissonneau, P. Byrne. Experimental investigation of bubble-induced free convection in a small electrochemical cell. *J. Appl. Electrochem.* **2000**, *30*, 767.

[62] A. Legat, V. Doleček. Chaotic analysis of electrochemical noise measured on stainless steel. *J. Electrochem. Soc.* **1995**, *142*, 1851.

[63] B.M. Grafov, L.S. Kanevskii, M.G. Astafiev. Noise characterization of surface processes of the Li/organic electrolyte interface. *J. Appl. Electrochem.* **2005**, *35*, 1271.

[64] L. Kwiatkowski. Phosphate coatings porosity: Review of new approaches. *Surface Engineering* **2004**, *20*, 292.

[65] A. Aballe, M. Bethencourt, F. J. Botana, M. Marcos. Using wavelets transform in the analysis of electrochemical noise data. *Electrochim. Acta* **1999**, *44*, 4805.

[66] J. Livage, F. Beteille, C. Roux, M. Chatry, P. Davidson. Sol-gel synthesis of oxide materials. *Acta Mater.* **1998**, *46*, 743.

[67] B.L. Cushing, V.L. Kolesnichenko, C.J.O Connor. Recent advances in the liquid-phase synthesis of inorganic nanoparticles. *Chem. Rev.* **2004**, *104*, 3893.

[68] D.E. Babushkin, E.P. Talsi. Formation, solution structure and reactivity of alkylperoxo complexes of titanium. *J. Mol. Catal. A: Chem.* **2003**, *200*, 165.

[69] C.J. Brinker, G.W. Scherer. Sol-Gel science: The physics and chemistry of sol-gel processing. Academic Press, Inc, **1990**, p. 459.

[70] H. Kozuka, M. Kajimura, T. Hirano, K. Katayama. Crack-free, thick ceramic coating films via non-repetitive dip-coating using polyvinylpyrrolidones as stress-relaxing agent. *J. Sol-Gel Sci. Technol.* **2000**, *19*, 205.

[71] H. Kozuka, M. Kajimura. Single-step dip coating of crack-free $BaTiO_3$ films > 1μm thick: effect of poly(vinylpyrrolidone) on critical thickness. *J. Am. Ceram. Soc.* **2000**, *83*, 1056.

[72] J.G.M. van Berkum, A.C. Vermeulen, R. Delhez, T.H. De Keijser, E.J. Mittemeijer. Applicabilities of the Warren-Averbach analysis and an alternative analysis for separation of size and strain broadening. *J. Appl. Cryst.* **1994**, *27*, 345.

[73] H. Savaloni, M. Gholipour-Shahraki, M.A. Player. A comparison of different methods for X-ray diffraction line broadening analysis of Ti and Ag UHV deposited thin films: nanostructural dependence on substrate temperature and film thickness. *J. Phys. D: Appl. Phys.* **2006**, *39*, 2231.

[74] H.R. Rietveld. Line profiles of neutron powder-diffraction peaks for structure refinement. *Acta Cryst.* **1967**, *2*, 151.

[75] A.R. West. *Solid state chemistry and its applications*. John Wiley & Sons, **1984**, pp. 71-75.

[76] E. Rasten. *Electrocatalysis in water electrolysis with solid polymer electrolyte*. Ph.D Dissertation, Norwegian University of Science and Technology. **2001**, p. 13.

[77] T. Ohno, K. Sarukawa, K. Tokieda, M. Matsumura. Morphology of a TiO_2 photocatalyst (Degussa, P-25) consisting of Anatase and rutile crystalline phases. *J. Catal.* **2001**, *203*, 82.

[78] R. Loudon. The Raman effect in crystals. *Adv. Phys.* **1964**, *13*, 423.

[79] O.R. Camara, S. Trasatti. Surface electrochemical properties of Ti/(RuO_2+ZrO_2) electrodes. *Electrochim. Acta* **1996**, *41*, 419.

[80] S. Ardizzone, A. Carugati, G. Lodi, S. Trasatti. Surface structure of ruthenium dioxide electrodes and kinetics of chlorine evolution. *J. Electrochem. Soc.* **1982**, *129*, 1689.

[81] F. Hine, M. Yasuda, T. Yoshida. Studies on the oxide-coated metal anodes for chlor-alkali cells. *J. Electrochem. Soc.* **1977**, *124*, 500.

[82] L.D. Burke, O.J. Murphy, J.F. O'Neill, S. Venkatesan. The oxygen electrode. Part 8.-Oxygen evolution at ruthenium dioxide anodes. *J. Chem. Soc., Faraday Trans. 1* **1977**, *73*, 1659.

[83] L.D. Burke, O.J. Murphy. Surface area-voltammetric charge correlation for RuO_2/TiO_2-based anodes. *J. Electroanal. Chem.* **1980**, *112*, 39.

[84] R.G. Hutchinson, N.A. Fleck, A.C.F. Cocks. A sintering model for thermal barrier coatings. *Acta Mater.* **2006**, *54*, 1297.

[85] V. Panić, A. Dekanski, V.B. Mišković-Stanković, S. Milonjić, B. Nikolić. On the deactivation mechanism of RuO_2-TiO_2/Ti anodes prepared by the sol-gel procedure. *J. Electroanal. Chem.* **2005**, *579*, 67.

[86] S. Trasatti. Oxide/aqueous solution interfaces, interplay of surface chemistry and electrocatalysis. *Mater. Chem. Phys.* **1987**, *16*, 157.

[87] P. Simon, Y. Gogotsi. Materials for electrochemical capacitors. *Nat. Mater.* **2008**, *7*, 845.

[88] W. Sugimoto, T. Shibutani, Y. Murakami, Y. Tkasu. Charge storage capabilities of rutile-type RuO_2-VO_2 solid solution for electrochemical supercapacitors. *Electrochem. Solid-State Lett.* **2002**, *5*, A170.

[89] C.-C. Hu, K.-H. Chang, M.-C. Lin, Y.-T. Wu. Design and tailoring of the nanotubular arrayed architecture of hydrous RuO_2 for next generation supercapacitors. *Nano Lett.* **2006**, *6*, 2690.

[90] Y.-Y. Chen, T. Zhang, X. Wang, Y.-Q. Shao, D. Tang. Phase structure and microstructure of a nanoscale TiO_2-RuO_2-IrO_2-Ta_2O_5 anode coating on titanium. *J. Am. Ceram. Soc.* **2008**, *91*, 4154.

[91] A. Marshall, B. Børresen, G. Hagen, M. Tsypkin, R. Tunold. Preparation and characterization of nanocrystalline $Ir_xSn_{1-x}O_2$ electrocatalytic powders. *Mater. Chem. Phys.* **2005**, *94*, 226.

[92] S. Ardizzone, C.L. Bianchi, G. Cappelletti, M. Ionita, A. Minguzzi, S. Ronfinini, A. Vertova. Composite ternary SnO_2-IrO_2-Ta_2O_5 oxide electrocatalysts. *J. Electroanal. Chem.* **2006**, *589*, 160.

[93] K. Macounová, M. Makarova, J. Franc, J. Jirkovský, P. Krtil. Influence of oxygen on reactivity of $Ru_{1-x}Fe_xO_{2-y}$-doped materials. *Electrochem. Solid-State Lett.* **2008**, *11*, F27.

[94] C. Angelinetta, S. Trasatti, Lj.D. Atanososka, R.T. Atanasoski. Surface properties of RuO_2+IrO_2 mixed oxide electrodes. *J. Electroanal. Chem.* **1986**, *214*, 535.

[95] V.V. Panić, A. Dekanski, S.K. Milonjić, R.T. Atanasoski, B.Ž. Nikolić. RuO_2-TiO_2 coated titanium anodes obtained by the sol-gel procedure and their electrochemical behaviour in the chlorine evolution reaction. *Colloids Surf., A* **1999**, *157*, 269.

[96] Y. Takasu, W. Sugimoto, Y. Nishiki, S. Nakamatsu. Structural analyses of RuO_2-TiO_2/Ti and IrO_2-RuO_2-TiO_2/Ti anodes used in industrial chlor-alkali membrane processes. *J. Appl. Electrochem.* **2010**, DOI 10.1007/s10800-010-0137-3.

[97] A.A. Bolzan, C. Fong, B.J. Kennedy, C.J. Howard. Structural studies of rutile-type metal dioxides. *Acta Cryst.* **1997**, *B53*, 373.

[98] J. Gaudet, A.C. Tavares, S. Trasatti, D. Guay. Physicochemical characterization of mixed RuO_2-SnO_2 solid solutions. *Chem. Mater.* **2005**, *17*, 1570.

[99] A.I. Onuchukwu, S. Trasatti. Effect of substitution of SnO_2 for TiO_2 on the surface and electrocatalytic properties of RuO_2+TiO_2 electrodes. *J. Appl. Electrochem.* **1991**, *21*, 858.

[100] S. Yuan, Q. Sheng, J. Zhang, H. Yamashita, D. He. Synthesis of thermally stable mesoporous TiO_2 and investigation of its photocatalytic activity. *Micropor. Mesopor. Mat.* **2008**, *110*, 501.

[101] K. Macounová, M. Makarova, J. Jirkovskỳ, J. Franc, P. Krtil. Parallel oxygen and chlorine evolution on $Ru_{1-x}Ni_xO_{2-y}$ nanostructured electrodes. *Electrochem. Acta* **2008**, *53*, 6126.

[102] Y. Takasu, S. Mizutani, M. Kumagai, S. Sawaguchi, Y. Murakami. Ti-V-W-O/Ti oxide electrodes as candidates for electrochemical capacitors. *Electrochem. Solid-State Lett.* **1999**, *2*, 1.

[103] K. Takahashi, Y. Wang, K. Lee, G. Cao. Fabrication and Li^+-intercalation properties of V_2O_5-TiO_2 composite nanorod arrays. *Appl. Phy. A* **2006**, *82*, 27.

[104] J.R. Osman, J.A. Crayston, A. Pratt, D.T. Richens. RuO_2-TiO_2 mixed oxides prepared from the hydrolysis of the metal alkoxides. *Mater. Chem. Phys.* **2008**, *110*, 256.

[105] M. Krämer, T. Schmidt, K. Stöwe, W.F. Maier. Structural and catalytic aspects of sol-gel derived copper manganese oxides as low-temperature CO oxidation catalyst. *Appl. Catal., A* **2006**, *302*, 257.

[106] L. Hernán, J. Morales, L. Sánchez, J. Santos. Use of Li-M-Mn-O [M = Co, Cr, Ti] spinels prepared by a sol-gel method as cathodes in high-voltage lithium batteries. *Solid State Ionics* **1999**, *118*, 179.

[107] L.J.Q. Maia, V.R. Mastelaro, S. Pairis, A.C. Hernandes, A. Ibanez. A sol-gel route for the development of rare-earth aluminium borate nanopowders and transparent thin films. *J. Solid State Chem.* **2007**, *180*, 611.

[108] J.M. Miller, L.J. Lakshmi. Spectroscopic characterization of sol-gel-derived mixed oxides. *J. Phys. Chem. B* **1998**, *102*, 6465.

[109] F.R. Kogler, M. Jupa, M. Puchberger, U. Schubert. Control of the ratio of functional and non-functional ligands in clusters of the type $Zr_6O_4(OH)_4(carboxylate)_{12}$ for their use as building blocks for inorganic-organic hybrid polymers. *J. Mater. Chem.* **2004**, *14*, 3133.

[110] H. Over, Y.D. Kim, A.P. Seitsonen, S. Wendt, E. Lundgren, M. Schmid, P. Varga, A. Morgante, G. Ertl. Atomic-scale structure and catalytic reactivity of the RuO_2(110) surface. *Science* **2000**, *287*, 1474.

[111] E. Härk, K. Lust, A. Jänes, E. Lust. Electrochemical impedance study of hydrogen evolution on Bi(001) electrode in the $HClO_4$ aqueous solutions. *J. Solid State Electrochem.* **2009**, *13*, 745.

[112] L.K. Xu, J.D. Scantlebury. Microstructure and electrochemical properties of IrO_2-Ta_2O_5 coated titanium anodes. *J. Electrochem. Soc.* **2003**, *150*, B254.

[113] R. Lin, P.L. Taberna, J. Chmiola, D. Guay, Y. Gogotsi, P. Simon. Microelectrode study of pore size, ion size, and solvent effects on the charge/discharge behaviour of microporous carbons for electrical double-layer capacitors. *J. Electrochem. Soc.* **2009**, *156*, A7.

[114] P.M. Biesheuvel, M.Z. Bazant. Nonlinear dynamics of capacitive charging and desalination by porous electrodes. *Phys. Rev. E* **2010**, *81*, 031502.

[115] T. Ohkubo, T. Konishi, Y. Hattori, H. Kanoh, T. Fujikawa, K. Kaneko. Restricted hydration structures of Rb and Br ions confined in slit-shaped carbon nanospace. *J. Am. Chem. Soc.* **2002**, *124*, 11860.

[116] J. Huang, B.G. Sumpter, V. Meunier. Theoretical model for nanoporous carbon supercapacitors. *Angew. Chem. Int. Ed.* **2008**, *47*, 520.

[117] E. Barsoukov, J.R. Macdonald. *Impedance spectroscopy: Theory, experiment, and applications*. (second Edition) John Wiley & Sons, Inc., **2005**, p. 75.

[118] J. Bisquert, M. Grätzel, Q. Wang, F. Fabregat-Santiago. Three-channel transmission line impedance model for mesoscopic oxide electrodes functionalized with a conductive coating. *J. Phys. Chem. B* **2006**, *110*, 11284.

[119] F. Fabregat-Santiago, E.M. Barea, J. Bisquert, G.K. Mor, K. Shankar, C.A. Grimes. High carrier density and capacitance in TiO_2 nanotube arrays induced by electrochemical doping. *J. Am. Chem. Soc.* **2008**, *130*, 11312.

[120] J. Lim, J.D. Whitcomb, J.G. Boyd, J. Varghese. Effect of electrode pore geometry modelled using Nerst-Planck-Poisson-modified stern layer model. *Comput. Mech.* **2009**, *43*, 461.

[121] L. Bai, L. Gao, B.E. Conway. Problem of in situ real-area determination in evaluation of performance of rough or porous, gas-evolving electrocatalysts. Part 1.-Basis for distinction between capacitance of the double layer and the pseudocapacitance due to adsorbed H in the H_2 evolution reaction at Pt. *J. Chem. Soc. Faraday Trans.* **1993**, *89*, 235.

[122] J.C. Myland, K.B. Oldham. Which of three voltammetric methods, when applied to a reversible electrode reaction, can best cope with double-layer capacitance and severe uncompensated resistance? *Anal. Chem.* **2000**, *72*, 3210.

[123] V. Lazarov, D. Stoychev. Method for determination of the kinetic parameters in electrolytes containing surface-active substances, accounting for the influence of electrode potential on the changes of the free electrode surface. *Electroanalysis* **2004**, *16*, 211.

[124] D. Galizzioli, F. Tantardini, S. Trasatti. Ruthenium dioxide: a new electrode material. I. Behaviour in acid solutions of inert electrolytes. *J. Appl. Electrochem.* **1974**, *4*, 57.

[125] N. Munichandraiah, S. Sathyanayana. Insoluble anode of porous lead dioxide for electrosynthesis : preparation and characterization. *J. Appl. Electrochem.* **1987**, *17*, 22.

[126] M. van Soestbergen, P.M. Biesheuvel, M.Z. Bazant. Diffuse-charge effects on the transient response of electrochemical cells. *Phys. Rev. E* **2010**, *81*, 021503.

[127] R. Liu, J. Duay, T. Lane, S.B. Lee. Synthesis and characterization of RuO_2/poly(3,4-ethylenedioxythiophene) composite nanotubes for supercapacitors. *Phys. Chem. Chem. Phys.* **2010**, *12*, 4309.

[128] M.T. Colomer, M.J. Velasco, J.R. Jurado. Synthesis and thermal evolution of TiO_2-RuO_2 xerogels. *J. Sol-Gel Sci. Technol.* **2006**, *39*, 211.

[129] J. Málek, A. Watanabe, T. Mitsuhashi. Sol-gel preparation of rutile type solid solution in TiO_2-RuO_2 system. *J. Therm. Anal. Cal.* **2000**, *60*, 699.

[130] P.H. Duvigneaud, A. Coussement. Effect of chlorine on solid solution formation in ruthenium titanium dioxide coatings. *J. Solid State Chem.* **1984**, *52*, 22.

[131] F. Hine, M. Yasuda, T. Yoshida. Studies on the oxide-coated metal anodes for chlorine-alkali cells. *J. Electrochem. Soc.* **1977**, *124*, 500.

[132] J. Muscat, V. Swamy, N.M. Harrison. First-principles calculations of the phase stability of TiO_2. *Phys. Rev. B* **2002**, *65*, 224112.

[133] F. Dachille, P.Y. Simons, R. Roy. Pressure-temperature studies of anatase, brookite, rutile and TiO_2-II. *American Mineralogist* **1968**, *53*, 1929.

[134] J.F. Banfield, D.R. Veblen. Conversion of perovskite to anatase and TiO_2 (B): a TEM study and the use of fundamental building blocks for understanding relationships among the TiO_2 minerals. *American Mineralogist* **1992**, *77*, 545.

[135] A.R. West. *Solid state chemistry and its applications*. John Wiley & Sons, **1984**, p. 445.

[136] M. Rajamathi, R. Seshadri. Oxide and chalcogenide nanoparticles from hydrothermal/solvothermal reactions. *Curr. Opin. Solid State Mater.* **2002**, *6*, 337.

[137] J. Cho, J.-K. Jeon. Optimization study on the azeotropic distillation process for isopropyl alcohol dehydration. *Korean J. Chem. Eng.* **2006**, *23*, 1.

[138] M. Wu, G. Lin, D. Chen, G. Wang, D. He, S. Feng, R. Xu. Sol-hydrothermal synthesis and hydrothermally structural evolution of nanocrystal titanium dioxide. *Chem. Mater.* **2002**, *14*, 1974.

[139] G. Demazeau. Solvothermal reactions: an original route for the synthesis of novel materials. *J. Mater. Sci.* **2008**, *43*, 2104.

[140] G. Li, L. Li, J. Boerio-Goates, B.F. Woodfield. High purity anatase TiO_2 nanocrystals: Near room-temperature synthesis, grain growth kinetics, and surface hydration chemistry. *J. Am. Chem. Soc.* **2005**, *127*, 8659.

[141] L.M. Bronstein, X. Huang, J. Retrum, A. Schmucker, M. Pink, B.D. Stein, B. Dragnea. Influence of iron oleate complex structure on iron oxide nanoparticle formation. *Chem. Mater.* **2007**, *19*, 3624.

[142] http://www.electrochem.org/dl/ma/206/pdfs/1540.pdf

[143] I. Shaltout. Crystallization kinetics and structure of (TeO_2-TiO_2-Fe_2O_3) glasses. *J. Mater. Sci.* **2000**, *35*, 323.

[144] M.M. Oliveira, D.C. Schnitzler, A.J.G. Zarbin. (Ti,Sn)O_2 mixed oxides nanoparticles obtained by the sol-gel route. *Chem. Mater.* **2003**, *15*, 1903.

[145] V. Swamy. Size-dependent modifications of the first-order Raman spectra of nanostructured rutile TiO_2. *Phys. Rev. B* **2008**, *77*, 195414.

[146] M. Ocaña, V. Fornés, J.V. García Ramos, C.J. Serna. Factors affecting the infrared and Raman spectra of rutile powders. *J. Solid State Chem.* **1988**, *75*, 364.

[147] H. Liu, W. Yang, Y. Ma, Y. Cao, J. Yao, J. Zhang, T. Hu. Synthesis and characterization of titania prepared by using a photoassisted sol-gel method. *Langmuir* **2003**, 19, 3001.

[148] L. Vegard. Die Konstitution der Mischkristalle und die Raumfüllung der Atome. *Z. Phys.* **1921**, *5*, 17.

[149] H. Nakano, N. Hasuike, K. Kisoda, K. Nishio, T. Isshiki, H. Harima. Synthesis of TiO_2 nanocrystals controlled by means of the size of magnetic elements and the level of doping with them. *J. Phys.: Condens. Matter.* **2009**, *21*, 064214.

[150] A.V. Korotcov, Y.-S. Huang, K.-K. Tiong, D.-S. Tsai. Raman scattering characterization of well-aligned RuO_2 and IrO_2 nanocrystals. *Raman Spectrosc.* **2007**, *38*, 737.

[151] M.T. Colomer, M.J. Velasco. Rutile-type dense ceramics fabricated by pressureless sitering of $Ti_{1-x}Ru_xO_2$ powders prepared by sol-gel. *J. Eur. Ceram. Soc.* **2007**, *27*, 2369.

[152] B.L. Cushing, V.L. Kolesnichenko, C.J. O'Connor. Recent advances in the liquid-phase synthesis of inorganic nanoparticles. *Chem. Rev.* **2004**, *104*, 3893.

[153] A.S. Barnard, L. A. Curtiss. Prediction of TiO_2 nanoparticle phase and shape transitions controlled by surface chemistry. *Nano Lett.* **2005**, *5*, 1261.

[154] S.C. Pillai, P. Periyat, R. George, D.E. McCormack, M.K. Seery, H, Hayden, J. Colreavy, D. Corr, S.J. Hinder. Synthesis of high-temperature stable anatase TiO_2 photocatalyst. *J. Phys. Chem. C* **2007**, *111*, 1605.

[155] Yu.G. Chirkov, V.I. Rostokin. Gas-generating porous electrodes: Effect of the porous space structure on polarization curves. *Russ. J. Electrochem.* **2001**, *37*, 353.

[156] D. Kiuchi, H. Matsushima, Y. Fukunaka, K. Kuribayashi. Ohmic resistance measurements of bubble froth layer in water electrolysis under microgravity. J. *Electrochem. Soc*. **2006**, *153*, E138.

[157] C. Gabrielli, F. Huet, R.P Nogueira. Electrochemical noise measurements of coalescence and gas-oscillator phenomena on gas-evolving electrodes. *J. Electrochem. Soc.* **2002**, *149*, E71.

[158] L. Zhang, Y. Zhang, X. Zhang, Z. Li, G. Shen, M. Ye, C. Fan, H. Fang, J. Hu. Electrochemically controlled formation and growth of hydrogen nanobubbles. *Langmuir* **2006**, *22*, 8109.

[159] M. Boinet, D. Marlot, J.C. Lenain, S. Maximovitch, F. Dalard, R.P. Nogueira. First results from coupled acousto-ultrasonics and electrochemical noise technique applied to gas evolving electrodes. *Electrochem. Commun.* **2007**, *9*, 2174.

[160] C. Gabrielli, F. Huet, M. Keddam. Real-time measurement of electrolyte resistance fluctuations. *J. Electrochem. Soc.* **1991**, *138*, L82.

[161] D.R. Hodgson. Application of electrochemical noise and in situ microscopy to the study of bubble evolution on chlorine evolving anodes. *Electrochim. Acta* **1996**, *41*, 605.

[162] C. Gabrielli, F. Huet, M. Keddam, A. Sahar. Investigation of water electrolysis by spectral analysis. I. Influence of the current density. *J. Appl. Electrochem*. **1989**, *19*, 683.

[163] H. Vogt. Contribution to the interpretation of the anode effect. *Electrochim. Acta* **1997**, *42*, 2695.

[164] F. Huet, M. Musiani, R.P. Nogueira. Electrochemical noise analysis of O_2 evolution on PbO_2 and PbO_2-matrix composites containing Co or Ru oxides. *Electrochim. Acta* **2003**, *48*, 3981.

[165] F. Huet, M. Musiani, R.P. Nogueira. Oxygen evolution on electrodes of different roughness: An electrochemical noise study. *J. Solid State Electrochem*. **2004**, *8*, 786.

[166] A. Maksumov, R. Vidu, A. Palazoglu, P. Stroeve. Enhanced feature analysis using wavelets for scanning probe microscopy images of surfaces. *J. Colloid Interface Sci.* **2004**, *272*, 365.

[167] X.-G. Shao, A.K.-M. Leung, F.-T. Chau. Wavelet: A new trend in chemistry. *Acc. Chem. Res*. **2003**, *36*, 276.

[168] I. Simonovski, M. Boltežar. The norms and variances of the Gabor, Morlet and general harmonic wavelet functions. *J. Sound Vib.* **2003**, *264*, 545.

[169] C. Torrence, G.P. Compo. A practical guide to wavelet analysis. *Bull. Am. Meteorol. Soc.* **1998**, *79*, 61.

[170] B. Cazelles, M. Chavez, G.C. De Magny, J.-F. Guégan, S. Hales. Time-depedent spectral analysis of epidemiological time-series with wavelets. *J. R. Soc. Interface* **2007**, *4*, 625.

[171] R. Büssow. An algorithm for the continous Morlet wavelet transform. *Mech. Syst. Signal Pr.* **2007**, *21*, 2970.

[172] P. Lachowicz. Wavelet analysis: a new significance test for signals dominated by intrinsic red-noise variability. *arXiv:0906.4176v1* [astro-ph.HE].

[173] D.S. Bloomfield, R.T.J. McAteer, M. Mathioudakis, D.R. Williams, F.P. Keenan. Propagating waves and magnetohydrodynamic mode coupling in the quiet-sun network. *Astrophys. J.* **2004**, *604*, 936.

[174] J.M. Silva, R.P. Nogueira, L. De Miranda, F. Huet. Hydrogen absorption estimation on Pd electrodes from electrochemical noise measurements in single-compartment cells. *J. Electrochem. Soc.* **2001**, *148*, E241.

[175] D. Schönfuss, L. Müller. On the current-potential curve of a very fast hydrogen evolution process up to high current densities. *Electrochim. Acta* **1994**, *39*, 2097.

[176] H. Vogt, Ö. Aras, R.J. Balzer. The limits of the analogy between boiling and gas evolution at electrodes. *Int. J. Heat Mass Transfer* **2004**, *47*, 787.

[177] S.D. Lubetkin. The fundamentals of bubble evolution. *Chem. Soc. Rev.* **1995**, *24*, 243.